Etudes expérimentales et numériques de la pyrolyse et l'oxydation du charbon pulvérisé dans les flammes étirées de méthane/oxygène/azote

Meng Xia

NNT : 2017SACLC060

THÈSE DE DOCTORAT DE L'UNIVERSITÉ PARIS-SACLAY,

préparée à CentraleSupélec.

ÉCOLE DOCTORALE N°579

Sciences mécaniques et énergétiques, matériaux et géosciences.

Spécialité Combustion.

Présentée par

Meng XIA

Experimental and numerical studies of pulverized coal devolatilization and oxidation in strained methane/oxygen/nitrogen flames

Thèse soutenue à Gif-sur-Yvette, le 21 novembre 2017.

Composition du jury:

Pr. Luc VERVISCH	INSA de Rouen	Président du Jury, Rapporteur
Dr. Guillaume VANHOVE	Université Lille 1	Rapporteur
Pr. Laurent CATOIRE	ENSTA ParisTech	Examinateur
Dr. Stéphanie de PERSIS	Université d'Orléans	Examinatrice
Dr. Michele VASCELLARI	TU Freiberg	Invité
Pr. Nasser DARABIHA	CentraleSupélec	Directeur de thèse
Pr. Benoît FIORINA	CentraleSupélec	Co-encadrant
M. Philippe SCOUFLAIRE	CNRS	Co-encadrant

Remerciements

Je tiens tout d'abord à remercier l'ensemble des membres du jury. Mes grands remerciements sont destinés aux deux rapporteurs de ce travail, Luc Vervisch et Guillaume Vanhove, pour le temps qu'ils ont consacré à la lecture de ma thèse ainsi que pour les remarques qu'ils m'adressent. Je voudrais remercier particulièrement Luc Vervisch pour avoir accepté la présidence de mon jury. Je souhaite ensuite remercier Laurent Catoire et Stéphanie de Persis d'avoir accepté de juger cette thèse et de tous les conseils donnés pour améliorer le manuscrit. Je remercie enfin Michele Vascellari d'avoir accepté d'assister à la présentation de ce travail et pour les discussions intéressantes sur la modélisation.

Je voudrais exprimer ma sincère gratitude à mon directeur de thèse, Nasser Darabiha, pour m'avoir orienté vers le domaine de recherche sur la combustion du charbon, pour m'avoir accompagnée et soutenue tout au long de la thèse, et pour m'avoir apporté de conseils précieux pour ce travail.

Je remercie vivement Benoît Fiorina de son encadrement sur la partie numérique, et d'avoir consacré beaucoup de temps pour discuter et améliorer ce travail. Je tiens à remercier sincèrement Philippe Scouflaire, mon encadrant sur la partie expérimentale, pour son soutien très important lors de la réalisation des dispositifs expérimentaux.

Il me faut remercier l'ensemble des personnels administratifs et techniques du laboratoire, qui m'ont immensément aidé lors des problèmes rencontrés. Je remercie David Charalampous d'avoir consacré du temps à m'apprendre l'utilisation du spectromètre. Je remercie également Erika Jean-Bart et Yannick Le Teno pour les fabrications et les dépannages de la manip.

Je profite ici pour remercier particulièrement Christophe Laux et Juan Carlos Rolon pour leur disponibilité et leur expertise sur la spectrométrie de la flamme. J'adresse aussi mes remerciements à Diego et Hernando pour leur contribution à la manip.

Je tiens à remercier tous les membres du laboratoire EM2C pour l'ambiance amicale, pour les discussions enrichissantes et pour les nombreux moments très agréables que j'ai passés pendant mes quatre ans en France. Je remercie les

chercheurs et les thésards avec qui j'ai partagé le bureau, Wenjie, Bene, Antoine, Pedro, Robin, Milan, Mathieu, Pierre, David, Thomas, Claire... Je pense aussi aux docteurs et thésards dont l'amitié m'a beaucoup encouragée au long de la thèse, Renaud, Maria, Florence, Pedro, Paul, Kévin, Mélody, Davi, Cédric, Adrian, Théa, Abigail, Yi, Lorella, Léo, Livia...

Je tiens à remercier le China Scholarship Council (CSC) d'avoir financé mes études de doctorat en France.

Il me faut également remercier tous mes amis chinois pour leurs accompagnements pendant mes séjours en France. Entre autres, Huan, Fangyuan, Xing, Jing, Zeyin, Wangshu... Sans eux, la vie à Paris aurait sûrement eu moins de couleurs.

Enfin, je remercie celles et ceux qui me sont chers, ma famille et mes proches, et en particulier mes parents qui sont toujours à mes côtés pour me protéger et me soutenir tant moralement que matériellement pour que je puisse poursuivre ce parcours académique.

Abstract

Coal has been and will continue to be one of the most important resources in the long term due to its abundant worldwide reserves and competitively low prices, especially used in power generation. Hence, improving the energy efficiency and effectively reducing pollution from coal combustion, especially from those with low rank coal, is significant to satisfy the increasing demand in energy production and to control pollutant emissions. Pulverized coal combustion (PCC) has been studied for the past century, but application of fundamental combustion research for industries is still limited due to the relations between different spatial and time scales and to the complexity of the combustion system. Also, the modeling of PCC with CFD tools requires a detailed approach to address issues related to two-phase flow, coal conversion modeling, heat transfer and pollutant emissions. Thus, more investigations into these aspects are needed. Given the large number of processes and factors that occur in PCC, experimental and numerical studies of small-scale PCC are required to introduce a reliable and efficient methodology for realistic PCC modeling.

In the present work, a laboratory-scale laminar strained configuration is used to investigate the characteristics of pulverized coal devolatilization and oxidation in a mixture of $CH_4/O_2/N_2$ reactive flow both in conventional air conditions and in oxygen-enriched combustion conditions. In order to stabilize the flame and to introduce a reference for comparison and validation of modeling, CH_4 is used to assist the particle combustion process. The advantages of the chosen configuration are that it is well suitable for the development of numerical models, especially 1-D simulations, and optical measurement techniques.

Non-intrusive optical diagnostics such as Flame Emission Spectroscopy (FES) and measurement of spontaneous emission (ASE) are employed for qualitative determination of excited-state radicals in the reaction region, which gives a good characterization of flame structure. Flame chemiluminescence has been widely employed as simple and nonintrusive optical diagnostic for combustion systems. The ability of interpreting chemiluminescence intensity to monitor equivalence ratio, heat release rate, pollutant emission and flame front location has been proved by previous studies. The spatial concentration evolution of three excited radicals, OH^*, CH^* and C_2^*, are analyzed in the present work.

Results show that the comparison between ASE and FES signals highlights the advantages and disadvantages of both methods. The spontaneous emission imaging using narrowband filters is spatially resolved and relatively les time-consuming than FES method. However, spectrally resolved FES permits blackbody emission correction, which has significant effect especially for the presence of coal particles.

Whilst devolatilization and gasification sub-models are involved in LES/RANS simulations of pulverized coal turbulent flames, their impacts on the flame structure and species concentrations still remain unclear. Therefore the analysis of PC sub-models is also an important issue towards better understanding and prediction of PCC. In the present study, 1-D modeling of this strained flow configuration is proposed for its capability of producing accurate descriptions of the flame structure with less computational cost and without loss of accuracy. The focus here is on the development and validation of modeling methods applied to our experimental configuration. Simulations using detailed gas-phase kinetics including OH^*, CH^*, and C_2^* sub-mechanisms and coal combustion sub-models are performed using the 1D-REGATH code developed at EM2C laboratory and compared with experimental data. Comparison with experiments showed that the current numerical configuration was suitable for the prediction of OH^*, CH^* and C_2^* emission. The ability of chemical kinetics models in prediction of coal flame chemiluminescence under different flame conditions is discussed. Special emphasis is also given to the effect of oxygen-enriched combustion (OEC). Finally, the predicted results from the modeling approach differed significantly with changes to the coal sub-models and kinetic parameters. Especially, the devolatilization model and coal pyrolysis products seem to play more important roles.

Résumé

Le charbon est l'une des ressources les plus importantes à long terme en raison de ses réserves mondiales et de son prix compétitifs, notamment utilisé dans la production d'électricité. Par conséquent, l'amélioration de l'efficacité et la réduction de la pollution provenant de la combustion du charbon, en particulier de ceux à faible teneur en carbone, sont significatives pour satisfaire la demande croissante d'énergie et pour contrôler les émissions de polluants. La combustion du charbon pulvérisé (PCC) a été étudiée au cours du dernier siècle, mais l'application de la recherche fondamentale aux industries est encore limitée en raison des différentes échelles spatiales et temporelles et de la complexité du système de combustion. En outre, la modélisation de PCC avec des outils CFD nécessite une approche détaillée pour aborder les problèmes liés au écoulement diphasique, à la modélisation de la pyrolyse du charbon, au transfert thermique et aux émissions de polluantes. Compte tenu du grand nombre de processus qui se produisent dans PCC, des études expérimentales et numériques de PCC à petite échelle sont nécessaires pour introduire une méthodologie fiable et efficace pour la modélisation réaliste de PCC.

Dans ce travail, une configuration laminaire stratifiée a été utilisé à étudier les caractéristiques de la pyrolyse et de l'oxydation du charbon pulvérisé dans un mélange de écoulements réactifs $CH_4/O_2/N_2$ à la fois dans les conditions atmosphériques conventionnelles et dans des conditions de combustion enrichies en oxygène. Afin de stabiliser la flamme et d'introduire une référence pour la comparaison et la validation de la modélisation, CH_4 est utilisé pour assister le processus de combustion des particules de charbon. Les avantages de la configuration sont qu'il est bien adapté au développement de modèles numériques, en particulier des simulations monodimensionnelles, et des diagnostics optiques.

Les diagnostics optiques non-intrusifs tels que la spectroscopie d'émission de flamme (FES) et la mesure des émissions spontanées (ASE) sont utilisés pour la détermination qualitative des radicaux d'état excité dans la région de réaction, ce qui donne une bonne caractérisation de la structure de la flamme. La chimiluminescence de la flamme a été utilisée en tant que diagnostic optique simple et non-intrusif pour les systèmes de combustion. La capacité d'interpréter l'intensité de la chimiluminescence pour surveiller la richesse, le taux de dé-

gagement de chaleur, l'émission de polluants et la position du front de flamme a été étudiée dans la littérature. L'évolution de la concentration spatiale de trois radicaux excités, OH^*, CH^* and C_2^* sont analysé dans ce travail. Les résultats montrent que la comparaison entre les signaux ASE et FES souligne les avantages et les inconvénients des deux méthodes. Les mesures d'émission spontanée utilisant des filtres optiques sont résolues dans l'espace et relativement longue durée que la méthode FES. Cependant, le FES spectrale permet la correction des émissions du corps noir, ce qui a un effet significatif surtout pour la présence de particules de charbon.

Alors que les sous-modèles de pyrolyse et d'oxydation sont impliqués dans les simulations LES / RANS de flammes PCC turbulentes, leurs impacts sur la structure de la flamme et les concentrations d'espèces restent peu clairs. Par conséquent, l'analyse des sous-modèles de charbon est également une question importante pour une meilleure compréhension et prédiction de PCC. Dans l' étude présentée ici, la modélisation monodimensionnelle de cette configuration est proposée pour une description précise de la structure de la flamme avec moins de coût de calcul sans perte de précision. L'accent est mis sur le développement et la validation des méthodes de modélisation appliquées à la configuration expérimentale. Des simulations utilisant des cinétiques détaillées en phase gazeuse y compris les sous-mécanismes de combustion OH^*, CH^* and C_2^* et les sous-modèles de combustion du charbon sont effectués en utilisant le code 1D-REGATH développé au laboratoire EM2C et comparé aux données expérimentales. La comparaison avec les expériences a montré que la configuration numérique actuelle était appropriée pour la prédiction des émissions de OH^*, CH^* and C_2^*. La capacité des modèles de cinétique chimique à prédire la chimiluminescence de flamme de charbon dans différentes conditions de flamme est démontrée. Un accent particulier est également accordé à l'effet des atmosphères enrichies en oxygène. Enfin, les résultats de simulation numérique diffèrent considérablement avec les modifications apportées aux sous-modèles de charbon et aux paramètres cinétiques. Le modèle de pyrolyse et les produits de pyrolyse du char semblent jouer des rôles plus importants.

Contents

List of Tables

List of Figures

Introduction

Coal: an outlook of world energy supply and usage

Coal is a readily combustible solid containing various organic and inorganic compounds. It is formed from vegetation consolidation and alteration by the effects of pressure and heat over millions of years. Carbon (C) is the main component of coal. It also contains varying amounts of other components, like hydrogen (H), oxygen (O), nitrogen (N), sulfur (S) and other trace elements. Main parameters to classify coal ranks are calorific value, volatile matter, fixed carbon, ash, and moisture. Different classifications of coal are used around the world, depending on the range of ages, composition and properties. Four main ranks are lignite, sub-bituminous coal, bituminous coal, and anthracite. Figure 1 explains briefly these ranks and their uses. In the process of coalification, peat is altered to lignite, lignite to sub-bituminous coal, sub-bituminous coal to bituminous coal, and bituminous coal is altered to anthracite. Lignite is the lowest rank that has the lowest heating value and lowest carbon content.

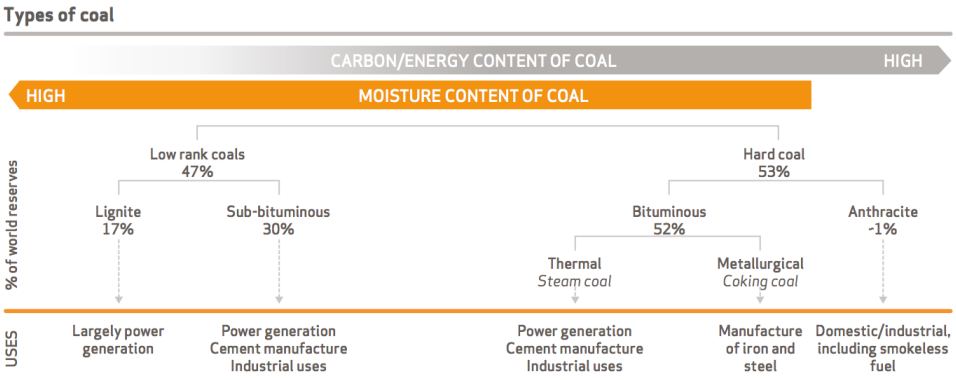

Figure 1: *Different types of coal and their uses, from World Coal Association (2017)*

Economic value of coal

The use of coal dates back thousands of years, and increases drastically during the Industrial Revolution and never stopped growing globally. And it is believed to remain significant in the future. Compared to other energy sources, its abundance, affordable prices, easy transportation and minor geopolitical tensions contributes to its popularity. Coal is the world's number one fuel for generating electricity, and the second source of primary energy (about 30%, declining to 27% by 2021, according to International Energy Agency (2016)). As reported by U.S. Energy Information Administration (2016), 41% of worldwide electricity is produced from coal and coal-fired power generation keeps to increase by 0.8%/year from 2012 to 2040 (Fig.2). In addition, coal is also an important raw material and source of primary energy for the manufacturing of materials. For exemple, coal is used in 70% of steel and 50% of aluminum production. To supply the large amount of energy required in cement manufacture, 200 kg of coal is needed to produce 1 tonne of cement, while 250-350 kg of cement is needed to produce $1m^3$ of concrete.

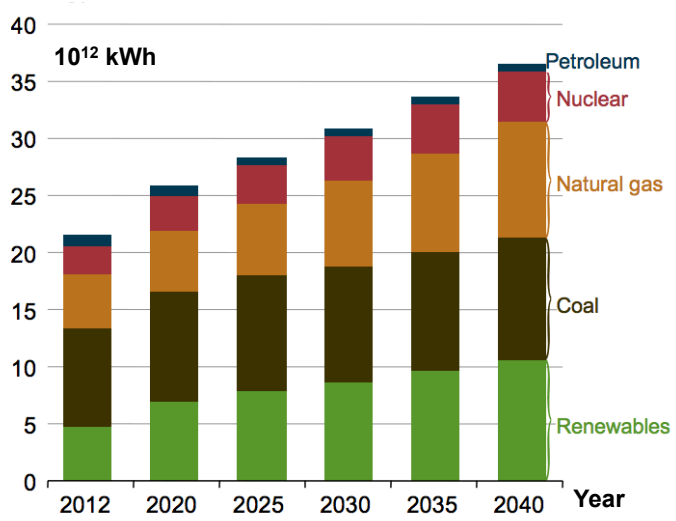

Figure 2: *2012-2040 World net electricity generation by energy source, unit: trillion kWh*

There are 6.9 billion tonnes of hard coal that are currently produced worldwide World Coal Association (2017). The top five hard coal producers are China, the USA, India, Australia and Indonesia. Most of global coal production is used in the country where it was produced. According to International Energy Agency (2016), the demand for coal is moving to Asia (Fig.3), where developing countries with growing populations, such as China and India, are seeking affordable and secure energy sources to power their economies.

Yet here lies the contradiction of coal - in the next few decades, while we rely on coal to provide essential energy, the problems of large amounts of pollutant emissions caused by coal uses must also be solved. Therefore, greater efforts are needed by industry and researchers to embrace less polluting and more efficient technologies to ensure cleaner coal energy.

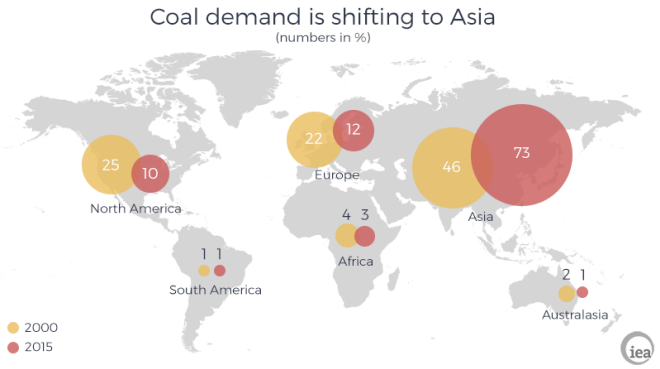

Figure 3: *Geographic map of global coal market share in percentage (%) of year 2000 and 2015*

Environmental issues

Global consumption of energy raises environmental concerns. For coal, the release of pollutants has always been an important challenge. The coal-related pollutants include sulfur and nitrogen oxides (SO_x and NO_x), particulate matter (PM) and trace elements, such as mercury. Although technologies have been developed to minimize these emissions, for exemple the sulfur removal from coal to prevent acid rain, additional environmental concerns have emerged in the recent years. Among them are the health impacts of the smog caused by microscopic particles pollution (PM2.5), and the global climate change from greenhouse gases. One of the important sources of greenhouse gases is carbon dioxide emissions (CO_2). The release of CO_2 into the atmosphere from human activities has been linked to global warming, and the combustion of fossil fuels is a major source.

While the use of petroleum in the transportation sector is the major source of energy-related CO_2 emissions in most developed countries, coal is also a significant source, especially in developing countries relying on coal to meet their energy needs. Coal is responsible for 45% of all energy-related carbon emissions according to U.S. Energy Information Administration (2016) (Fig.4). On the other hand, power plants using pulverized coal combustion (PCC) are the most carbon-intensive source of power generation. As CO_2 emissions need to be reduced dramatically and urgently, solving the issue of PCC related emissions has become a consensus of the international research community. As a result,

the industry has been researching and developing technological options to meet this new environmental challenge.

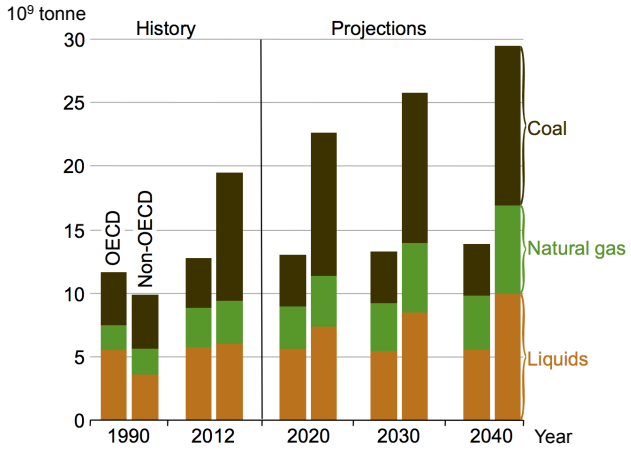

Figure 4: *1990-2040 Energy-related carbon dioxide emissions by fuel type of Organization for Economic Co-operation and Development (OECD) and non-OECD countries, unit: billion tonnes*

Clean coal technologies (CCT) are a range of technological options which improve the environmental performances of coal. These technologies reduce emissions and waste, and increase the efficiency from burning coal. Different technologies suit different types of coal and tackle different environmental problems. The choice of technology also depends on a country's economic development level. More expensive, highly advanced technologies may not be suitable in developing countries. While cheaper readily available options can have a larger and more affordable environmental benefit. A broad spectrum of research is targeting on efficiency improvement and pressing environmental challenges of coal conversion to electricity or other forms of energy.

Coal in power generation

A major part of coal is used mostly in power generation. Other ways of coal conversion includes coal gasification and liquefaction, which offer more versatile and clean ways to convert coal into electricity, hydrogen, and other valuable energy products.

In the most common type of coal plants, PCC is the technology used to produce electricity. Pulverized coal (PC) is blown into the furnace where it burns (Fig.5). Water flows through tubes that run through the furnace. The water is heated to boiling while under pressure. This pressurized steam blasts through a turbine, which turns a generator to produce electricity. After the steam has

passed through the turbine, it is condensed into water and cooled, and sent back into the furnace.

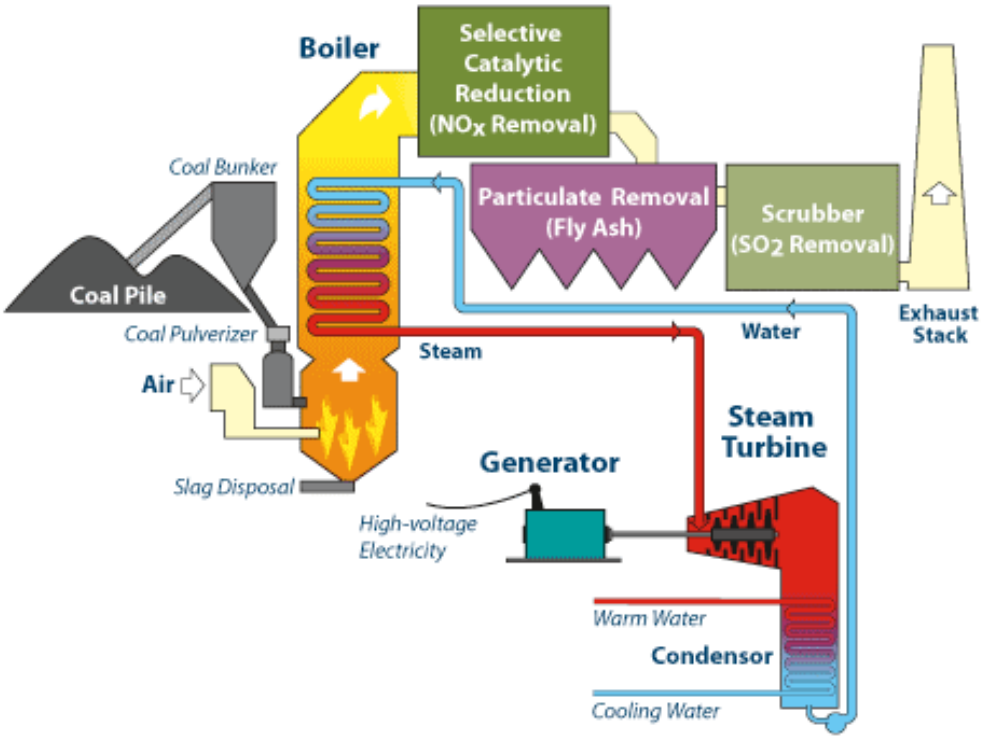

Figure 5: *Diagram of pulverized coal conversion to electricity from Partha Das Sharma (2008)*

Another type of coal-fired power plant uses "fluidized bed combustion (FBC)" instead of a standard furnace. A fluidized bed is made up of small particles of ash, limestone and other non-flammable materials, which are partially suspended in an upward flow of hot air. Pulverized coal and limestone are blown into the bed at high temperature. They burn in the bed, and the limestone binds with sulfur released from the coal. The heat then boils water in pipes (Fig.6). FBC systems fit into essentially two major groups, atmospheric systems (FBC) and pressurized systems (PFBC), and two minor subgroups, bubbling (BFB) and circulating fluidized bed (CFB). The advantage of FBC is that sulfur emissions are lower than in standard coal plants. The down side is that the plants are more complex and require more maintenance.

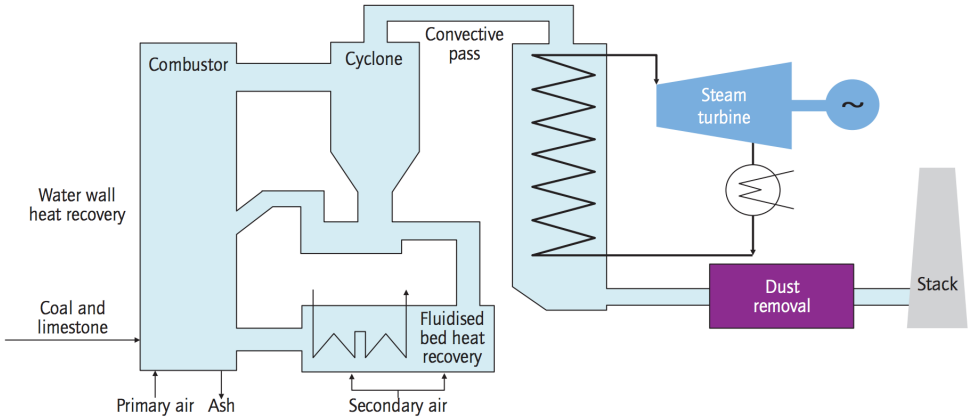

Figure 6: *Diagram of circulating fluidized bed combustion from International Energy Agency (2012)*

An alternative approach is to produce gaseous fuels from coal – this is called the integrated gasification combined cycle (IGCC). In IGCC, coal is not combusted directly but reacted with oxygen and steam to produce syngas composed mainly of hydrogen and carbon monoxide (Fig.7). This syngas is cleaned of impurities and then burns in a gas turbine to generate electricity and to produce steam for a steam power cycle. IGCC systems operate at higher efficiencies. They also remove 95-99% of NO_x and SO_x emissions. But the major drawback is the high capital cost compared to conventional forms of coal power plants.

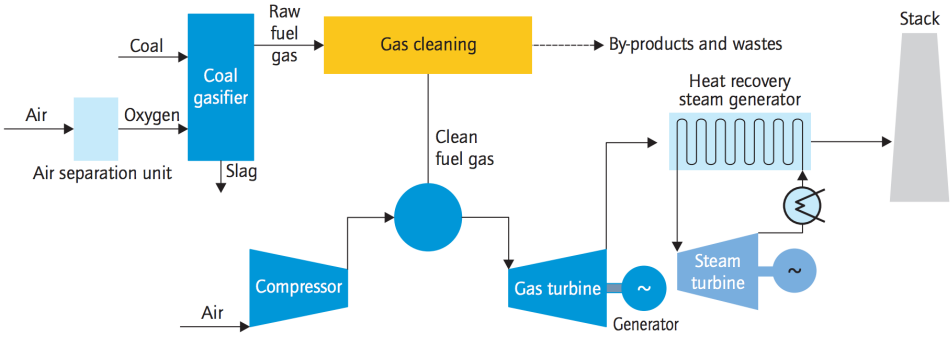

Figure 7: *Diagram of integrated gasification combined cycle from International Energy Agency (2012)*

Pulverized coal combustion technology

PCC is currently the most widely adopted system for coal-fired power generation. It accounts for over 90% of coal-fired capacity worldwide (Godridge 2010).

Improvements continue to be made in conventional PCC power station design and new combustion techniques are being developed. These developments allow improvement of the thermal efficiency.

PC power plants

In a PC furnace, finely powdered coal (with a size range typically 70% $\leq$ 75 μm) is burnt in a large combustion chamber (ClimateTechWiki 2010). The coal particles and air mixture is produced by conveying milled coal using preheated primary combustion air. The burner design may vary with different placements and secondary air admission. The aim of PCC system is to achieve maximum char burnout with the minimum production of NO_x. The combustion process is usually complete within a few seconds and the flame temperature is up to 1500 °C.

Three categories of PCC power generation with varying degrees of efficiency are commonly used: subcritical, supercritical, and ultra-supercritical pulverized coal plants (Nalbandian 2009). Operating temperatures and pressures (steam parameters) are the primary parameters to distinguish different types of PC boilers (Zhang 2013). Subcritical plants operate below the critical point of water (647.096 K and 22.064 MPa). Supercritical and ultra-supercritical plants operate above the critical point. As the pressures and temperatures increase, so does the operating efficiency. Subcritical plants are at about 37%, supercriticals at about 40% and ultra-supercriticals in the 42-45% range (ClimateTechWiki 2010).

Toward zero emission

As mentioned in the previous section, producing energy from coal can result in the release of varying degrees of pollutants that are harmful to human health and the environment. A brief summary of the formation and current technical solutions of SO_x, NO_x and Particulate Matter (PM) is introduced as follows.

Formation of SO_x:

SO_x emission levels can be calculated from coal sulphur content. Ash chemistry and ash content have important influence on the formation of SO_x because the asorption of SO_2 takes place in the ash. More precisely, the level of absorption increases with increasing levels of CaO, MgO, etc. and increasing ash content. SO_x emissions can be reduced by injection of a sorbent directly into the furnace chamber (Demirbas and Balat 2004) and/or by flue gas desulfurization (FGD) systems attached to the back end of the boiler (Cordoba 2015).

Formation of NO_x:

- **Thermal NO_x**
  It is formed by the attack of O atom on N_2 in the gas phase. About 20% of total NO_x emission from PC burners is thermal NO_x. It is mainly affected by flame temeprature and O_2 concentration, the former one being the most important.
- **Fuel NO_x**
  It comes from pyrolysis and oxidation of N compounds in coals. It takes up about 80% of total NO_x emission from PCC. However, the relation between N content in coal vs. fuel NO_x emission is not linear: Coals with higher N do not necessarily produce more NO_x. The O_2 concentration plays an important role in fuel N conversion into NO_x. The N content in char is converted to NO_x in a different way compared to N content in volatiles.
- **Prompt NO_x**
  The path is about the capture of N_2 by hydrocarbon radicals. It only contributes a small part to the total NO_x emission in PCC.

Formation of PM:

PM includes the tiny particles of fly ash and dust that come from coal-fired power plants. It has become the principal urban pollutant in many major cities in China and all over the world (Lu and Ren 2014). Technology has been developed to control the emissions of PM (Shanthakumar et al. 2008), including: Electrostatic precipitator (ESP) which uses an electrical field to create a charge on particles in the flue gas in order to attract them to collecting plates; and fabric filters, which collect particulates from the flue gas as it passes through the tightly woven fabric of the filter.

Reducing CO2 Emissions:

An important step in reducing CO_2 emissions from coal combustion has been improvements in the thermal efficiencies of coal-fired power stations. Thermal efficiency is a measure of the overall fuel conversion efficiency for the electricity generation process. The higher the efficiency levels, the greater the energy being produced from the fuel. Therefore, the current PC power plants can be categorized into different levels of CO_2 intensity factor based on their thermal efficiency (Fig.8).

An important factor in the future use of coal will be how to reduce CO2 emissions to the maximum. Much has been done to achieve this. But in order to achieve zero emission of CO_2 in the future, one of the most promising options

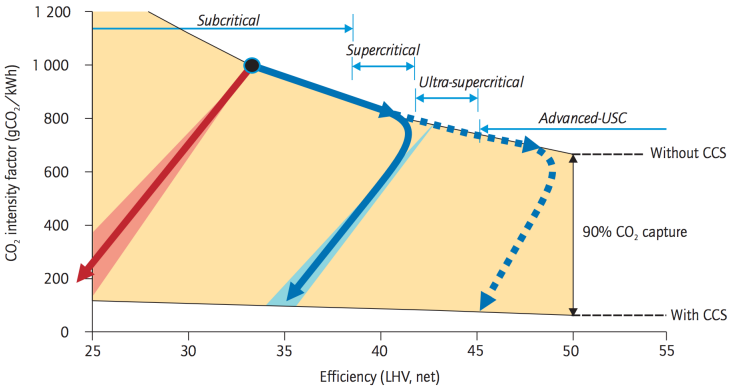

Figure 8: *Reducing CO2 emissions from pulverized coal-fired power generation from International Energy Agency (2012)*

is carbon capture and storage (CCS). CCS technologies retrieve CO_2 emissions of the exhaust stream from coal combustion or gasification and dispose them so that they do not enter the atmosphere. Once the CO_2 has been captured, it is essential that it can be safely and permanently stored. The World Coal Association (2005) proposed the roadmap towards zero CO_2 emission (Table 1).

Table 1: *The Coal-fired Routes to CO_2 Reductions*

Up to 5% CO_2 Reductions	**Up to 22% CO_2 Reductions**	**Up to 25% CO_2 Reductions**	**Up to 99% CO_2 Reductions**
Coal Upgrading Includes coal washing and drying. Currently used throughout the world.	**Efficiency Improvements of Existing Plant** Conventional subcritical plants have improved significantly in efficiency. Supercritical and ultra-supercritical plants offer even higher efficiencies and lower emissions.	**Advanced Technologies** Very high efficiencies and low emissions from innovative technologies such as IGCC, PFBC and in the future integrated gasification fuel cells (IGFC).	**Zero Emissions** Carbon capture and storage.

Proposed as CCS technologies for retrofitting coal-fired power plants, oxygen-enriched combustion (OEC) and oxy-fuel combustion of PC are practical solutions for the application of oxygen combustion to conventional furnaces (Chen et al. 2012). Research of OEC and oxy-coal technologies has been advancing in

recent years; however, there are still fundamental issues, such as heat transfer, flame structure, and flame stabilization, that must be addressed before this technology can reach its full potential.

Technical challenges

From the industrial aspect, advanced coal fired power plants are being built throughout the world. They meet the various energy and environmental standards required for commercial deployment currently (Makino 2016). However, the key issues are to ensure that coal can be utilized efficiently to satisfy future environmental regulations, particularly in the power sector (Minchener 2013). This requires advances in the development of clean coal technologies, together with the future introduction of oxy-coal combustion and CCS such that near zero emissions from coal can be achieved. The consequent R&D challenges include:

- Improve pollutant control, ensuring adequate interaction of individual components, leading to optimum combination of technologies that ensure compliance with present and future emission regulations. This would include characterization of the release of trace pollutants for the full range of fuel types, determining the influence of trace metal emissions on the removal of traditional pollutants (NO_x, SO_x and PM).
- Improve the use of more advanced combustion technologies such as oxy-fuel combustion. This is the case where burning coal in high-O_2 concentration environment rather than air. This eliminates the N_2 concentration found in air from the combustion process, resulting in flue gas composed of CO_2, H_2O, coal ash, and other gases. The high concentration of CO_2 and absence of N_2 also simplify separation of CO_2 from the flue gas for storage or beneficial use.
- Gain a better understanding of the operating conditions of the furnaces and coal combustion products to ensure the provision of robust systems. Optimize the cycles for better utilization of waste heat.
- Improve the flexibility of operation through dynamic modelling, control and instrumentation development, as well as development, selection and fabrication of new robust materials for furnace design.
- Develop the capability of power plants to cofire coal with biomass and other organic wastes.

While the major technology development programs are usually driven by the industry, there remains a significant role for the research community to provide valuable support, especially in fundamental research areas:

- Basic coal science is particularly important to the understanding of coal

utilization processes. For example, experimental studies along with simulated process conditions of advanced PC plants are in great need, such as volatile matter measured at realistic heating rates and temperatures, NOx emissions characteristics, advanced techniques for collection of in-flame data, effective techniques to measure corrosion and deposition rates.

- On-line monitoring of various species and conditions in coal-fired plants needs to be developed, especially non-intrusive optical techniques for the monitoring of coal flames.
- Modeling techniques are increasingly helpful with the development of computational fluid dynamics (CFD) and software tools. CFD modeling needs to be improved to reflect the latest findings of coal science such as the development of particle structure, pore diffusion and reaction within particles.

A good understanding of the PCC processes in industrial application is fundamentally important. However performing experimental tests on full-scale burners is not easy and can be rather expensive. For exemple, poor optical access, soot interference and the large dimensions of the coal burners make experimental measurements via laser diagnostics very difficult and mainly on laboratory-scale burners (Hwang et al. 2005; Molina and Shaddix 2007; Ribeirete and Costa 2009; Balusamy et al. 2013; Balusamy et al. 2015). Measurements of large-scale PCC boilers (Costa et al. 2003; Costa and Azevedo 2007; Li et al. 2008) are obtained using intrusive methods that can interfere with the local combustion processes. For this reason, CFD has been a helpful tool. In the case of PCC, CFD must be able to simulate turbulent two-phase flows interactions as well as coal conversion processes including the devolatilization, the homogenous combustion of the volatile gases and the heterogeneous reactions of the char.

Turbulent combustion modeling of PCC: state of the art

Complementary to experimental measurements, numerical simulations of PCC helps to gain better insight of the physical and chemical processes that are difficult to be detected by experimental methods. Also it plays an important role in the development of more efficient burners.

CFD methods for PC applications

CFD simulations have been performed over the past 50 years to predict the coal combustion behaviour. Currently, Reynolds-Averaged Navier Stokes (RANS) method is used as the industrial standard for modeling turbulent reactive flows,

due to its lower computational cost. However, RANS is only able to provide time-averaged flow quantities. When detailed information of the flow are necessary, Large Eddy Simulations (LES) offers the opportunity to predict the time-dependent flow variables.

RANS:

The first numerical studies of PCC were done in RANS during the 1980s. Truelove et al. (Truelove 1988; Truelove and Williams 1989) compared RANS simulations to experimental measurements of a 300 kW burner and also performed simulations of a full scale 40 MW burner. Lockwood et al. (Lockwood et al. 1980; Lockwood and Salooja 1983) performed simulations of the International Flame Research Foundation (IFRF) No. 1 furnace Weber et al. (1992) with reasonable agreement with experimental measurements of temperature and species mass fractions. Weber et al. (Smart et al. 1989; Peters and Weber 1997) also performed simulations of the IFRF No.1 furnace, and compared their results to more detailed experimental data for velocity and NO_x concentrations.

More recent CFD simulations of PCC have been performed in RANS on the burners developed in the Central Research Institute of Electric Power (CRIEPI) (Kurose et al. 2001; Kurose et al. 2004; Kurose et al. 2009) and the University of Leeds (Backreedy et al. 1999; Backreedy et al. 2006a; Ma et al. 2009; Gubba et al. 2012). Also, RANS simulations have been performed on oxy-coal burners. Andersson et al. (Andersson and Johnsson 2007; Andersson et al. 2008; Hjartstam et al. 2009) performed simulations of the Chalmers 100 kW oxy-coal test unit. The Aachen Pilot scale 100 kW burner has been investigated experimentally and numerically under different oxy-fuel configurations by a group of researchers (Toporov et al. 2008; Heil et al. 2009; Zabrodiec et al. 2017; Hees et al. 2016; Sadiki et al. 2017). Figure 9 compares the numerical results using RANS and LES from the work of Hees et al. (2016).

In order to improve the ability of RANS in the prediction of PC flames, much effort has been done to investigate the influence of different sub-models and assumptions. Hashimoto et al. (Hashimoto et al. 2012; Hashimoto et al. 2012) developed an improved model for coal devolatilization and introduced additional species in order to obtain a more realistic devolatilization model and this devolatilization model was subsequently validated based on RANS simulations. Korytnyi et al. (2009) developed a measurement methodology to obtain activation energies, pre-exponential factors for both devolatilization and char oxidation reactions in a pilot-scale cylindrical test furnace, which were subsequently used for RANS simulations of a full scale furnace. Zhao and Haworth (2014) developed a transported composition probability density function method using single and multiple rate devolatilization models in order to investigate the CRIEPI jet flame using RANS simulations.

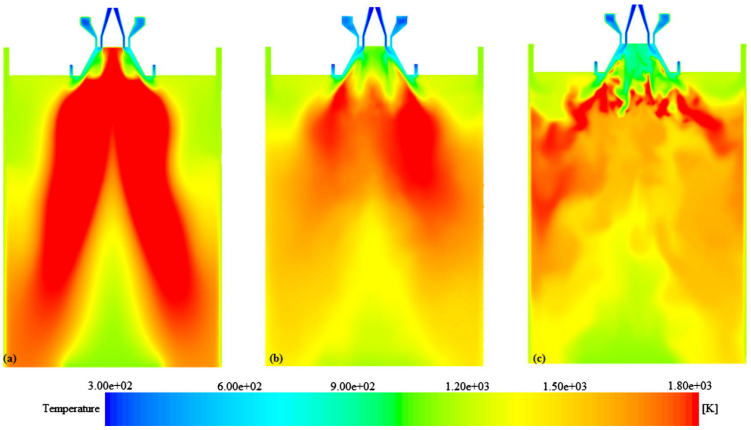

Figure 9: *Temperature contour plots (a) RANS (b) LES time-averaged (c) LES instantaneous of the Aachen burner from Hees et al. (2016)*

LES:

LES provides more detailed data than RANS, but it also requires more detailed validation data and higher computational cost. Many studies (Kurose et al. 2009; Bermudez et al. 2011; Hashimoto et al. 2012; Warzecha and Boguslawski 2014; Sadiki et al. 2017) compare RANS with LES results. The general conclusions are that RANS is useful for order-of-magnitude estimates, and gives an indication of the mean flow and scalar quantities and can be used to support burner development(Heil et al. 2009). However, even unsteady RANS approaches cannot capture the inherently non-linear transient turbulent processes occurring in PC burners. Instead, such processes are expected predicted by more advanced numerical approaches like LES. The first study of coal LES has been performed by Kurose and Makino (2003) of a hypothetical solid fuel flame, where the fuel was modeled as pure methane. Edge et al. (2011) and Gharebaghi et al. (2011) performed the first LES of a relatively large test facility (0.5 MWth and 1 MWth) . Both studies showed how LES can provide more detailed information than a RANS simulation, however there was not much comparison to experimental data. Yamamoto et al. (2011) performed a LES of a preheated pulverized coal jet flame where the comparison between experimental data and the simulations was limited to gas temperature, char burnout and flame lift-off height. Jovanovic et al. (2013) numerically analysed a system which uses oxygen and recycled flue gas in order to obtain improved ignition properties and flame stability. They demonstrated that the predictions of LES provide better agreement with experimental data than the corresponding results obtained from RANS calculations. Franchetti et al. (2013) conducted LES simulations of coal combustion process of a pulverized coal jet flame studied at the Japanese Central Research Institute of Electric Power and demonstrated good agreement with experimental data. Stein et al. (2013) used both Lagrangian

and Eulerian representations of the particles for LES simulation of a laboratory scale burner and obtained satisfactory agreement between experimental data and the predictions of LES simulations (Fig.10). Midou (2017) performed LES

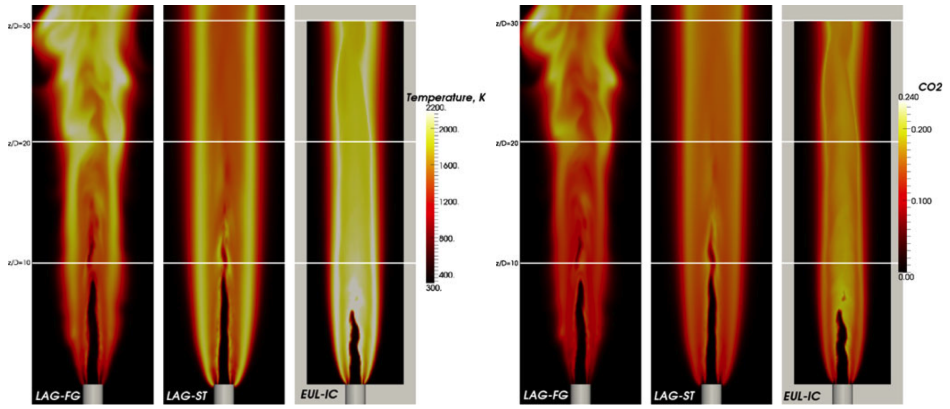

Figure 10: *Contour plot of the instantaneous gas temperature (left) CO_2 mass fraction (right) of the CRIEPI jet flame from Stein et al. (2013)*

with complex chemistry of a swirl-piloted pulverized coal burner studied by Balusamy et al. (2015). This configuration has been previously simulated by Muto et al. (2015) using two-step global reactions. The work of Midou (2017) showed the possibility of coupling complex chemistry with LES.

In terms of gas-phase turbulence modeling, many LES studies of coal flames (Edge et al. 2011; Warzecha and Boguslawski 2014; Rabacal et al. 2015; Olenik et al. 2015; Clements et al. 2015; Sadiki et al. 2017) mainly employed the eddy break-up model (EBU) or the eddy dissipation concept (EDC) concept. These studies considered global reactions for volatiles where two reactions describing the conversion of volatiles to CO and H_2O, and then the conversion of CO to CO_2. A third reaction is used to describe the conversion of a pilot gas such as CH_4. The volatile gas is treated as a postulate substance, because of lack of information such as the exact composition of the volatile species, also of reducing the computational cost.

Recently, the flamelet model, where the laminar flame structure is not influenced by turbulence, is introduced into coal LES. The flamelet model assumes reactions occur only in thin layers embedded in the turbulent flow field (Peters 1984). These thin layers maintain their structure in the turbulent flow field and can be described one-dimensionally as a function of mixture fraction. Watanabe et al. (Watanabe and Yamamoto 2015; Watanabe et al. 2017) used the flamelet model to study of a lab-scale coal jet flame and a large-scale combustion test of an actual pulverized coal burner. Rieth et al. (2016) (Fig.11) applies the flamelet model to simulate a semi-industrial furnace studied by Weber et al. (1992). Both studies obtained good agreement between experiment and simulations, which proved the suitability of the flamelet model in PCC-LES.

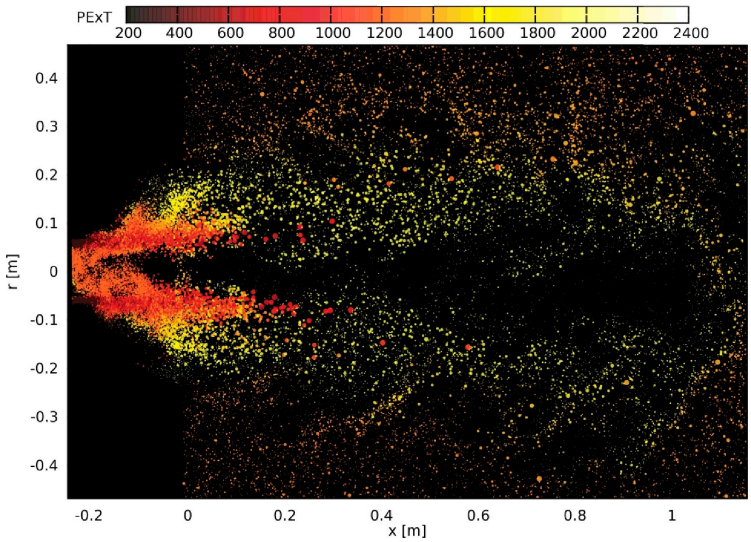

Figure 11: *Particles in the quarl region scaled by diameter and colored by temperature from the simulation of Rieth et al. (2016)*

DNS:

Compared to RANS and LES, the Direct Numerical Simulation (DNS) can give more detailed perspective on coal flames because the flow is directly solved. However, due to the extremely high computational costs, there are not many works on the DNS for coal combustion so far, and it is still unfeasible for industrial applications.

Luo et al. (2012) performed DNS of simplified coal combustion with point-source assumption to investigate the general characteristics of pulverized coal jet flow. Brosh et al. (Brosh and Chakraborty 2014; Brosh et al. 2015) applied the similar DNS methods to investigate the localized forced ignition of pulverized coal particle-laden mixtures in a cubic box domain initialized by an incompressible homogeneous isotropic turbulence. Hara et al. (2015) performed DNS to simulate the coal jet flame experiment of Hwang et al. (2005), using a global reaction scheme for the volatile matter of coal. Muto et al. (Muto et al. 2016; Muto et al. 2017) performed DNS of the same flame to investigate the chemical reaction in an ignition of mono-dispersed pulverized coal particle-laden flow using two-dimensional numerical simulation with detailed chemical reaction mechanism. Bai et al. (2016) (Fig.12) conducted three-dimensional DNS on the flame investigated by Hara et al. (2015); Muto et al. (2016); Muto et al. (2017). Rather than simulating the coal flame, recent studies using the approach of resolved single particle in quiescent fluid (RP-QF) or resolved laminar flow simulation (RLS/DNS) allows describing in detail devolatilization, fuel-oxidizer mixing and ignition in particle level. Vascellari et al. (2013) performed Euler-Lagrange simulations and RLS along with flamelet modeling to

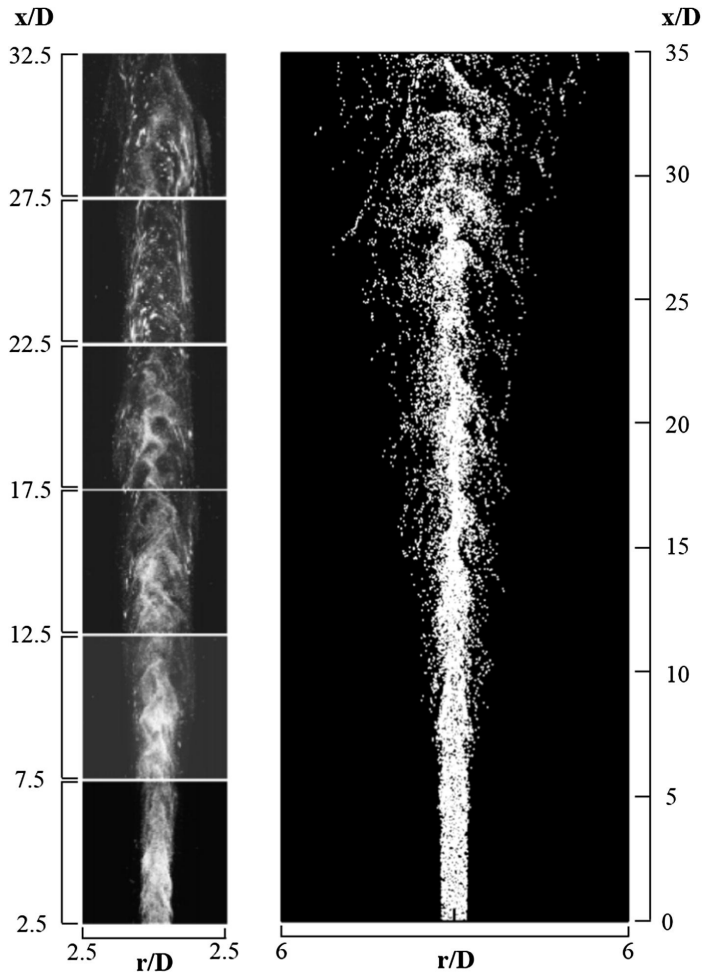

Figure 12: *The images of instantaneous pulverized coal particle positions: CRIEPI experiment (left) and DNS (right) from Bai et al. (2016)*

study single coal particle ignition. Tufano et al. (2016) extended the work of Vascellari et al. (2013) and performed RLS of single coal particle ignition with detailed pyrolysis boundary condition and studying the effect of gas phase chemistry. DNS of resolved particle allows analyzing the effects of kinetic related assumptions, detailed devolatilization and char oxidation models as well as radiation modeling and their sensitivity on the computational results on these models. These studies showed the potential to provide validation data for LES and RANS modelling.

Modeling challenges

CFD simulation has been proved to be an effective method to evaluate the performance of PCC. However, several problems remain if we want to improve the prediction of combustion characteristics, heat and mass transfer and pollutant formation in PCC.

- Coal conversion sub-models: Models for devolatilization, homogenous and heterogeneous reactions of volatile matter and char govern single particle level studies of PCC. The need for more accurate and sustainable modeling approaches and kinetic parameters asks for more detailed researches.
- Characteristics of different coal types: Due to the distinct physical properties and chemical structures, studies have shown various characteristics for coal of different ranks during devolatilization, volatile combustion, char burning, and pollutant formation. Their characteristics are essential for the accuracy of PCC modeling.
- Gas phase reactions: High-fidelity gas combustion mechanism should capture the chemical effects of coal volatile species, and provide accurate predictions of minor species and pollutant formations.
- Radiation modeling: Radiative heat transfer plays a major role in coal furnaces. Better turbulence-radiation and gas emittance/absorptance submodels are needed to improve the simulation of the temperature field.
- Turbulence modeling: Better predictive yet computationally economical models for different scales and types of applications are needed.

Thesis overview

PCC has been studied for the past century, but application of fundamental combustion research for industries is still limited due to the relations between different spatial and time scales and to the complexity of the combustion system. Also, the CFD of PCC requires a detailed approach to address issues related to two-phase flow, coal conversion modeling, heat transfer and pollu-

tant emissions. Thus, more investigations into these aspects are needed. Given the large number of processes and factors that occur in PCC, experimental and numerical studies of small-scale PCC are required to introduce a reliable and efficient methodology for realistic PCC modeling.

In order to fulfill the gap between validation of specific combustion sub-models, simulations of small-scale PC applications and those of real systems, some critical questions must be addressed:

- Which physical phenomena govern small scale coal combustion?
- Which type of experimental configuration is suitable for validation of coal sub-models?
- What are the information that are accessible by the measurements on this configuration?
- How to develop strategies for real systems based on small-scale applications?

Thesis objectives

Whilst devolatilization and gasification sub-models are involved in LES/RANS simulations of pulverized coal turbulent flames, their impacts on the flame structure and species concentrations still remains unclear. According to Peters (2000), instantaneous flame element embedded in a turbulent flow has the structure of a 1-D strained laminar flame. This elemental configuration, retained in many studies on gaseous (Lacas et al. 1992; Daguse et al. 1996) or two-phase flow flames (Franzelli et al. 2013; Alviso et al. 2015) is attractive to understand such fundamental coal combustion properties. The aim of the present study is to understand the physical phenomena that govern small scale coal combustion.

We have decided to start with a well-characterized laboratory scale laminar burner. This could help validating detailed coal sub-models, and in the long run, served as incorporating tabulation methods into a LES framework using a flamelet approach. Developing a novel configuration for investigations into PCC is the purpose of the present Ph.D. thesis entitled "Experimental and numerical studies of pulverized coal combustion in strained methane/oxygen/nitrogen flames".

The general objective of this Ph.D. thesis is to study the PC devolatilization and oxidation in a strained flow configuration. In order to stabilize the flame and to introduce a reference for comparison and validation of modeling, methane is used to assist the particle combustion process. Non-intrusive optical diagnostics are performed, which gives a good characterization of flame structure. However, the analysis of PC sub-models is also an important issue towards

better understanding and prediction of PCC. Thus, in the second part of this Ph.D. thesis, 1-D modeling of this axisymmetric configuration is proposed for its capability of producing accurate descriptions of the flame structure with less computational cost and without loss of accuracy. The focus here is on the development and validation of modeling methods applied to our experimental configuration. The problem of chemical structure of coal and kinetic studies for the sub-model parameters is outside the scope of this research.

Manuscript outline

The manuscipt consists of two parts:

- Part I: Experimental studies of pulverized coal devolatilization and oxidation

  - In Chapter 2, laboratory-scale studies of PCC are reviewed. The different flame diagnostics used for several configurations for investigations of flow conditions, coal conversion as well as heat transfer are compared and discussed.

  - The experimental configurations for our laboratory-scale strained flow burner are described in Chapter 3. Two optical diagnostics: measurements of OH^*, CH^*, and C_2^* spontaneous emission and flame emission spectroscopy are employed to investigate the flame structure and emission characteristics.

  - Chapter 4 explains the choice of the operating conditions. In particular, the post-processing methods for experimental data will be discussed in detail. A typical experimental result of the flame structure characterized by the diagnostic techniques employed is presented. Experimental results will then be used to validate the modeling procedure by comparing numerical simulations in a 1-D configuration.

- Part II: Numerical studies of pulverized coal devolatilization and oxidation

  - Chapter 5 introduces a literature review of coal conversion modeling, concerning the mains steps of coal combustion such as devolatilization, gasification and oxidation.

  - The aim of Chapter 6 is to specify the model formulations of fully-coupled 1-D configuration of laminar two-phase flow. This modeling method features sub-models that deals with conservation equations for different source terms, coupled with convective and radiative heat transfer through REGATH code.

  - In Chapter 7, the numerical setup and model parameters, as well as the mechanisms used in this work for chemiluminescence formation are

given. We validate the modeling approach by presenting a typical flame structure predicted by the simulations.

- Chapter 8 presents the comparison of experimental and numerical results, and the analysis and discussion of the modeling methodology. A comparative study for different operating conditions is conducted.

Part I

Experimental studies of pulverized coal devolatilization and oxidation

Chapter 1

Literature review of pulverized coal devolatilization and oxidation: experimental studies

This chapter focuses on reviewing various measurement techniques used in laboratory-scale experimental studies of the devolatilization and oxidation of pulverized coal. Special emphasis has been put on different configurations of laboratory-scale laminar flow burners. Finally, a brief summary of the advantages/limitations of the existing experiments is presented.

Experimental studies of pulverized coal combustion (PCC) at particle level have been performed in recent years. They are used to provide experimental data for the validation of theoretical and numerical investigations of the combustion process. Figure 1.1 shows a typical graphic presentation of the detailed time evolution that a coal particle typically undergoes together with its morphological change depending on particle diameter and heating rate. From an industrial point of view, it is vital to predict the time of total burnout of coal particles and the amount of heat emitted during combustion. Besides, a full understanding of the ignition modes and thermal processes taking place in a coal particle is also very important for the development of reliable kinetic models in turbulent combustion modeling.

The chief advantage of studying particle conversion in a laminar flow is the isolation of coal devolatilization and char oxidation phenomena from the influence of particle-turbulence interaction. Additionally, if the coal mass flow rate is relatively low, the behavior of group combustion can usually be neglected. These experiments are designed to determine related parameters including:

- Coal particle ignition time and temperature
- Combustion mechanism in given experimental conditions (homogeneous, heterogeneous, hetero-homogeneous combustion)
- Particular stages of particle combustion (pyrolysis, volatile combustion, char residual combustion)
- Impact of particle size and/or changing temperature conditions and/or varying gas composition on combustion behavior and particle burnout
- Particle mass loss during combustion
- Kinetic constants for coal conversion reactions in given experimental conditions

The experimental techniques to conduct investigations of coal devolatilization and oxidation behaviors differ to a great extent. These differences mainly come from the construction of the test rig, the nature of the coal sample, the temperature and heat transfer method of the reactor, the composition of the oxidant gas or carrier gas, and the measurement techniques. Also, as we saw in the introduction, experimental conditions are supposed to comply as accurately as possible with the assumptions of a theory or a model, because the dominant phenomena may be distinct under certain conditions. This chapter aims to review the latest experimental studies of coal devolatilization and oxidation, and especially the different measurement techniques and diagnostics commonly used in laboratory-scale experiments. They have been grouped based on the target phenomena and the type of the reactor used. The idea is to compare the advantages and limitations of those configurations, and therefore design and develop the most appropriate one for our study.

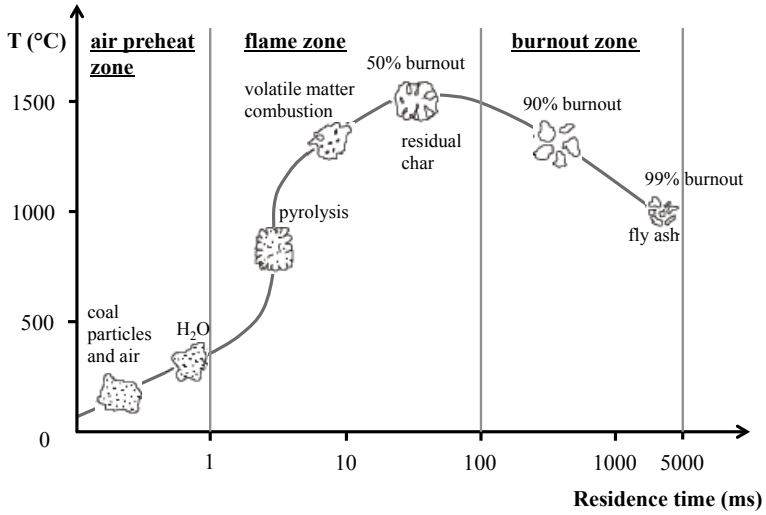

Figure 1.1: *Schematic of combustion process of a coal particle (diameter 10 - 100 µm) adapted from de Jong (2005)*

1.1 Mesurements techniques of laboratory-scale PCC experiments

Studying laboratory-scale coal flames can provide insights into different phenomena, such as particle ignition, char burnout, or the impact of coal particles on turbulent flames (Balusamy et al. 2013). It also simplifies the use of optical diagnostics that are useful in comprehensive studies of turbulent gas or two-phase flames. A precis of diagnostics used to study laboratory-scale coal flames is given in the following manner :

Velocity field

- Coded aperture (Shaddix and Molina 2009)
- Laser Doppler Velocimeter (LDV) (Hwang et al. 2005; Balusamy et al. 2015)
- Particle Image Velocimetry (PIV) (Balusamy et al. 2015; Lemaire et al. 2014; Xia et al. 2017)
- Shadow Doppler Particle Analyzer (SDPA) (Hwang et al. 2005)

Visualization

- Chemiluminescence (spontaneous emission) (Molina and Shaddix 2007; Hwang et al. 2005; Balusamy et al. 2013; Xia et al. 2017, this work)
- Laser Induced Fluorescence (OH-LIF) (Hwang et al. 2005; Balusamy et al. 2015; Xia et al. 2017)

- Mie scattering (Hwang et al. 2005; Balusamy et al. 2015; Hashimoto et al. 2016)
- Laser Induced Incandescence (LII) (Hayashi et al. 2013; Balusamy et al. 2015; Hashimoto et al. 2016)

Gas temperature

- Suction pyrometer (Butler et al. 1994)
- Thermocouple (Lemaire et al. 2014)
- Coherent Anti-stokes Raman Spectroscopy (CARS) (Hancock et al. 1992)

Particle temperature

- Two-color pyrometry (Hwang et al. 2005; Schiemann et al. 2009; Lemaire et al. 2014; Zabrodiec et al. 2017)
- Fit of emission with Plank grey body radiation (Zabrodiec et al. 2017)

Gas species

- Suction probe to analyzer (CO, CO_2, H_2O, NO, SO_2) (Lemaire et al. 2014)
- Flame emission spectroscopy (FES) (Smolarz et al. 2012; Parameswaran et al. 2014; Yan et al. 2017, this work)

In order to analyze the combustion process of PCC in small laboratory burners (e.g. the counter-flow burner used in the present study), the experimental setup can be equipped with several kinds of non-intrusive optical diagnostics. They are widely used in flow field measurements, visualization of coal particle combustion, temperature (coal and gas) or species concentration measurements. However, these diagnostics differ largely in temporal, spatial as well spectral resolutions. Most commonly employed approaches found in the literature are presented in the next section with examples of application.

1.1.1 Spontaneous emission

In the combustion zone, the electronically excited species are formed from the intermediate ground state species. These excited species are highly reactive. They return to the ground state by emitting radiation in form of light, as shown in Fig.1.2. Chemiluminescence is the emission of light ($h\nu$) as result of molecules returning to the ground state which are excited chemically.

Spontaneous emission of chemiluminescent species is responsible for ultra-violet and visible light in the combustion process. It offers an optical diagnostic tool for the observation of flames due to its natural occurrence. Three main radicals for this emission can be identified in hydrocarbon flames: OH^* (around 310 nm), CH^* (around 431 nm) and C_2^* (around 516 nm). These radicals are naturally

present in the reaction zone and are used to determine important macroscopic properties such as flame location, flame speed, and heat release rate evolution. In premixed conditions, the OH^* chemiluminescent signal is often considered to be proportional to the heat release of flame. Images of flame chemiluminescence are typically acquired on CCD cameras equipped with band-pass filters for spatially resolved measurements.

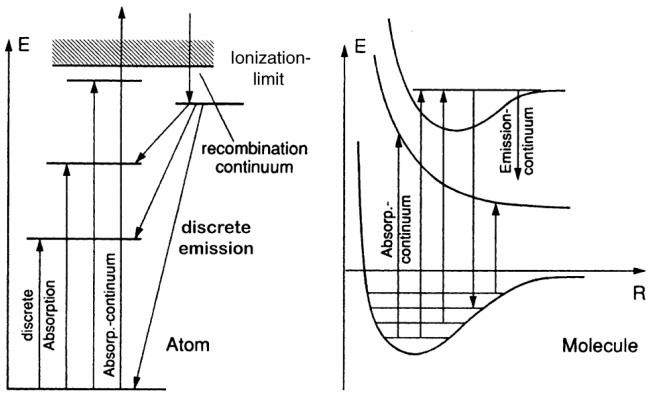

Figure 1.2: *Schematic diagram to illustrate the origin of discrete and continuous absorption and emission spectra for atoms (left) and molecules (right) from Demtröder (2008)*

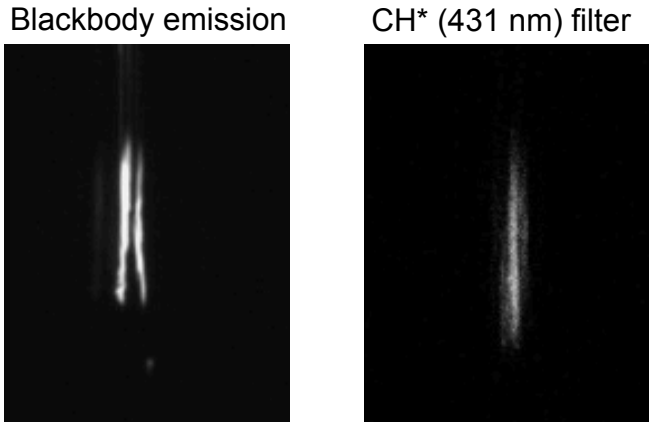

Figure 1.3: *Comparison of backbody emission (filterless image) and chemiluminescent CH^* emission of the Sandia single-particle burner from Molina and Shaddix (2007)*

Burning coal usually results in luminous yellow flames, and C_2^* and CH^* emission can be observed in such flames (Gaydon 1957). While the OH^* radical seems more suitable for lean flames, CH^* and C_2^* have a more monotonic behavior and stronger dynamics for richer flames (Docquier et al. 2000). Thus,

CH^* chemiluminescence intensity is used to observe luminous flame structure and is considered to be a good representative of the heat release rate (Lacas et al. 2005). Molina and Shaddix (2007) also measured CH^* chemiluminescence signals as a better indicator for the onset of pulverized coal particle ignition and the volatile reaction zone (Fig.1.3). The measurement of C_2^* chemiluminescence has also been proved to be useful for validating coal sub-models in the present configuration by Xia et al. (2017).

However, the main challenge of measuring chemiluminescence signals with band-pass filters is that it is often extremely difficult to eliminate the impact of certain emissions, such as the CO_2 spectrum as well as blackbody emission, the most affected being the CH^* and C_2^* signals. It makes the quantification of radical concentrations and the comparison with numerical studies relatively difficult.

1.1.2 Planar Laser-Induced Fluorescence (PLIF)

Laser induced fluorescence (LIF) is a non-intrusive optical diagnostic, which is able to measure spatially and temporally the induced fluorescence of molecules. The excitation is obtained by directing a laser beam towards the target molecule. If the laser beam is introduced as a thin sheet, the molecules located in this sheet are excited. Then one can take 2-D images from the fluorescence of the molecules contained in this 2-D plane. This technique is Planar Laser induced fluorescence (PLIF). The main interest of PLIF is to obtain the relative intensity profiles corresponding to the relative concentration of intermediate species such as OH and CH, or pollutant such as NO and PAH. The measurement of OH-PLIF has been proved to be useful for validating coal sub-models in the present configuration in our previous study (Xia et al. 2017).

1.1.3 Mie scattering

When light encounters particles, it is scattered in a way that depends on the particle size given the light wavelength. When the wavelength and the particle diameter are comparable, the applicable light scattering theory is Mie scattering. When applied to coal particles, signal from each particle can be obtained to get information on its position. The overall signal is thus dependent on the particle number density and the size of each particle. The scattered light by the particles can be used to collect images of their 2-D spatial distribution.

Simultaneous measurement system for OH-PLIF and Mie scattering image of pulverized coal particles are used by Hwang et al. (2005) and Balusamy et al. (2015) to examine the spatial relations of combustion reaction zone and pulverized coal particles (Fig.1.4).

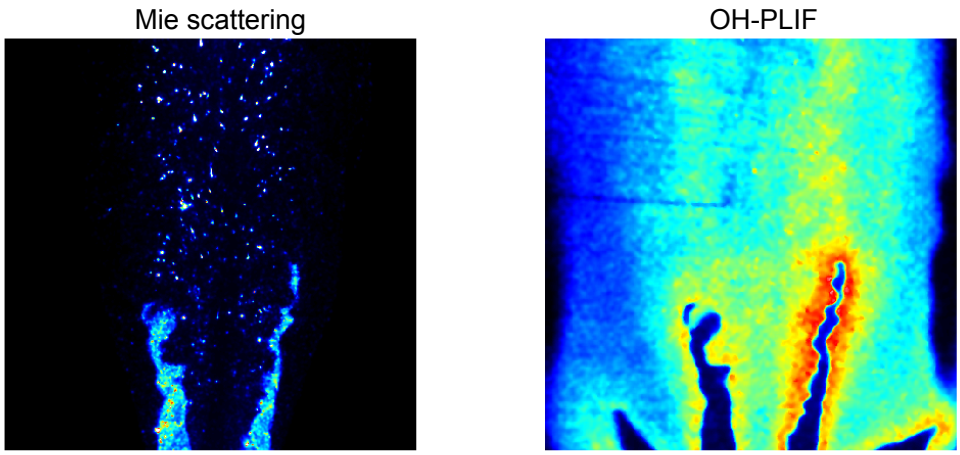

Figure 1.4: *Instantaneous two-dimensional images taken simultaneously using Mie scattering and OH PLIF from Balusamy et al. (2015)*

1.1.4 Velocimetry techniques

Measurements of the flow field of coal particles can be obtained by using laser diagnostic techniques such as laser Doppler velocimetry (LDV) and particle image velocimetry (PIV), which are based on the Mie scattering signal from particles. LDV is a point-based measurement, which is widely used in spray and solid combustion. It is time-consuming for the characterization of the entire flow field. The alternative is PIV, which allows vectors measurement across the field at a given instant. The principle of PIV is to estimate the displacement of a particle between two instants from its Mie scattering signal recorded on two successive images. A plane within the flow is illuminated by laser, creating two laser sheets with a small time delay. This delay depends on the mean flow velocity and the resolution of the images. The light scattered by the particles is then acquired in a sequence of images. The displacement of particles between subsequent images is then calculated through correlation of images (Agarwal 2013). In our previous study (Xia et al. 2017), PIV measurements have been performed to prove that the particle average velocity matches the gas velocity at the injector exit.

Balusamy et al. (2013) compared LDV and PIV measurements (Fig.1.5) using alumina and coal particles of a laboratory-scale annular pulverized coal burner. They concluded that PIV measurements are affected by the size distribution of coal particles, whereas LDV measurements turned to be biased toward the velocity of small particles.

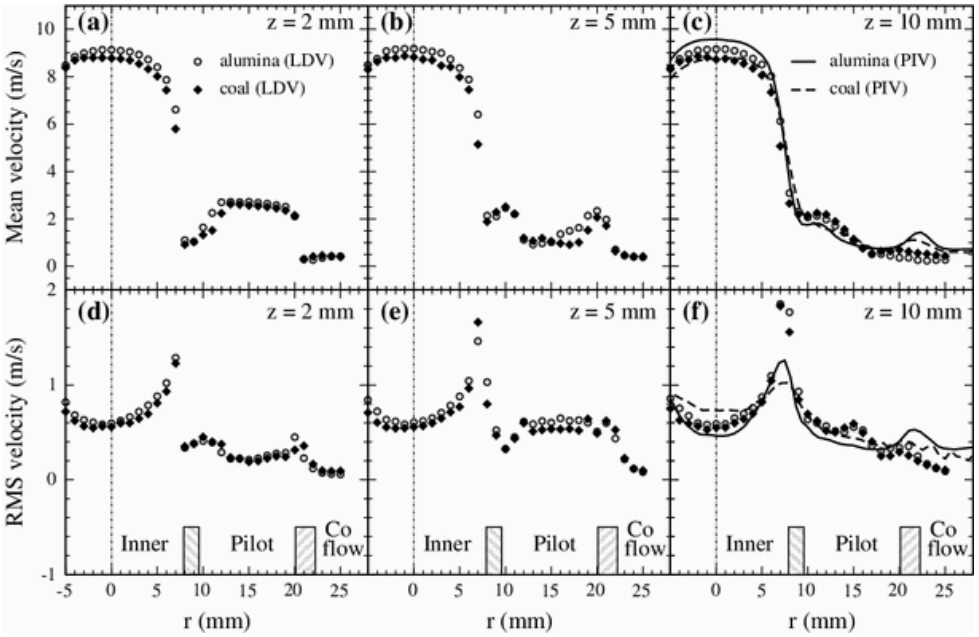

Figure 1.5: *Instantaneous two-dimensional images taken simultaneously using Mie scattering and OH PLIF from Balusamy et al. (2013)*

1.2 Laboratory-scale apparatus of PCC

Most practical PCC systems operate under turbulent conditions, where the heat release is more efficient than under laminar conditions. The study of chemically reacting turbulent flows, such as PCC, is really challenging because of interactions between chemistry and turbulence, along with solid phase conversions. In laminar flows, however, the measurements of velocity, temperature, and concentration will obtain quite smooth profiles (Kuo 2005). Therefore, laboratory-scale laminar flow burners are preferentially used for the investigations of PCC, especially of coal kinetics and ignition behaviors. In this section, three types of laminar flow experiments which have been commonly used in the literature are introduced.

1.2.1 Thermogravimetric Analysis (TGA)

Thermogravimetric analysis (TGA) is one of the most common techniques used to investigate thermal conversion and kinetics of coal pyrolysis (Reverte et al. 2007; Shi et al. 2013; Aboyade et al. 2013; Seo et al. 2011). It provides weight loss history of the coal sample as a function of time and temperature. It is also used to perform the proximate analysis of coal samples (see section 4.1.1). A thermogravimetric analyzer is a combination of an electronic microbalance with

a furnace, a temperature programmer and computer for control, that allows the sample to be simultaneously weighed and heated or cooled in a controlled manner, and the mass, time, temperature data to be captured (see Fig.1.6). The kinetics of coal conversion can be determined by the application of the Arrhenius equation corresponding to the separate slopes of constant mass degradation during the pyrolysis. TGA has also been widely used for the determination of ignition temperature and combustion characteristics of coal (Tognotti et al. 1985; Hurt and Gibbins 1995; Zolin et al. 1998; Le Manquais et al. 2009; Li et al. 2014). The temperature is typically from low to moderate at relatively slow heating rates, with high accuracy and time resolution. However, the heating rate is usually about 3∼200 K/min, which is not comparable to the actual heating rate in practical coal furnaces.

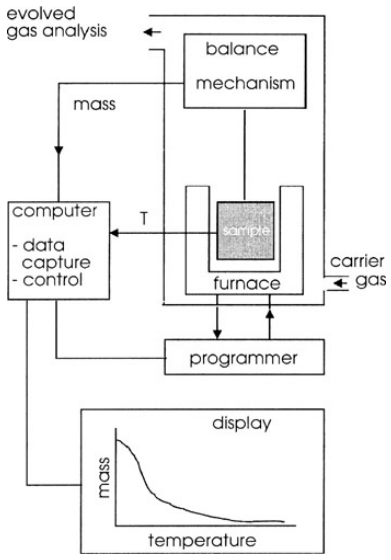

Figure 1.6: *Schematic of thermogravimetry from Brown (2001)*

1.2.2 Drop tube furnace (DTF)

Complementary to TGA, drop tube furnaces (DTF) are designed for laboratory experiments under similar conditions in temperature and residence time as those of industrial boilers and power plants (Authier et al. 2015; Wang et al. 2014; Li et al. 2012; Riaza et al. 2014; Khatami et al. 2012). DTFs are usually electrically heated, and the wall temperature is maintained constant. The coal particle is rapidly heated to a controlled temperature and completes devolatilization in a short residence time. A heating rate of 10^5 K/s and maximum temperature of 1700 °C can be achieved in the DTF. In addition, free-falling coal particles are in a dynamic, dilute phase, which allows for individual and group particle combustion.

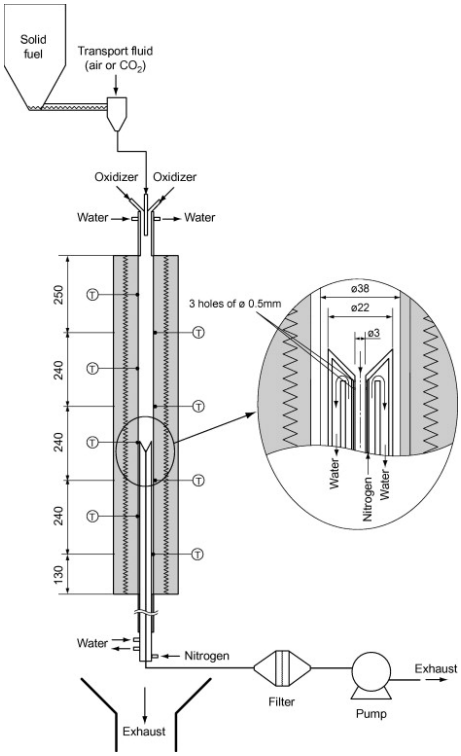

Figure 1.7: *Schematic of a drop tube furnace from Wang et al. (2014)*

DTF can also be used for kinetic analysis of pulverized coal devolatilization and combustion characteristics under inert or reactive gaseous atmosphere. Bejarano and Levendis (2008) investigated the combustion of single coal particles in air- and oxy-combustion environments. Zhang et al. (2010) examined predried coal combustion characteristics in a DTF and concluded that oxy-coal combustion showed different behavior in pyrolysis, volatiles ignition and oxidation, char oxidation rate and surface temperature, comparing to conventional air combustion. Khatami et al. (2012) studied the ignition characteristics of single coal particles of various ranks. Wang et al. (2014); Wang et al. (2014) reported gas temperature, major gas species concentration and particle burnout measured along a DTF (Fig.1.7) of various coal type, particle size distribution and oxy-fuel atmospheres. Köser et al. (2015) studied the combustion characteristics of individual coal particles in an oxygen-enriched environment using high-speed OH-PLIF. Bai et al. (2017) carried out experimental investigations into the combustion behaviors of single pulverized coal particles based on high-speed imaging and image processing techniques.

Figure 1.8 shows the difference of heating rate between slow TGA and fast DTF systems. The mass loss rate of both systems is successfully predicted for a wide range of thermal conditions by optimization of the two-step reaction model, which will be introduced in Chapter 4.

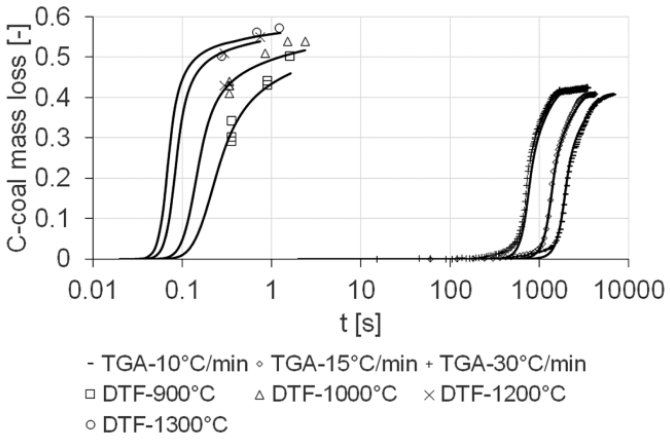

Figure 1.8: *Normalized mass loss versus time from the devolatilization of Calenturitas coal in TGA and DTF (dots: experimental data; lines: modeling results) from Authier et al. (2015)*

1.2.3 Entrained flow reactor (EFR)

Another type of laminar flow PCC burner is entrained flow reactor (EFR), which is designed for introducing coal particles into well-characterized, preheated gas stream. Heating rates as much as 10^6 K/s can be achieved using a Flat Flame Burner (FFB). This burner is a flow reactor with premixed/non-premixed gaseous fuel and air injected through a honeycomb grid. The gases ignite, forming a uniform thin flame sheet. Coal particle and carrier gases are injected through a narrow tube in the center of the burner slightly above the tip of the flame sheet at a certain velocity. The advantage of this kind of single particle experiment is that it focuses only on phenomena directly related to the coal conversion and in the boundary layer around the particle. It also reduces complexity compared to large scale reactors. In this cofiguration there is no interactions with other particles or turbulent flows, which is good for development and calibration of kinetic models.

Ignition of single coal particle during devolatilization was investigated by Shaddix et al. (Molina and Shaddix 2007; Shaddix and Molina 2009; Liu et al. 2011), using optical diagnostics for estimating ignition. Experiments were conducted in the laminar optical FFB (Fig.1.9). The reactor operates at 1 atm and uses a non-premixed-flamelet Hencken burner to provide a high velocity flow of combustion product gases. Coal particles are injected at the furnace centerline with different feeding rates. The experimental results from chemiluminescent imaging and pyrometry are used to develop and validate coal conversion modeling.

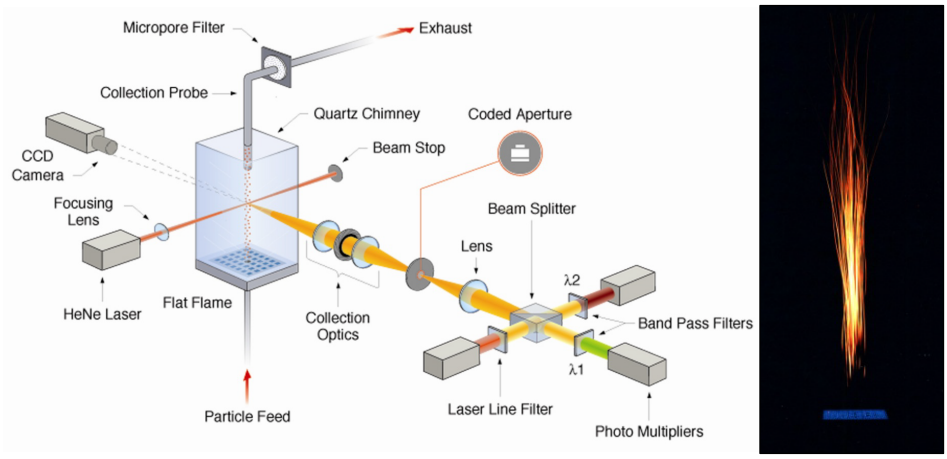

Figure 1.9: *Schematic of the a flat-flame burner (left) and a typical coal jet flame (right) from Molina and Shaddix (2007)*

Schiemann et al. (2009) analyzed the firing and combusting behavior of coal particles in a FFB, which the coal conversion during the whole combustion process can be tracked via optical diagnostics. The coal particles are injected into the heated combustion chamber through a small borehole metered by a mechanical coal dozer. A quartz tube separates the hot stream of combustion gases from the surrounding atmosphere and provides optical access during the whole process, from firing to complete burnout. A two-color pyrometry system was used to study the combustion of coal and chars. This camera system is based on two cameras, which allows studies on the combustion temperature and size evolution of coal char particles. The measurements can be used to calculate char burning kinetics.

Lemaire et al. (2014) conducted characterization of a similar test bench (Fig.1.10) designed to study the devolatilization and oxidation of pulverized coal particles. A premixed propane/air laminar flat flame is stabilized on the porous media generating hot gases for a heating rate of approximately 10^6 K/s. The inert or oxidant carrier gas stream is injected in the centerline of the burner along with coal particles. They also performed numerical simulations to characterize the velocity and temperature fields in the reaction chamber. Measurements of particle image velocimetry, two-color pyrometry and the composition of the burnt gases have been characterized.

Figure 1.11 gives the gas and particle temperature history from the correlation of velocimetry measurement and distance (height above burner, HAB). Similarly, devolatilization yield profiles are available for the validation and optimization of coal pyrolysis models.

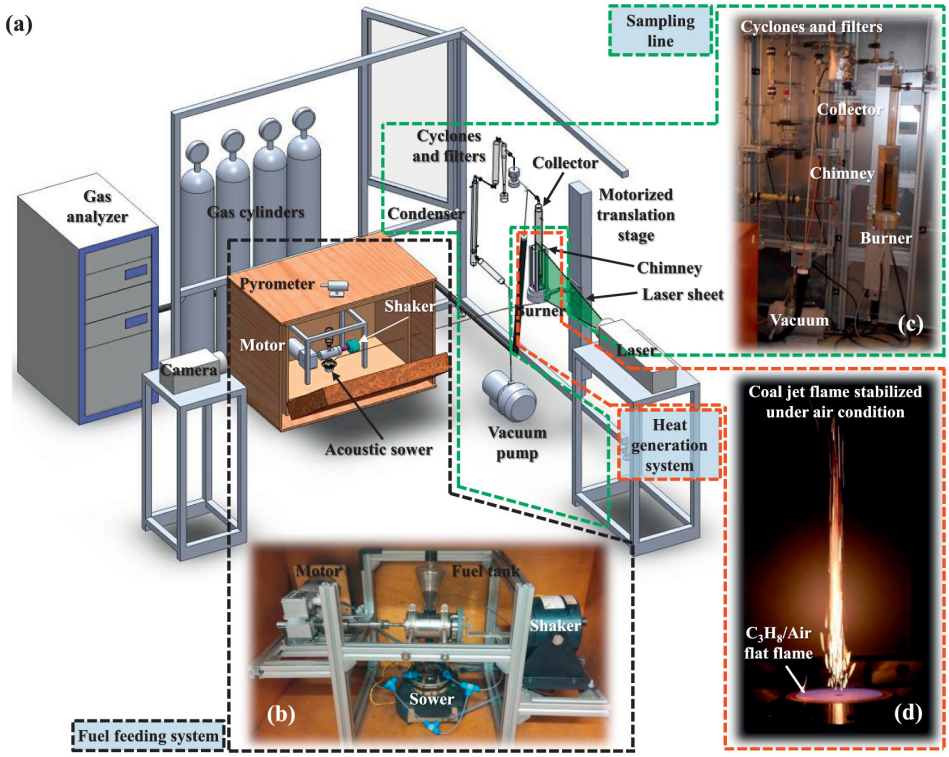

Figure 1.10: *(a) CAD representation of the experimental test bench, (b) pictures of the fuel feeding system, (c) the sampling line for char and combustion gas analyses, and (d) a typical coal jet flame stabilized on the FFB using air as a carrier gas from Lemaire and Menanteau (2016)*

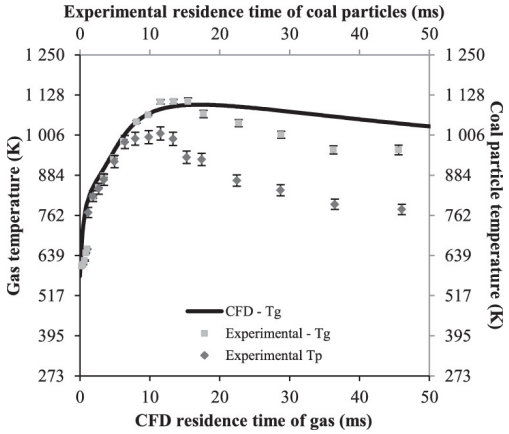

Figure 1.11: *Comparison between gas temperatures T_g obtained by CFD and thermocouple measurements with experimental coal particle temperatures T_p measured by pyrometry as a function of the residence time in the reaction chamber from Lemaire and Menanteau (2016)*

1.3 Summary

This review of laboratory-scale laminar PCC burners for the study of coal devolatilization and oxidation can be summarized in the Table.1.1. The main advantages as well as certain limitations related to each configuration are explained. It is furthermore noteworthy that all the current test benches focus on the description of fundamental processes taking place during the combustion of coal, such as heat and mass exchange or reaction kinetics. However, most of them are not able to reproduce the operating conditions of real coal furnaces.

Another very important factor when making choices of experimental design is the modeling issues. The CFD of coal flames requires a detailed approach to simulate aspects including two-phase flow, coal conversion modeling, heat transfer and pollutant emissions. The modeling of current configurations generally remains in the validation of coal kinetic models. The simulation of particle-gas coupling under laminar flow conditions is often simplified. It seems that the gap between specific combustion sub-models and the simulations of real PCC systems has not been fulfilled yet. Therefore, the development of a novel configuration for the investigations into coal devolatilization and oxidation is in great need.

Table 1.1: *Summary of laboratory-scale laminar configurations for the investigations of pulverized coal devolatilization and oxidation*

Type of reactors	**Advantages**	**Limitations**
TGA	- precise control of temperature and residence time; - simplicity in implementation and utilization; - good repeatability; - varying atmosphere;	-low heating rate (3∼200 K/min); - non-uniform diffusion of oxidizer within the sample; - ash formation at the surfaces of particles.
DTF	- high and homogeneous gas temperature; - high heating rate (10^5 K/s); - varying atmosphere;	- relatively difficult real-time analysis; - repeatability and reproducibility.
EFR	- possible pilot flame; - high heating rate (10^6 K/s); - varying atmosphere; - easy optical access;	- evacuation of burnt gases mixed with volatile gases.

Chapter 2

Experimental configuration of pulverized coal devolatilization and oxidation in strained $CH_4/O_2/N_2$ flames

This chapter presents the experimental setup chosen for studying PCC in laminar strained premixed methane/oxygen/nitrogen flames. The description of the burner, the setup of positioning system as well as the coal feeding system are explained. We then present the two optical diagnostics used to investigate the flame structure and emission characteristics: measurements of OH^*, CH^* and C_2^* spontaneous emission and flame emission spectroscopy (FES).

A geometrically simple strained flow can be obtained by injecting a laminar gas flow against a stagnation plane (a wall, for example). The axial velocity of the impinging jet vanishes at this plane. If the mixture is ignited in close proximity of the stagnation plane, a stable flame with a flat-circular structure is obtained (Darabiha et al. 1993). Figure 2.1 shows a direct view of a flat CH_4/air flame. In this counterflow configuration, the flame front is located at a fixed position in space, where flow speed equals the flame speed, determined by the equivalence ratio of the fresh gas mixture and by the strain rate.

As seen in the introduction, flamelet is one of the most promising turbulent PCC models because it can take into account detailed chemical kinetics at a reasonable computational cost (Vascellari et al. 2013; Watanabe and Yamamoto 2015; Rieth et al. 2017). Commonly-used flamelet approaches are referred as flamelet-based tabulated chemistry methods where the turbulent flame structure is modeled by an ensemble of single flamelet elements generally assuming single/muitiple burning regime(s). Tabulation strategies using laminar strained flame configuration for spray flames have been discussed by Franzelli et al. (2013) and recently applied to PCC by Messig et al. (2017).

Because this type of flame is well suitable for the development of numerical models, especially 1-D simulations, and optical measurement techniques, this system has been commonly used in the case of gaseous (Lacas et al. 1992; Darabiha et al. 1993) and spray reactants (Franzelli et al. 2013; Alviso et al. 2015). But only a small number of studies, dated back to the 1980s, deal with coal particles (Graves and Wendt 1982; Wendt et al. 1988), where the characteristics of laminar opposed jet premixed/diffusion pulverized coal flame were studied.

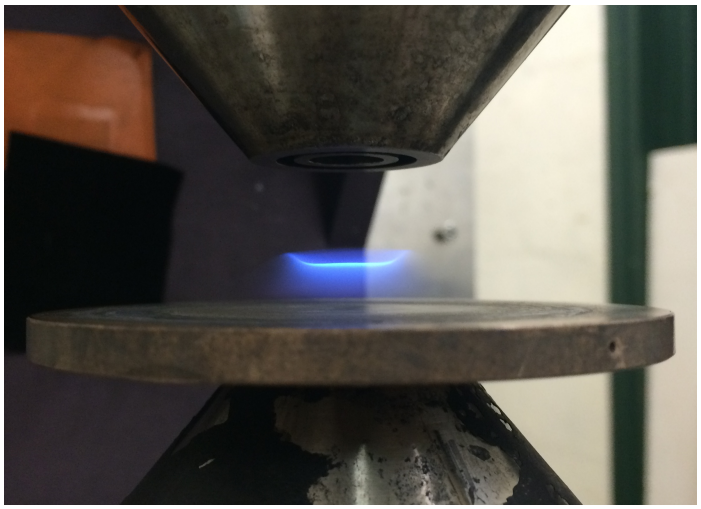

Figure 2.1: *Direct view of a methane/air flat flame*

In the present study, experiments of premixed laminar flames (Fig.2.2) established by the strained flow of monodisperse coal particles with a stream of $CH_4/O_2/N_2$ are performed at atmospheric pressure. This chapter aims to present the exprimental configurations and measurement techniques used in this work.

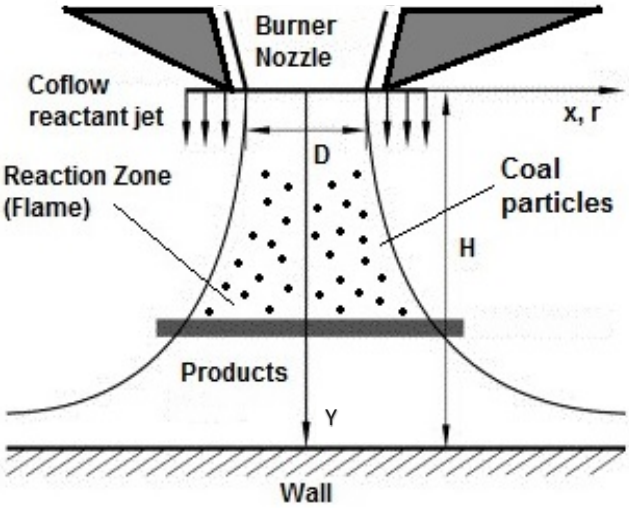

Figure 2.2: *Schema of the strained flame with coal particles*

2.1 Description of stained flow burner

The experiments are carried out using a strained flow burner as illustrated in Fig.2.3. A premixed $CH_4/O_2/N_2$ stream, carrying the pulverized coal particles, exits an axisymmetric convergent nozzle of 10 mm inner diameter. The flow then impacts a horizontal metallic brass wall. The distance between the nozzle and the wall is kept constant to 20 mm in all experiments. When ignited, a laminar flame front appears at a given distance from the wall, where the laminar flame speed equals the flow velocity. A co-flow of nitrogen is injected in order to prevent the flame from ambient air perturbations. The hot gases issued from the combustion of $CH_4/O_2/N_2$ mixture flow between the flame front and the wall. Pulverized coal particles start burning at the CH_4/O_2 flame front and the hot region promotes heating, pyrolysis and oxidation of the pulverized coal particles.

To our knowledge, there is no previous experimental studies of coal/air flames with a similar configuration. The introduction of methane in the mixture makes possible the ignition the coal particles. Bradley et al. (2001) argued that is very difficult to ignite and stabilize small pulverized coal flames under atmo-

spheric conditions. Also it is practically impossible for coal particle ignition without preheating (Bradley et al. 2006). However, we have found that it is not necessary to add a preheating system because the methane flame provides the heat to ignite and stabilize the coal flame (Xia et al. 2017). In addition, the CH_4/O_2 flame can be considered as a reference for the optical measurements.

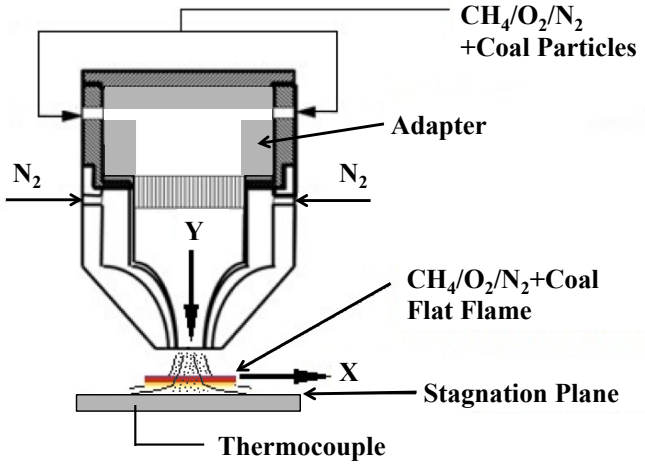

Figure 2.3: *Schema of the strained flow burner*

There are two important parameters to obtain a stable flame: the equivalence ratio, and the strain rate. The equivalence ratio of the gas mixture $CH_4/O_2/N_2$ is defined by

$$\Phi = \frac{Y_{fuel}/Y_{oxygen}}{(Y_{fuel}/Y_{oxygen})_{stoichio}} \tag{2.1}$$

where Y_i is mass fraction of the fuel and oxydizer and "stoichio" refers to stoichiometric conditions. The strain rate is defined as:

$$\epsilon = \frac{2V_u}{H} \tag{2.2}$$

where H is the separation distance between the burner nozzle and the flat plate and V_u is the is the velocity of reactants injected from the burner nozzle.

2.2 Experimental setup

2.2.1 Coal feeding system

Lignite coal briquettes (Heizprofi braunkohle) are grounded in an electrical grinder and sieved manually (sieve size = 100 μm) to obtain pulverized coal samples. Prepared samples were examined under an optical microscope in order

to determinate the granulometric properties of the coal particles. Figure 2.4 shows an typical image acquired by the microscope. Figure 2.5 presents the particle size distribution as an histogram from the processing of 100 images in which 56986 particles where identified and analyzed. The distribution is also summarized in Table 2.1. From the particle analysis, the mean particle diameter value of 11.42 μm is obtained, and the Sauter mean diameter D_{32} of the coal particles is 15 μm (Xia et al. 2017). More properties of coal briquettes are presented in Appendix A.

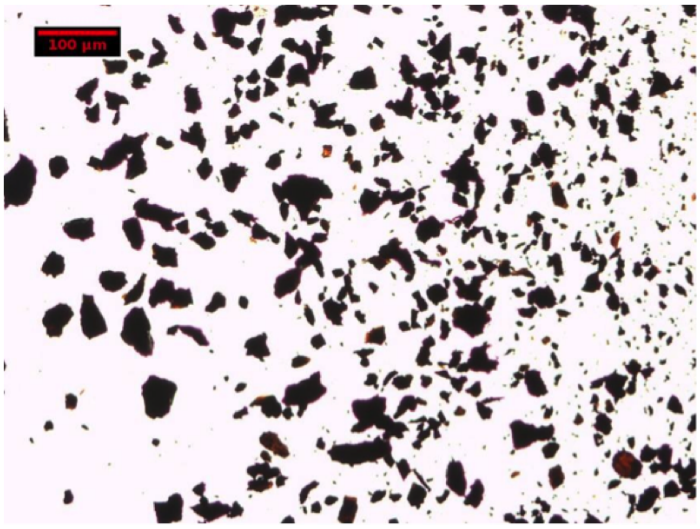

Figure 2.4: *Sample image obtained from optical microscope*

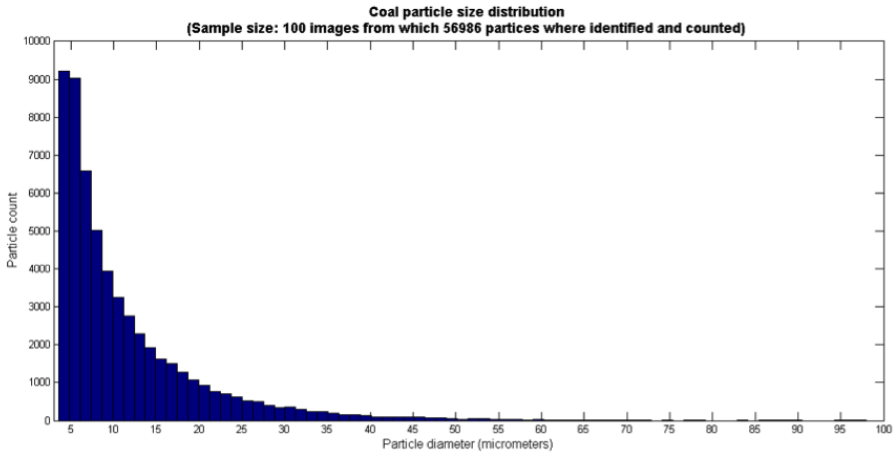

Figure 2.5: *Histogram of coal particle size distribution*

Table 2.1: *Particle size population distribution of processed coal particles*

Diameter range (μm)	Particle count	Population percentage (%)
0-20	49530	86
20-40	6441	12.21
40-60	890	1.57
60-80	121	0.2
80-100	14	0.02

The coal feeding system consists of three cylindrical tubes, showed in Fig.2.6. A porous sintered disk is placed between the top and the middle tubes. Pulverized coal samples are stocked on top of the porous disk. O_2/N_2 mixture is injected through four inlets at the bottom tube, passing through a honeycomb disk first before crossing the porous disk. The gas mixture carries coal particles out of the top reservoir.

So as to achieve a stable feeding rate of coal particles to the burner, we must be able to control the coal mass flow rate. However, it is difficult to find commercially-available equipment to fluidize, measure and control this parameter in real time. Therefore we connected the coal feeder to a collection container weighed by a precision weight balance. The value of the collected coal is recorded in regular time intervals (3-minutes, 5-minutes, half-hour and one hour), and the measurement runs length is set to one hour in each test. Figure 2.7 shows curves obtained from four runs with constant initial coal load in the reservoir. The tests gave an average flow rate of 0.5 g/h. However, due to the inhomogeneous nature of coal particles and the small mass flow rate, the uncertainty of the measurement is about 50%.

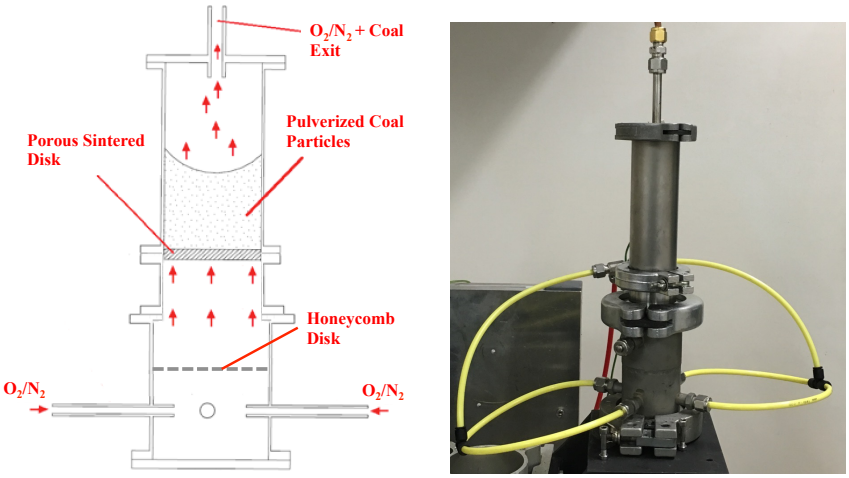

Figure 2.6: *Schema and photo of the coal reservoir*

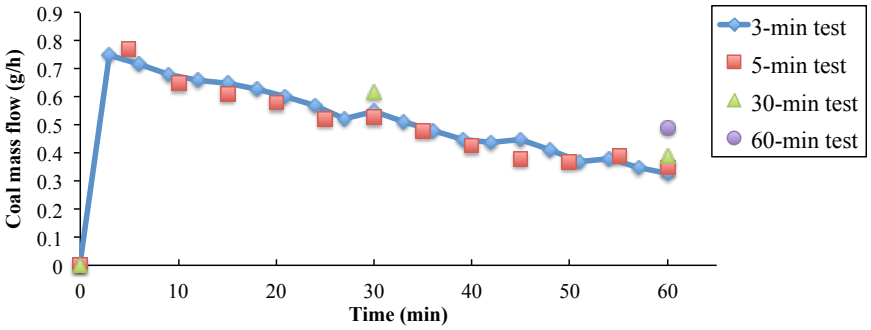

Figure 2.7: *Measured coal mass flow rate vs time, initial coal load 20 g*

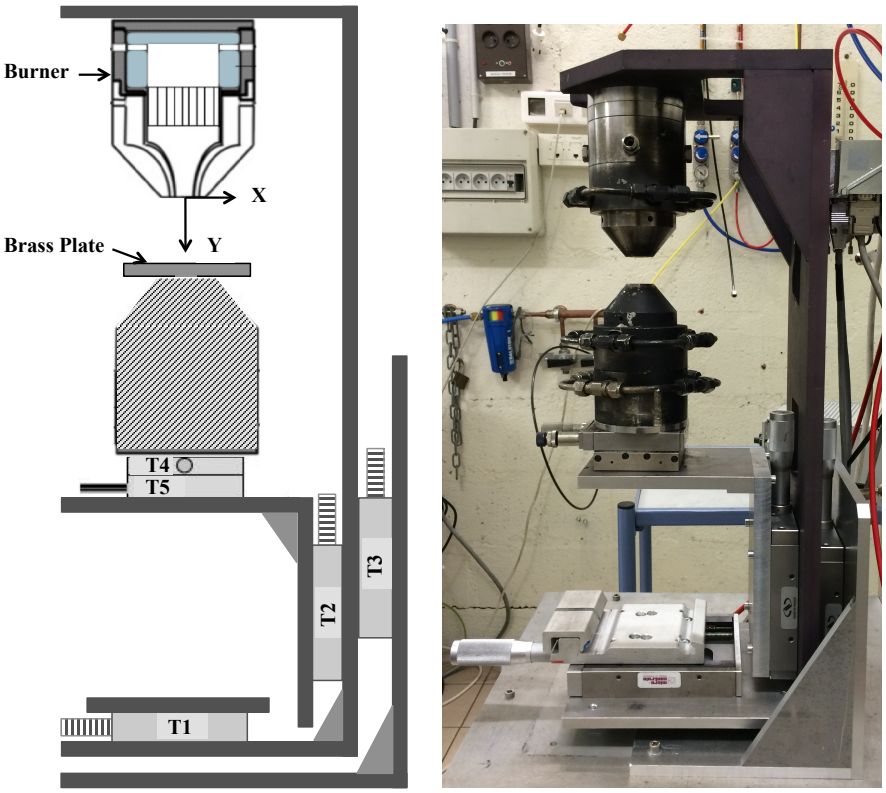

Figure 2.8: *The strained flow burner with the micro-positioning system*

2.2.2 Mechanical system

The positioning of the burner and the collimation of the optical path is carried out through 5 manual linear translation/precision positioning stages as illustrated in Fig 2.8. Translation T1 is used to align the lens with the centerline of the burner. The distance between the burner and the brass wall is controlled

by T2. Translation T3 moves the whole burner system assembly in the vertical direction. The other two translations (T4 and T5) are arranged in the bottom of the lower burner (adopted from a counterflow position) to position the wall coaxial with the burner. This system allows exploring the whole flame zone without moving the optics or diagnostics.

2.2.3 Flow control system

The gaseous flows are controlled by thermal mass flow meters (Bronkhorst EL-FLOW). Figure 2.9 shows the schematic diagram for the gas flow control system. The maximum flow capacities for each mass-flow meter are showed in Table 2.2. These devices are coordinated with a LM-50 controller.

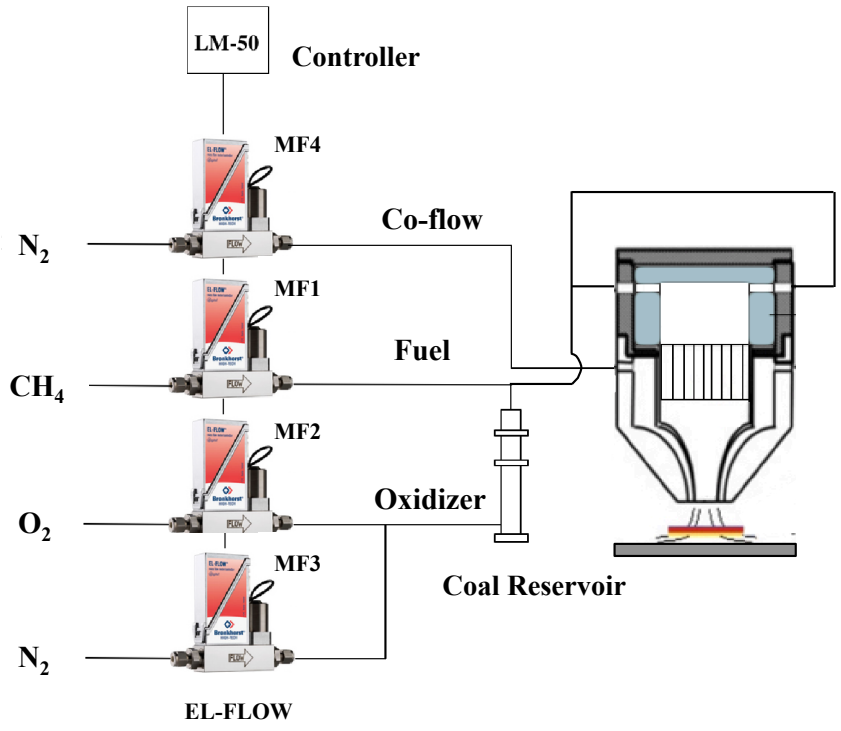

Figure 2.9: *Schematic diagram of the gas flow control system*

Table 2.2: *Description of flow meters*

Flow meter	Max. Flow (L/min)	Calibration gas	Metered gas
MF1	0.8	Methane(CH_4)	Methane(CH_4)
MF2	1.89	Air	Oxygen (O_2)
MF3	15.31	Oxygen (O_2)	Nitrogen (N_2)
MF4	16.67	Nitrogen (N_2)	Nitrogen (N_2)

2.3 Measurement techniques

Measurements on a strained flame of small dimensions require precautions, since the flow is very sensitive to outer perturbations. The non-intrusive optical diagnostics are well adapted for the current experimental configuration, thanks to the easy optical access. Two measurements techniques, flame chemiluminescence and emission spectroscopy, are chosen to obtain information on the flame structure. A schema of the experimental setup and diagnostics is displayed in Fig.2.10.

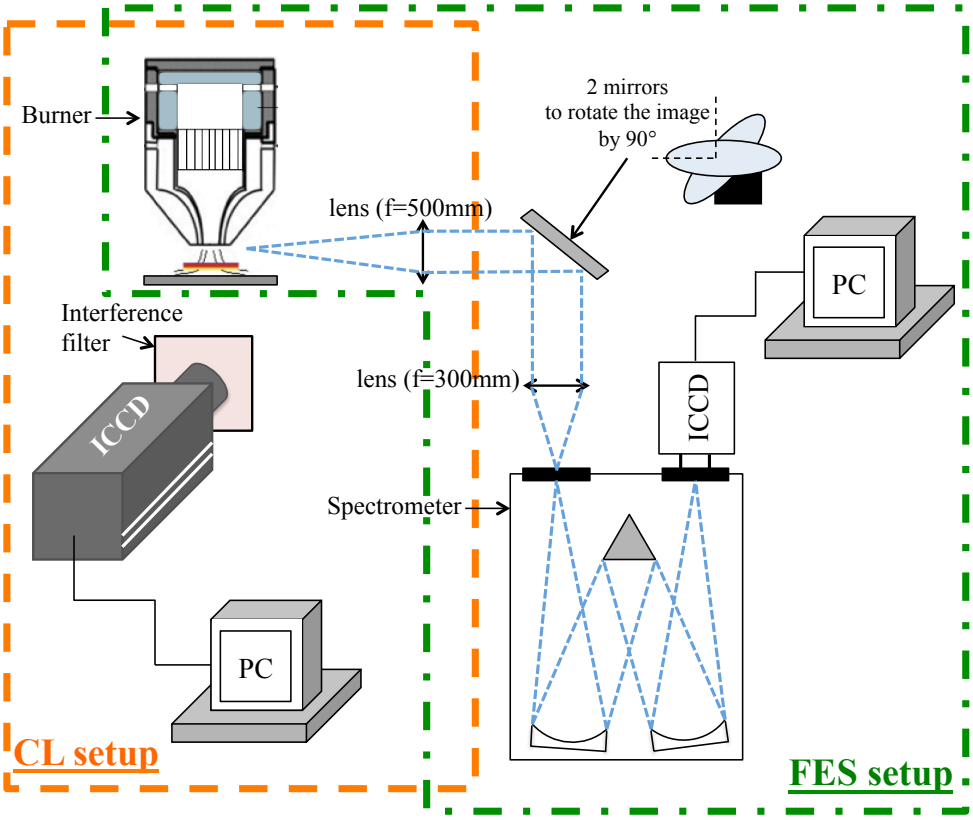

Figure 2.10: *The experimental arrangements of the two optical diagnostic techniques (CL: chemiluminescence, FES: spectroscopy)*

2.3.1 Flame chemiluminescence measurements

Chemiluminescence is defined as the spontaneous emission of electromagnetic radiation due to exicited radicals in chemical reactions. Visualization of flame chemiluminescence is a simple and fast diagnostic. The most common method of visualization involves a CCD camera and spectral filters. The detected species may have visible, ultraviolet or infrared wavelengths. The image re-

sults from integration of filtered light over the spectral band pass of the filter during the camera exposure time. It is also spatially integrated in the direction of the camera. As the flame front is axi-symmetrical, Abel inversion can be used to remove the effects of the integration and get the image of the flame front in the symmetry plane of the burner. Taking into account the very short time interval of each image (from 20000 to 500 frames per minute depending on the signal strength and camera), it can be considered to catch instantaneous information of certain species in the flame zone. If the experimental setup and camera parameters remain the same, it is possible to compare relative quantification of free radicals mole fractions in different operating conditions (Merotto et al. 2017).

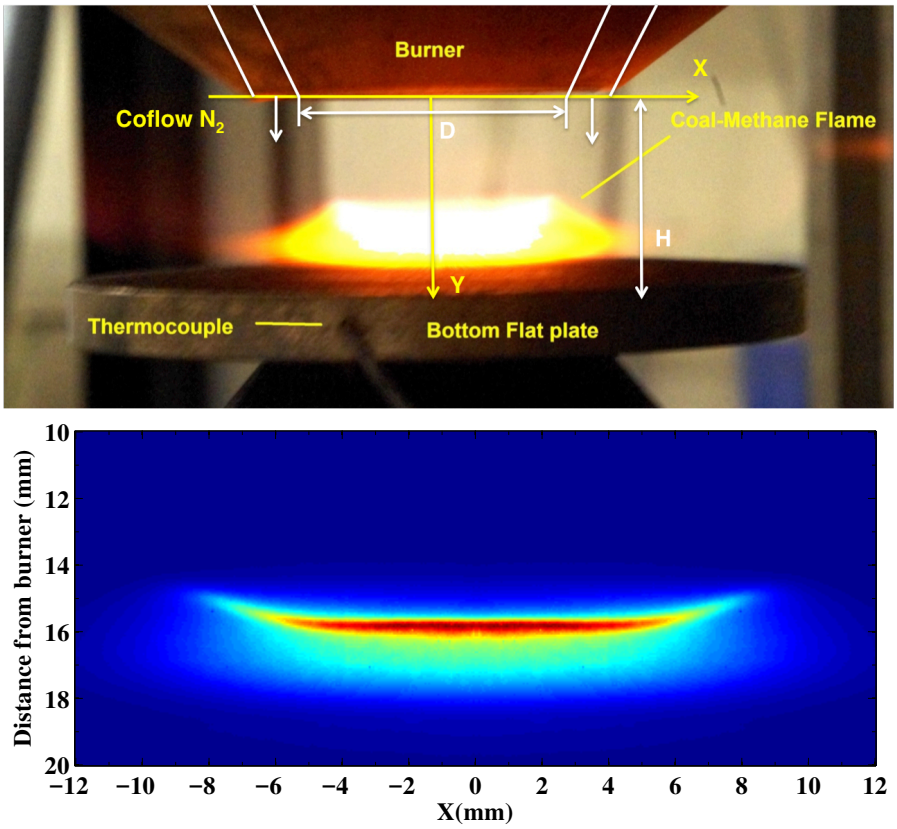

Figure 2.11: *Direct view of methane/air flame fed with coal particles (up), average image of CH* emission of methane/air flame with coal particles(bottom)*

2.3.1.1 Chemiluminescence setup

2-D images of OH^*, CH^* and C_2^* spontaneous emission have been recorded using a 512×512 pixels ICCD camera (Princeton Instruments) equipped with UV lens Nikkor 105 mm focal length f/4.5. Narrow-band interference filters

are interposed along the optical path for capturing the chemiluminescence signals. The OH^* narrow-band filter is centered at 313 nm, 10 nm band-pass and 68% transmission in the maximum. The CH^* filter has 60% transmission and a 10 nm width band-pass centered at 430 nm. The filter for C_2^* band-pass is centered at 515 nm and has 10 nm bandwidth and 80% transmission. Emission profiles are obtained by averaging 300 images, which are corrected by means of dark background subtraction. An averaged CH^* emission image is shown in Fig.2.11. Since the camera captures the overall signal from the flame pattern, Abel inversion of the axisymmetric data field is performed to remove the curvature effect and to obtain the profiles along the central axis.

2.3.2 Flame Emission Spectroscopy (FES)

Transition of a molecule/radical from the excited state to the fundamental state correspond to the emission of a spectral line at a frequency of:

$$\nu = \frac{E_2 - E_1}{h} \tag{2.3}$$

Where E_2 and E_1 are the initial and final energy states, respectively, and h is the Planck constant ($h = 6.62\text{E}^{-34}\ J.s$).
Molecular spectroscopy has played an important part in interpreting spectroscopic observations of flames (Gaydon 1957). The molecules of combustion products which have spectra of appreciable strength in the visible or ultraviolet regions includes hydroxyl radical OH, which gives a band system with the strongest head at 306.4 nm, and intermediate species such as CH, C_2, HCO, CN, NH, NH_2, etc. The primary combustion zone of hydrocarbon flames at atmospheric pressure is characterized by the emission of CH bands strongly at 431.5 nm, which gives the flame the blue color, and the C_2 radicals emitting strongly at 516.5 nm, with a green color. Another fairly strong component is mainly the quasi-continuous emission from excited CO_2. The spectrum CO_2 generally extends from below 300 nm to 600 nm. In this present study, excited radicals naturally present in the combustion zone are chosen, OH, CH, C_2. Indeed, they are widely used to determine important macroscopic properties such as flame location, equivalence ratio and heat release rate fluctuations.

Unlike visualization of flame chemiluminescence via optical filters, Flame Emission Spectroscopy (FES) allows spectral resolution of the emission spectra. Since the CO_2 and blackbody emission plays an important role in coal flame emission, it is necessary to compare the results from FES with that obtained by chemiluminescence.

2.3.2.1 OH spectrum

The existence of the ultraviolet bands of OH molecule in flames is widely used as an indicator of flame behavior (Panoutsos et al. 2009). In hydrocarbon/air flames, OH^* is mainly formed via the following route:

$$CH + O_2 \rightarrow CO + OH^* \tag{2.4}$$

Smith et al. (2005) determined the rate constants for two additional formation paths of OH^*, important mainly in H2/air flames:

$$\begin{aligned} &O + H + M \rightarrow OH^* + M \\ &OH + OH + H \rightarrow OH^* + H_2O \end{aligned} \tag{2.5}$$

Figure 2.12 shows the OH(A) band (head at 306.4 nm) measured in a lean premixed methane/air flame (Flame A1 from table 3.1).

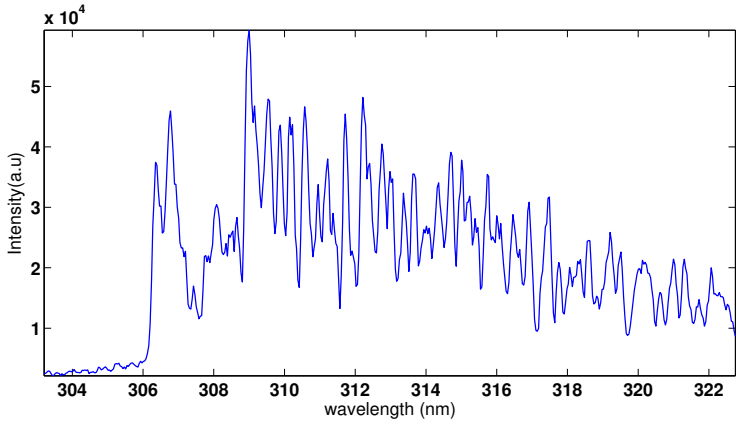

Figure 2.12: *Measured OH spectrum in a lean premixed methane-air flame*

2.3.2.2 CH spectrum

In hydrocarbon/air flames, it is considered that CH^* is mainly formed via following reactions:

$$\begin{aligned} &C_2H + O \rightarrow CO + CH^* \\ &C_2H + O_2 \rightarrow CO_2 + CH^* \\ &C_2 + OH \rightarrow CO + CH^* \end{aligned} \tag{2.6}$$

The strongest CH^* band system is around 431.5 nm (often refered as CH(A)), another weaker one is located around 387.2 nm (refered as CH(B)). Figure 2.13 shows the CH(A) band measured in a lean premixed methane/air flame (Flame A1). In order to compare with spontaneous emission, the CH(A) band is measured in this study.

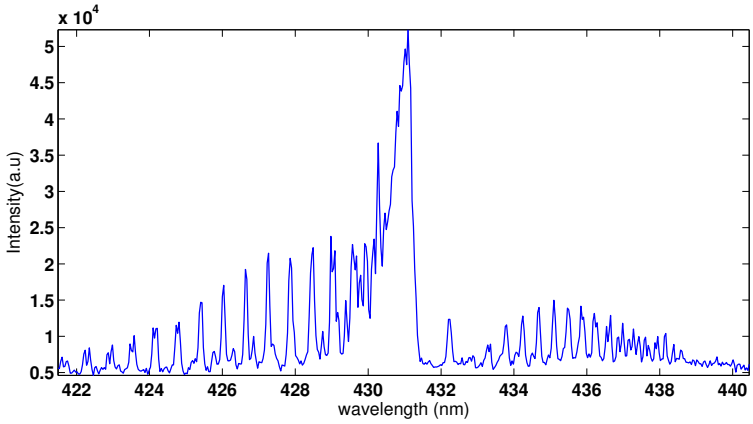

Figure 2.13: *Measured CH spectrum in a lean premixed methane-air flame*

2.3.2.3 C_2 spectrum

C_2 is strongly involved in the formation of OH^* and CH^*. Therefore, Smith et al. (2002) proposed the kinetic paths of C_2.

$$\begin{aligned} &C_2 + H_2 \rightarrow C_2H + H \\ &CH + CH \rightarrow C_2 + H_2 \\ &C + C + M \rightarrow C_2 + M \\ &C + CH \rightarrow C_2 + H \\ &O + C_2 \rightarrow C + CO \\ &C_2 + O_2 \rightarrow CO + CO \end{aligned} \tag{2.7}$$

If no further improvement is considered by adding the kinetics of C_3 and related species (Smith et al. 2005), C_2 can be used as the indicator of the relative intensity of C_2^*. Further discussion of the C_2^* kinetics is given in the next chapter.

Figure 2.14 shows the C_2(d) band measured in a rich premixed methane/air flame (Flame A3 from table 3.1). It is also refered as the San band, where the strongest (0,0) band is at 516.5 nm.

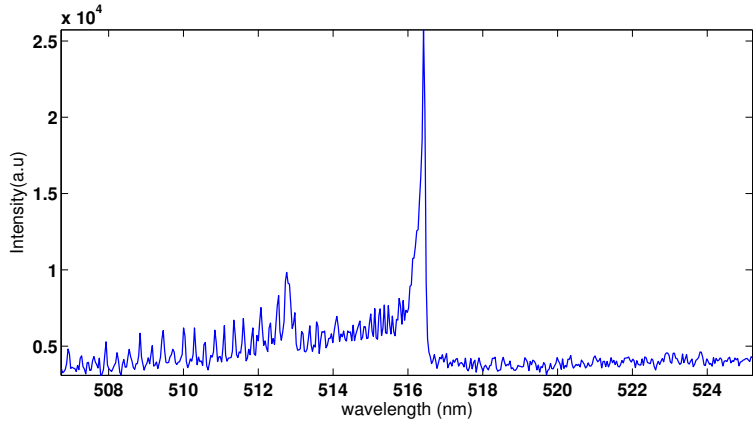

Figure 2.14: *Measured C_2 spectrum in a rich premixed methane-air flame*

2.3.2.4 Trace elements spectra

Besides the molecular spectra of OH, CH and C_2, the spectrum of coal flames presents strong lines of metallic trace elements such as Sodium (Na) at 589 nm, Lithium (Li) at 671 nm and Potassium (K) at 766 and 769 nm. Figure 2.15 presents the typical spectra of a lean premixed methane/air flame with/without addition of coal particles. A low resolution spectrometer (OceanOptics, Maya2000Pro) is used to obtain preliminary information of the flame emission spectra. Results show that the wavelengths of these emission lines do not interfere with the intensity measurement of OH, CH and C_2 emission.

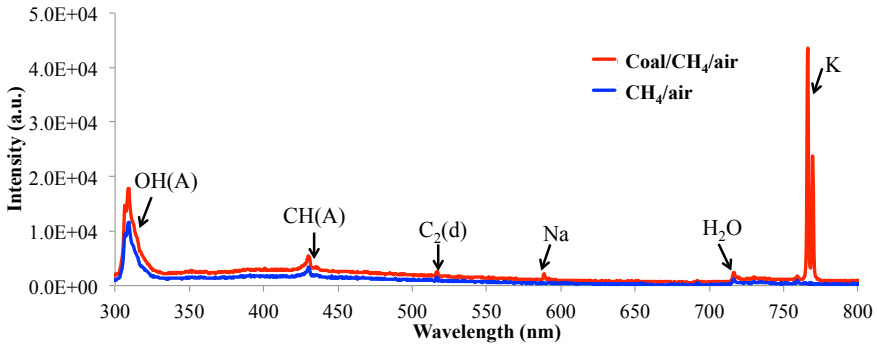

Figure 2.15: *Measured spectra using low-resolution spectrometer*

2.3.2.5 FES setup

FES is used to measure the visible, ultraviolet (UV) chemiluminescence of OH, CH and C_2 radicals. A Czerny-Turner type monochromator (SpectraPro-500i) is used. A 512×512 pixels ICCD camera (Princeton Instruments) is located

at the monochromator output. The diffraction grating is 1200 grating/mm and the focal length of the spherical mirrors is 500 mm. The spectrometer is optically collimated by two plano-convex synthetic fused silica ultraviolet lenses of 500 mm and 300 mm focal length respectively. A slit width of 80 μm is chosen and the exposure time is kept constant to 300 ms. The correction in the detector response is done with a Tungsten lamp and a mercury lamp. As the spectrometer entrance slit is vertical while the flame front is horizontal, two mirrors (Fig. 2.16) are used to rotate the image by 90°to coincident the slit with the flame front. The diagram of the optical system can be found in Fig.2.10. The mechanical positioning system allows the burner to move vertically, thus obtaining the spectra at different locations along the burner axis.

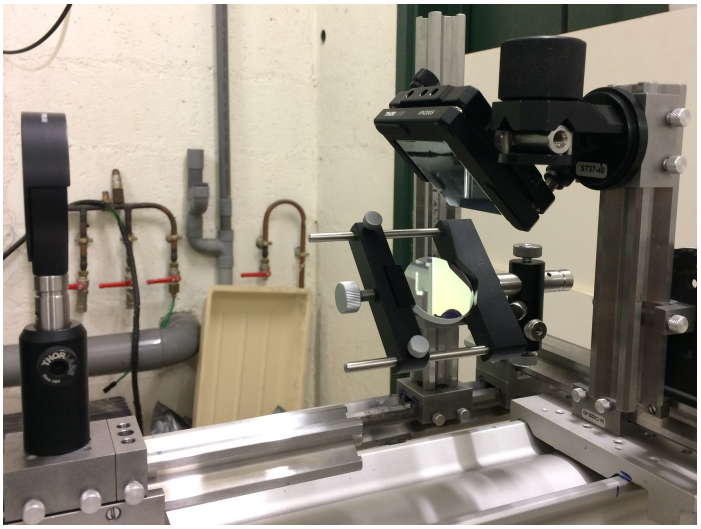

Figure 2.16: *The strained flow burner with the micro-positioning system*

In order to obtain OH^*, CH^* and C_2^* emission profiles, the evolution of the spectrum band heads intensity at 309 nm, 431 nm and 516.5 nm (Gaydon 1957) are obtained along the burner axis respectively. A comparison of the spectra with/without coal particles obtained for OH^* emission of Flame I with/without coal particles is shown in Fig.2.15. We can note that there is a displacement of the baseline of the spectra when coal particles are added to the flame. This is attributed mainly to ambient background as well as the black body emission of solid coal particles and unburned coal char. Post-processing of the raw data then needs to be performed so as to clarify the origin of this difference. This background emission is subtracted from every measured spectrum. The post-processing techniques will be discussed in detail in the next chapter.

Chapter 3

Processing procedure and experimental results

The purpose of this chapter is first to describe the post-processing procedure of experimental data in the present work. The approaches used to process the raw data obtained from spontaneous emission and spectroscopy are presented. The main purpose is to get reliable information on OH^*, CH^* and C_2^* emission intensities. Then all the operating conditions are explained. Finally, typical experimental results of one particular condition obtained from post-processing methods are introduced and thoroughly discussed.

3.1 Processing procedure

3.1.1 ASE data processing

The measurements of spontaneous emission in this study are performed by the acquisition of images. Figure 3.1 presents the spontaneous emission of a CH_4/air flame obtained by the ICCD camera. This image shows that the flame front is not straightly flat but slightly convex. This is essentially due to the natural convective flow around the burner. As a consequence, the signal observed by the camera is modified by the surrounding burnt gases.

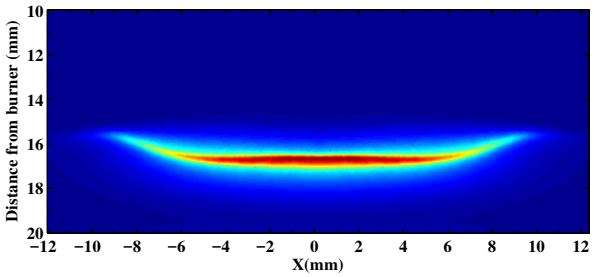

Figure 3.1: *Spontaneous emission of CH_4/air Flame A1 (filterless image)*

Also, these images are the projections of the circular flame zone on to the CCD camera (see Fig.3.2). That is to say, the signal of the three-dimensional flame zone is obtained through the line-of-sight integration. Abel inversion technique is therefore needed to obtain two-dimensional information from the projection.

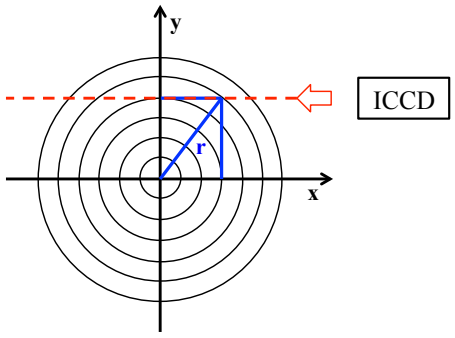

Figure 3.2: *Geometry of the axi-symmetric flame zone and projection on to the camera*

Abel transform is an integral transform often used in the analysis of spherically or axially symmetric functions. In image analysis, This often-called "forward" Abel transform is used to project an optically thin, axially symmetric emission function $\epsilon(r)$ onto a plane in order to get the intensity function $I(y)$ along the

parallel lines of sight.

$$I(y) = 2\int_{y}^{\infty} \frac{\epsilon(r) r dr}{\sqrt{y^2 - r^2}} \tag{3.1}$$

where y is the displacement of the intensity profile and r is the radial distance from the source. That is to say, $I(y)$ is the one-dimensional projection of a two-dimensional, spherically symmetric function $\epsilon(r)$ as a radial slice. Vice versa, the reconstruction of $\epsilon(r)$ from its projection $I(y)$ is known as Abel inversion. It provides a 2-D "cut" of the flame zone at the plan of burner axis. The inverse integral is given by

$$\epsilon(r) = -\frac{1}{\pi}\int_{r}^{\infty} \frac{dI}{dy}\frac{dy}{\sqrt{y^2 - r^2}} \tag{3.2}$$

Abel-inverted spontaneous emission (ASE) profiles of the strained flame will be presented in the next section.

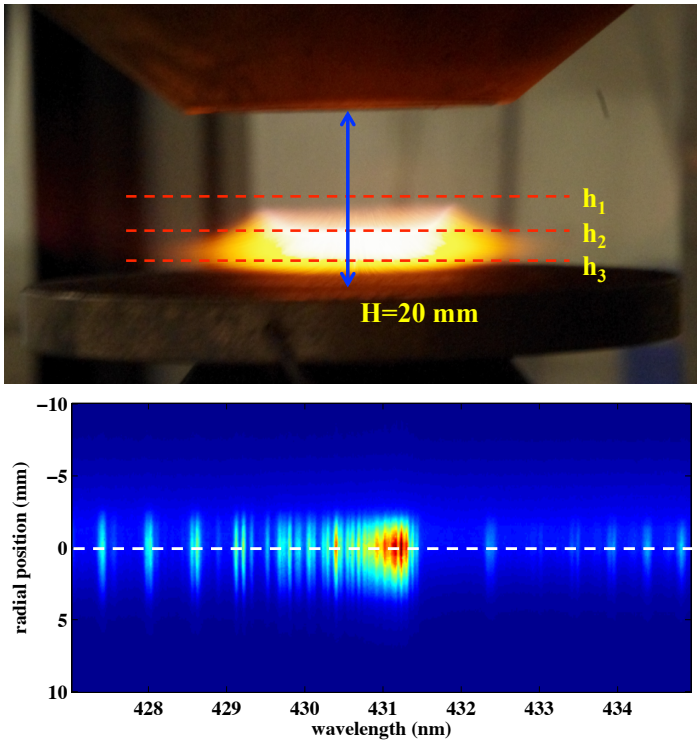

Figure 3.3: *(up):example of spectra asquisition postions; (bottom): an typical image of CH* emission spectrum - radial position (mm) vs Wavelength (nm)*

3.1.2 FES data processing

3.1.2.1 Acquisition of raw data

In the present flame emission spectroscopy (FES) measurments, a mirror system (section 2.3.2.5) is added between the entrance slit of the spectrometer and the flame. The aim of this setup is to rotate the image of the flame by 90° to coincident the slit with the flat flame front. Therefore, the emission profiles along the radial axis (the red pointed line in Fig.3.3(up))is obtained at each time. Measurements are then repeated at certain distances from the burner (h_1, h_2, h_3, etc.). By doing this, the error related to the spatial resolution along the burner axis can be reduced significantly. Also, a 3-mm diameter iris diaphragm is mounted to reduce the interference from the border effect. An image of CH^* emission spectra obtained from Flame A1 with coal particles is shown in Fig.3.3 (bottom) where the colormap corresponds to the emission intensity (a.u.). The average of emission intensity of 1 *mm* at the burner axis is taken to plot the evolution of the spectrum band heads. In this area, the temperature and species mass fractions are considered to be independent of the radius. A typical CH^* spectrum is presented in Fig.3.4 In order to avoid the uncertainties of plotting the evolution of only one pixel, an average of 5 pixels around the band heads was done.

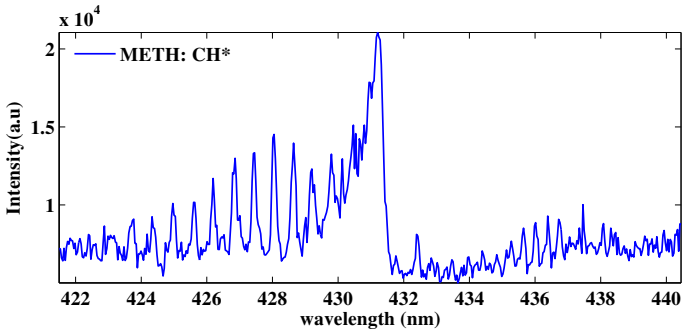

Figure 3.4: *CH^* spectrum obtained at the flame front of CH_4/air flame A1*

The intensity profiles at different distances from the burner are then obtained by moving the burner via the micropositioning system presented in section 2.2.2. Therefore, the optical path and setup is kept constant. A series of spectra corresponding to each axial position is presented in Fig.3.5. It shows clearly that the baseline of each raw spectrum is not necessarily the same. The contribution to this baseline value comes from both background emission (i.e. the ambient environment) and as well as continuous spectra such as CO_2^* and blackbody emission. In order to remove this baseline and to get relative information on OH^*, CH^* and C_2^* emission intensities, subtraction preocedure is necessary to correct the profiles. This will be developped in detail in the next

section.

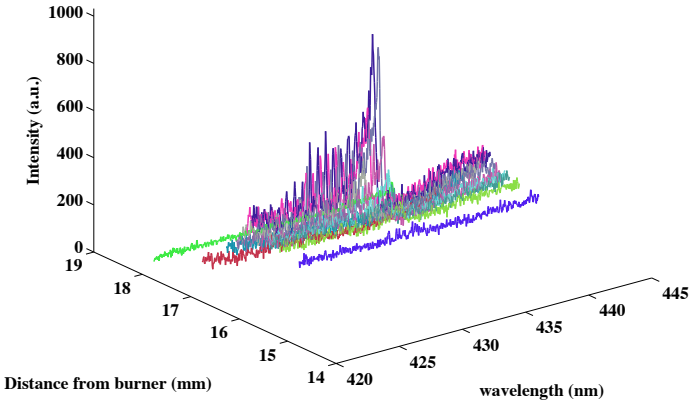

Figure 3.5: *Axial CH* emission profiles of Flame A1 with coal particles, raw spectra*

3.1.2.2 Post-processing procedure

Background signal

The background signal from ambient environment is measured and averaged before and after the measurement of each operating condition. This value may change due to the temperature and other parasite light sources. In Fig.3.6 (left) is presented the comparison of two raw CH* spectra obtained in the flame front for CH_4/Air and Coal/CH_4/Air flames respectively. After removal of the corresponding background signal respectively, the corrected spectra are shown in Fig.3.6(right). This first step removes the "offset" value of each spectrum.

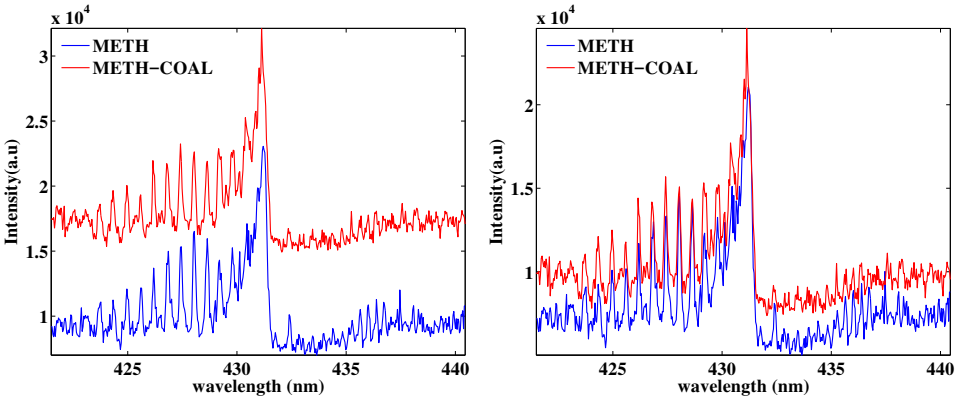

Figure 3.6: *Comparison of raw CH spectra (left) and background-removed spectra (right) obtained in the flame front for CH4/Air (blue) and Coal/CH4/Air (red) flames*

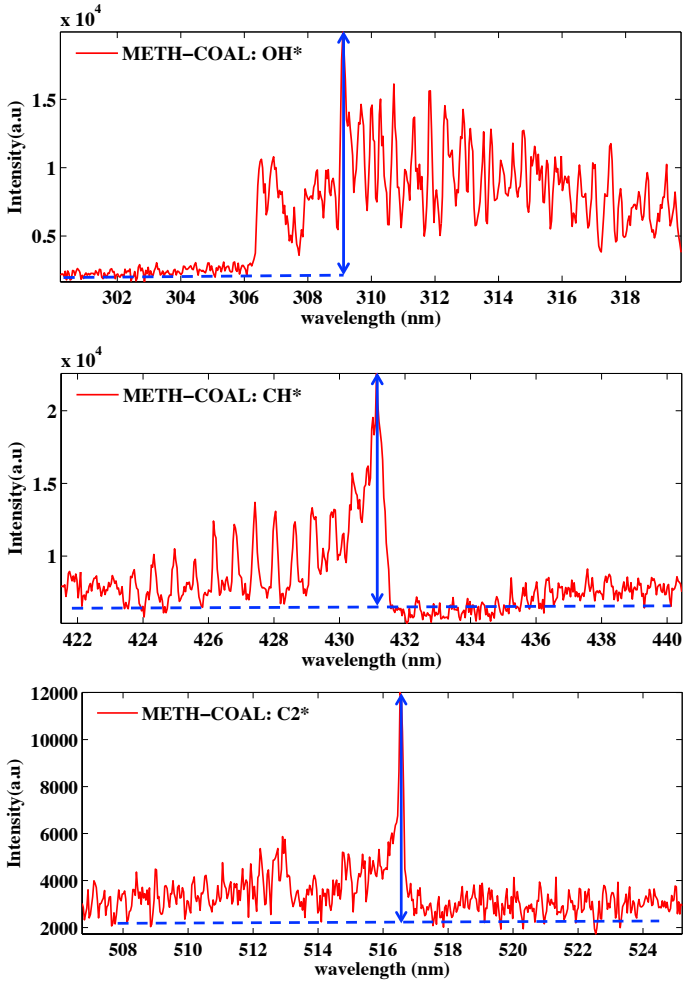

Figure 3.7: *Examples of the continuous spectra correction of OH^*, CH^* and C_2^* emission profiles of Coal/CH_4/air flame A1*

Continuous spectra

$$
\begin{aligned}
I^{bb}_{OH(309nm)} &= I_{301nm} \\
I^{bb}_{CH(431nm)} &= \frac{1}{2}(I_{422nm} + I_{440nm}) \\
I^{bb}_{C_2(516.5nm)} &= \frac{1}{2}(I_{508nm} + I_{525nm})
\end{aligned}
\tag{3.3}
$$

The CO_2^* and blackbody subtraction is performed according to equations (3.3), where the overall signal I^{bb} is estimated. This subtraction is done because both the CO_2^* and blackbody emission have continuous spectrum (Alviso (2013)). Therefore, the I^{bb} of CH^* at 431 nm is obtained by averaging the I^{bb} at 422 nm and 440 nm wavelength, while the I^{bb} of C_2^* from 508 nm and 525 nm wavelength.

These value are chosen from the same spectrum acquired at each measurement. As for OH^* spectrum, I^{bb} at 301 nm is used where no OH^* band is present at this wavelength. Figure 3.7 illustrates the subtraction procedure for OH^*, CH^* and C_2^* emission profiles respectively. An example of these two steps of post-processing is given in the next section. This blackbody signal is relatively smaller for OH^* and CH^* spectrum because the blackbody radiation effect is much more significant with higher wavelength according to the Planck's law. However, for C_2 spectrum, this substraction is essential to clearify the sources of emission intensity.

3.2 Experimental results

3.2.1 Operating conditions

Operating conditions are selected to ensure flame stability, flame thickness for enough spatial resolution and high emission intensity to improve the signal/noise ratio . The main limitation when conducting the experiments is that the flame stability is very sensible to the following three parameters:

- Equivalence ratio Φ of the gas mixture
- Injection velocity V_u (strain rate ϵ)
- Oxygen/Nitrogen ratio

Name	Equivalence ratio Φ	Inlet velocity V_u (m/s)	Strain rate ϵ (s^{-1})
Flame A1	0.88	2.6	260
Flame A2	1.0	2.6	260
Flame A3	1.12	2.6	260
Flame A4	1.2	2.6	260

Table 3.1: *Four different equivalence ratios (Φ) studied*

Name	Φ	V_u (m/s)	ϵ (s^{-1})	O_2 (%)	N_2 (%)
Flame A1	0.88	2.6	260	21	79
Flame B1	0.88	2.7	260	23	77
Flame C1	0.88	2.8	260	25	75

Table 3.2: *Three oxygen inlet volume fractions studied*

So it is necessary to perform parametric studies. In order to identify the importance of each factor, we have performed numerical simulations (Xia et al. (2017)) to study the effect of strain rate on the flame structure and emission

intensity. The results showed that the strain rate would result in the displacement of the flame front position. The increase of residence time of coal particles would produce more pollutants. However the parametric study further discussed in section 7.1 will show that the mole fractions of OH^*, CH^* and C_2^* do not exhibit significant difference with moderate difference of strain rate. To illustrate the type of results obtained, the experimental conditions of four different equivalence ratio (Φ defined by Eq.2.2) with constant strain rate (ϵ defined by Eq.2.1) are fisrt chosen as shown in Table 3.1. Secondly, the oxygen mole fraction in the oxidizer stream has been varied from 21% to 25% for a constant equivalence ratio $\Phi = 0.88$, as shown in Table 3.2.

3.2.2 Spontaneous emission

Figure 3.8(up) presents a typical CH_4/air flame front obtained by CH^* chemiluminescence of Flame A1. The Abel-inverted spontaneous emission (ASE) profile is plotted along with the averaged signal in Fig.3.8(bottom). Because the absolute value is changed after Abel transformation, both profiles are normalized by their repective peak values. It can be noted that Abel inversion has shifted very slightly the location of the maximum CH^* emission intensity. Similarly, the ASE signal of Flame A1 with coal particles is presented in Fig.3.9. The same curvature effect is corrected by Abel inversion.

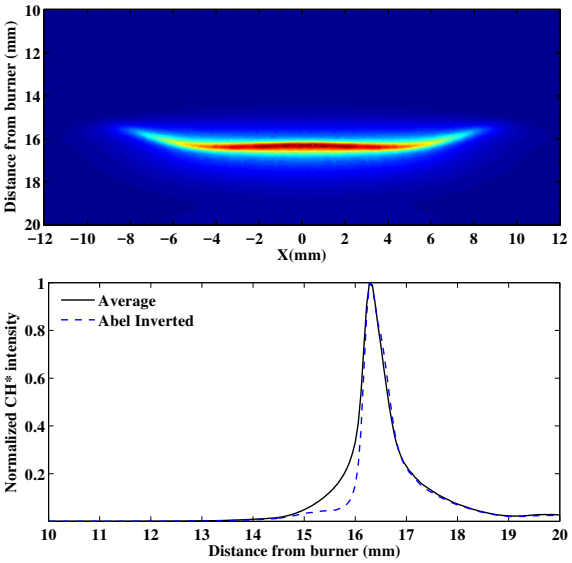

Figure 3.8: *Average image of CH* emission of Flame A1 (up); axial CH* emission profiles of the averaged and Abel inverted data normalized with the peak values (bottom)*

By plotting the two normalized ASE profiles of Flame A1 with and without coal particles in Fig.3.10, one may notice that both CH^* and C_2^* signals appear

in the burnt gases of the CH_4/coal/air flame while they are not observed in the CH_4/air flame. Numerical simulations presented later in this present work will help to analyze this phenomenon.

It's also worth noticing that the C_2^* profile of coal flame does not show clearly the peak which indicates the position of the flame front but a small plateau instead. This can be explained by the fact that the emission intensity around 516 nm in the hot gases is much higher than that of the flame front. However, this emission is the combination of C_2^* radical and the blackbody spectrum. In order to get an idea of the influence from each factor, the results obtained from FES are compared in parallel in the following section.

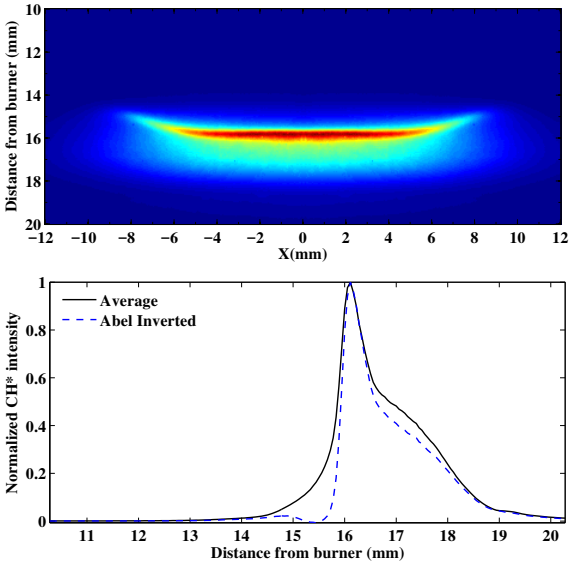

Figure 3.9: *Average image of CH* emission of Flame A1 fed with coal particles (up); axial CH* emission profiles of the averaged and Abel inverted data normalized with the peak values (bottom)*

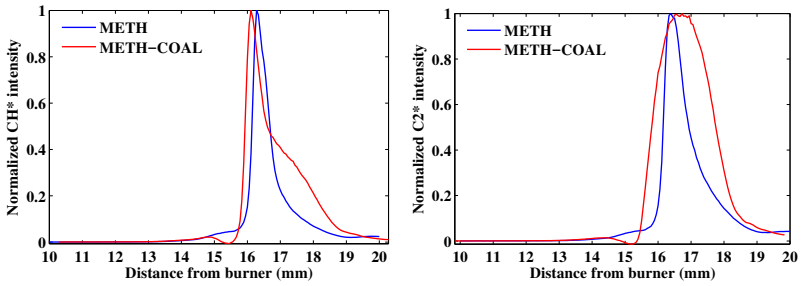

Figure 3.10: *Axial CH* (left) and C_2^* (right) emission profiles of Flame A1 normalized with the peak values (METH: CH_4/air flame, METH-COAL: CH_4/coal/air flame)*

3.2.3 Emission spectroscopy

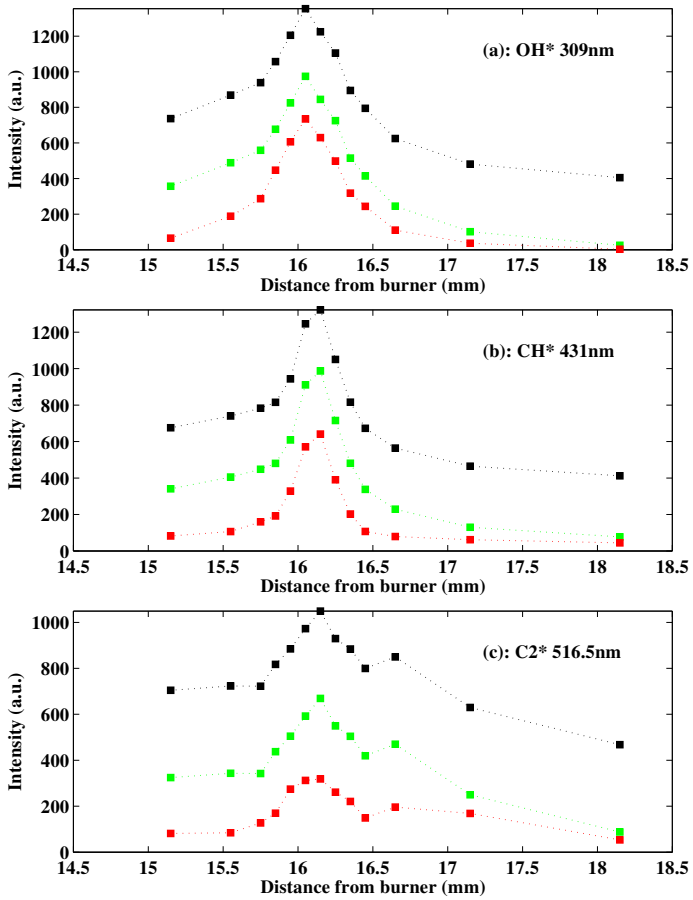

Figure 3.11: *Comparison of emission profiles of original signal(black), signal after ambient background subtraction(green) and final corrected signal after subtraction of blackbody radiation (red) of Coal/CH4/Air flame: (a) OH^*, (b) CH^*, (c) C_2^**

Figure 3.11 shows the comparison of signals before and after post-processing procedure. The first correction (black to green signal) corresponds to the removal of the ambient backgroud. The offset value is practically constant along the burner axis. However, it should be noted that the second subtraction (green to red signal) of continuous spectrum from CO^* emission and blackbody radiation is not consistent along the burner axis. This can be explained by the fact that the flame is not perfectly flat but slightly saucer-shaped (see Figs.3.8 and 3.9). The measurements along the vertical direction in the region above the flame are inevitably affected by the light emissions from the upward-curved tail. This creates an artificial signal, which increases the measured concentration on the fresh gas side.

The uncertainty of the measurement is estimated from maximum emission intensities in 300 images, in comparison to the average values obtained from those images. In CH_4/air flames the uncertainty is 5% and in CH_4/coal/air flames 10%. As the measurements do not give absolute values, in order to make comparisons with the numerical results, the experimental profiles of OH^*, CH^* and C_2^* were normalized by the maximum values from the reference CH_4/air Flame A1.

3.2.4 Comparison between ASE and FES

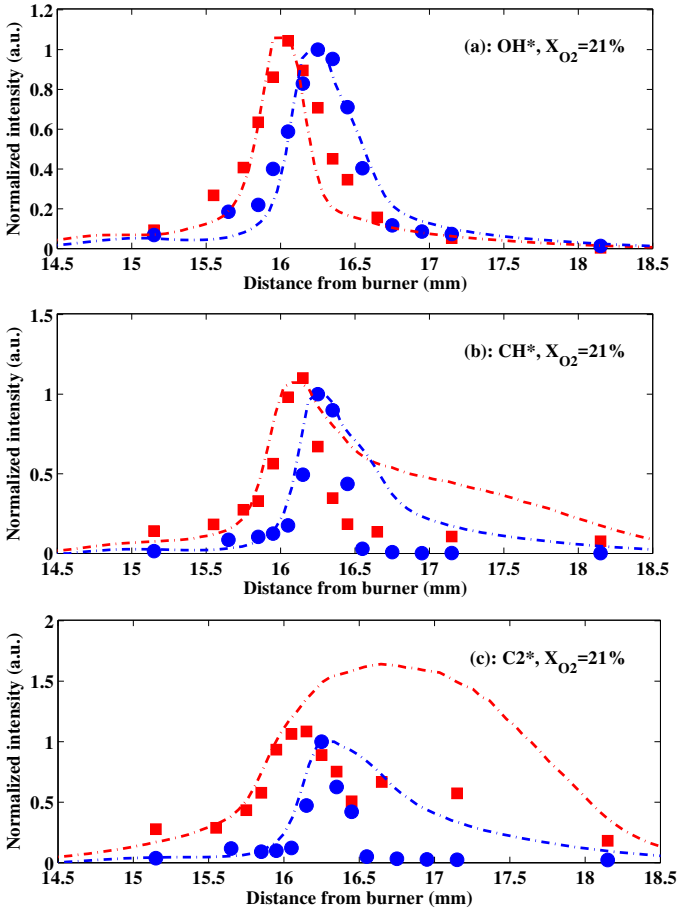

Figure 3.12: *Comparison of OH^* spontaneous emission imaging (dashdot line) and spectroscopy (circle and square) profiles for $CH_4/O_2/N_2$ (blue) and $Coal/CH_4/O_2/N_2$ (red) flames for different O_2 mole fractions: (a) OH^*, (b) CH^*, (c) C_2^**

Here we compare the signals from ASE and FES measurements of Flame A1. Figure 3.12 illustrates the comparisons of OH^*, CH^* and C_2^* emissions of both CH_4/air and CH_4/coal/air flames respectively. The experimental setup and

parameters are kept constant, so that the intensity profiles can be considered relatively comparable with each other. All profiles are normalized by the maxima of OH^*, CH^* and C_2^* emission corresponding to CH_4/air Flame A1 (without coal particles) from ASE and FES signals respectively. The comparison shows that results from ASE and FES are coherent at the fresh gas side. However in the burnt gases OH^* profiles from both methods are consistent but CH^* and C_2^* signals significantly differ. It seems that in this region the ASE signal is more important due to blackbody emission because it can not be eliminated from the measurement, while FES signal is corrected for blackbody emission.

The comparison between ASE and FES signals highlights the advantages and disadvantages both methods. The spontaneous emission imaging using narrowband filters is spatially resolved and relatively les time-consuming than FES method. However, spectrally resolved FES permits blackbody emission correction, which has significant effect especially for the presence of coal particles.

Part II

Numerical studies of pulverized coal devolatilization and oxidation

Chapter 4

Literature review of pulverized coal devolatilization and oxidation: modeling

This chapter addresses one of the most important aspects to simulate coal combustion: the thermal conversion of coal particles. First the characterization of coal, the kinetics of devolatilization, volatile combustion and char combustion are reviewed. Different levels of modeling complexity are summarized. Then, the coupling of these kinetic models with CFD is discussed, in particular, several examples are presented in order to illustrate the gap between detailed models and the need of simplified approaches in CFD applications.

4.1 Characterization of coal

Unlike other fossil fuels such as natural gas or diesel, coal varies considerably in nature. Analysis of the chemical composition of coal and some of its properties is given in this section.

4.1.1 Proximate analysis

The proximate analysis of coal gives an overview of its general composition, based on the different levels of volatile matter, fixed carbon, moisture and ash. These quantities are determined by measuring the mass loss of a coal sample that undergoes the thermo-gravimetric analysis (TGA). The sample is usually heated to up to 900°C under a nitrogen atmosphere and then held at 900 °C and the atmosphere is switched to air (Speight 2005).

4.1.1.1 Moisture

The moisture content can be determined by the mass loss after the sample has been heated to 110°C under a N_2 atmosphere until a constant mass is achieved (Donahue and Rais 2009). The measured moisture content represents water that may be physically or chemically bound in the coal. The percent of water changes with the rank of the coal. Lignite has the most quantity of moisture, while anthracite has the least.

4.1.1.2 Volatile Matter (VM)

Volatile matter is determined by the loss of mass, corrected for moisture, when heating up a coal sample to 900°C in an oxygen-free environment as a result of thermal decomposition. Volatile matter consists of a mixture of gases and tar. The main constituents are CO_2, CO, H_2O, methane and other hydrocarbons (C_xH_y). Determination of the devolatilization rate plays a fundamental role in modeling coal combustion. Anthracite coal has the lowest volatile matter content (typically 2-12%), while bituminous, sub-bituminous, and lignite coals yield higher results, 15-45%, 28-45%, and 24-32%, respectively (Speight 2005). The amount of volatile matter released is also strongly dependent on experimental conditions and heating rates.

4.1.1.3 Fixed Carbon (FC)

Fixed carbon is the solid combustible material (coke/char) that remains after loss of moisture and volatile matter minus the ash that remains after combustion is complete. Combustion occurs when the sample is held at 900 °C and the

atmosphere is switched to air. Fixed carbon is the calculated weight percentage of material that was lost during the testing for moisture, volatile matter, and ash:

$$FC\% = 1 - Moisture\% - VM\% - Ash\%$$

The higher the fixed carbon levels in a coal type the higher the coal rank, highest for anthracite, and lowest for lignite (Speight 2005).

4.1.1.4 Ash

Ash is the residue remained after the coal sample has fully combusted at 900 °C in air. The ash in coal consists of hydrated alumina silicates, iron pyrites, calcium and magnesium carbonates and alkali chlorides (Speight 2005). Neither ash or moisture in a coal are combustible materials, thus the coal rank diminishes with their higher contents.

4.1.2 Ultimate analysis

The ultimate analysis, which is more comprehensive than proximate analysis, is dependent on quantitative analysis of various elements present in a coal sample. It describes the amount of carbon, hydrogen, oxygen, sulfur and nitrogen atoms found in a coal type. The element composition is usually reported on a dry ash free basis (daf). Table 4.1 shows the analysis of three lignite coals: Heizprofi (HP) lignite used in this work, South Beulah (SB) and Morwell (MW) identified in Hara et al. (2015).

Coal Name	Proximate analysis (wt %)				Ultimate analysis (wt %)				
	Moisture	Ash	Volatile matter	Fixed carbon	C	H	O	N	S
HP	19.0	4.3	50.6	45.1	69.0	5.0	24.7	0.8	0.5
SB	18.1	13.7	38.6	47.7	71.8	4.7	19.2	1.4	2.9
MW	19.6	2.0	51.5	46.5	67.4	5.0	26.8	0.5	0.3

Table 4.1: *Ultimate analysis of three lignite coals*

4.1.3 Coal properties

4.1.3.1 Particle morphology

The size and shape of coal particles influence their heat and mass transfer characteristics and behavior in fluids (Mathews et al. 2007; Schiemann et al. 2014; Liu et al. 2015; Bai et al. 2017). Despite the knowledge that coal particles typically are not spherical (Fig.4.1), the size and shape can be determined by microscopy, or light scattering. The assumption of spherical particles is

commonly applied in modeling. In this work, we consider all particles to be spherical during the combustion process.

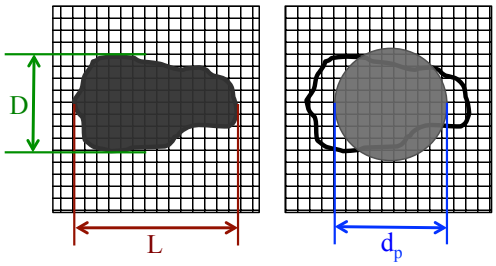

Figure 4.1: *Example of particle size detected by optical measurements (left) and the standard modeling assuptions (right), adapted from Schiemann et al. (2014)*

4.1.3.1.1 Density Coal particles are very porous. The apparent density $\rho_{p,A}$ measured by experiments is usually considered more representative of the coal density than the true density $\rho_{p,T}$, the weight per unit volume of a pore free particle. The porosity θ_p of the particle can be obtained from the ratio of the apparent and true densites.

$$\theta_p = 1 - \frac{\rho_{p,A}}{\rho_{p,T}} \tag{4.1}$$

From this point on, the coal particle density ρ_p in this work will be referred to its apparent density $\rho_{p,A}$, provided by the manufacturer. The density of a coal particle varies during the combustion process due to devolatilization and char combustion.

4.1.3.2 Specific heat capacity

Developing a relationship between the specific heat capacity of coal $C_{p,coal}$ and temperature is very difficult as during thermal decomposition, because the composition of the volatile matter and char within the coal particle changes continuously (Merrick 1983). In most modeling cases, it is assumed that the specific heat capacity of coal remains constant with values ranging between 1100 - 1600 J/kgK (Backreedy et al. 2006b; Franchetti et al. 2016). Some studies attempted to develop models that relate the specific heat capacity of coal to temperature, based on experimental data or from fundamental atomic theory (Merrick 1983; Zhao and Haworth 2014; Rieth et al. 2016; Messig et al. 2017). For a coal particle with a composition ($Y_{volatile}$, Y_{ash}, Y_{char}), $C_{p,p}$ is defined as

$$C_{p,p} = Y_{volatile} C_{p,vol}(T_p) + Y_{ash} C_{p,ash} + Y_{char} C_{p,char}(T_p) \tag{4.2}$$

where $C_{p,vol}$, $C_{p,ash}$ and $C_{p,char}$ are the specific heats for volatile matter, ash and char, respectively. The specific heats of volatile matter and char typically

depend on temperature T_p. Another formulation is based only on T_p, used by Wan et al. (2017)

$$C_{p,p} = 836.0 + 1.53 \times (T_p - 273.0) - 5.4 \times 10^{-4}(T_p - 273.0)^2 \tag{4.3}$$

In this work, $C_{p,p}$ is considered constant and equals to of 1500 J/kgK.

4.2 Modeling of coal combustion kinetics

There are four commonly-recognized steps involved in the conversion process of pulverized coal combustion: evaporation/drying, devolatilization, volatile combustion (homogeneous reactions) and char oxidation/gasification (heterogeneous reactions). Once coal particles are injected into a combustion chamber, they are heated up and the drying process (the release of moisture) occurs immediately, followed by the rapid devolatilization process (the release of volatiles) which occurs due to higher temperatures. Char produced through the volatilization process is consumed by heterogeneous processes of combustion and gasification, and its combustion yields CO_2 and/or CO. Figure 4.2 schematically explains briefly the conversion process of coal particles.

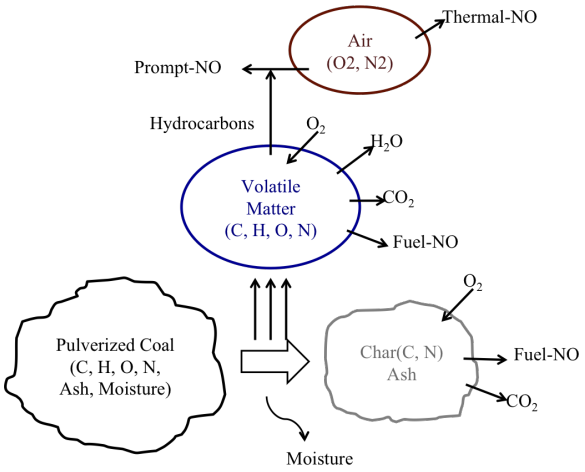

Figure 4.2: *Schematic of coal conversion process*

In the present work, the coal particles used are considered to be dry, ash-free (daf). Therefore, the process is simplified to two major steps concerning the particle phase: devolatilization and char oxidation, as shown in Fig.4.3. The different models are presented in following sections.

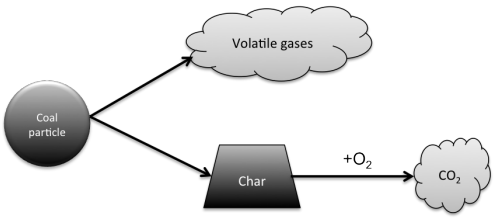

Figure 4.3: *Illustration of the typical coal conversion model used in the present work*

4.2.1 Devolatilization

The first step (neglecting drying) of coal conversion is the thermal decomposition of the large molecular structure during pyrolysis. When a pulverized coal particle enters the furnace, it heats up very rapidly, typically at 10^5 to 10^6 K/s (Lemaire et al. 2014). As the particle heats up the volatile material starts to decompose into a mixture of light gases and tars which are released. This process is known as devolatilization. The composition of the emitted volatile species varies with coal type and heating conditions. The devolatilization process and the combustion of the volatile gases drive the temperature to increase at the early stages of PCC.

Several quantities are expected to be predicted by the devolatilization model, including: the release rate of the volatiles, the yield and composition of the volatiles, and char formation rate.

A variety of coal pyrolysis models have been developed since the 1970s. These models differ considerably in their complexity. The models are classified into two major categories, empirical and network-based models. The network models take into account the detailed coal structure and directly simulate the development of this structure. But empirical models are more often used in CFD due to their lower computational cost.

4.2.1.1 Empirical models

- **Single First Order reaction Model (SFOM)**
  The single rate model Badzioch and Hawksley (1970) assumes that the rate of devolatilization is first-order dependent on the amount of volatiles remaining in the particle.
  The pyrolysis kinetics are modeled following the Arrhenius' Law:

$$\begin{aligned} \frac{dm_{vol}}{dt} &= k\left(m^*_{vol,0} - m_{vol}\right) \\ k &= A_{pyr} exp(-E_{pyr}/RT_p) \\ m^*_{vol,0} &= Q m_{vol,0} \end{aligned} \tag{4.4}$$

where $m_{vol,0}$ is the initial amount of volatile predicted from the proximate analysis. It has been shown by experiments that the amount of volatile released by different heating rates could lead to smaller or greater release than what is given by the proximate analysis, and this is quantified by a factor Q. k is the kinetic rate defined by an Arrhenius type equation with pre-exponential factor A, activation energy E and particle temperature T_p. A and E depend on the intrinsic characteristics of the coal samples and on the heating rate as well.

- **Competing Two Step Model (C2SM)**
  Devolatilization rate described in this model has two weighted first order Arrhenius reaction rates Kobayashi et al. (1977); Ubhayakar et al. (1977). Coal is assumed to decompose via two possible reaction paths depending on its time-temperature history.

$$\begin{aligned} Coal &\rightarrow \alpha_1\, Volatiles + (1-\alpha_1)\, Char, \qquad with\, k_{pyr,1} = A_1 exp(-E_1/RT_p) \\ &\rightarrow \alpha_2\, Volatiles + (1-\alpha_2)\, Char, \qquad with\, k_{pyr,2} = A_2 exp(-E_2/RT_p) \end{aligned} \tag{4.5}$$

And the mass loss rate is expressed as:

$$\begin{aligned} \frac{dm_{vol}}{dt} &= k\left(m^*_{vol,0} - m_{vol}\right) \\ k &= \alpha_1 A_1 exp(-E_1/RT_p) + \alpha_2 A_2 exp(-E_2/RT_p) \end{aligned} \tag{4.6}$$

Both reactions occur at the same time, however the first pseudo reaction is dominant at lower temperatures and the second pseudo reaction becomes increasingly faster at higher temperatures. The competing reaction rate model should be more accurate than the single-step model as the volatile release is a function of the particle temperature history rather than the current particle temperature. However, the model requires knowledge of more kinetic parameters which are often not available or difficult to obtain.

- **Distributed Activation Energy Model (DAEM)**
  The distributed activation energy model assumes that the release of volatiles consists of multiple independent first-order reactions Anthony et al. (1975).

$$Coal \rightarrow \alpha_i\, Volatiles + (1-\alpha_i)\, Char \tag{4.7}$$

The pyrolysis rate of the reaction i is given by:

$$\frac{dm_{vol,i}}{dt} = k_i\left(m^0_{vol,i} - m_{vol,i}\right) \tag{4.8}$$

The activation energy is a gaussian distribution

$$f(E) = \frac{1}{\sigma\sqrt{2\pi}} \exp(-\frac{(E-E_0)^2}{2\sigma^2}) \tag{4.9}$$

with

$$\int_0^\infty f(E)dE = 1 \tag{4.10}$$

And the mass loss rate is expressed as:

$$m = m_{inf}(1 - \frac{1}{\sigma\sqrt{2\pi}}\int_0^\infty \exp(-k_0\int_0^t \exp(\frac{-E}{RT_p})dt - \frac{(E-E_0)^2}{2\sigma^2})dE) \tag{4.11}$$

- **Models for variation of particle size**
  In practice, the particle size might be affected by a number of different processes like swelling, pyrolysis, break-up, char combustion, etc. Therefore coal particle shape and size distribution must be assumed for the calculation. Different approaches can be found in the literature.
  (1) Some use constant-diameter spherical particles corresponding to the measured mass-based median diameter.

$$m_p = \frac{1}{6}\rho_p\pi d_p^3 \tag{4.12}$$

  (2) Some use a swelling model, which allowes the particle diameter to increase by a swelling constant C_{sw} during pyrolysis.

$$d_p/d_{p,0} = 1 + (C_{sw}-1)\frac{m_{p,0}-m_p}{\nu_{vol}m_{p,0}} \tag{4.13}$$

  where $\nu_{vol}m_{p,0}$ is the total volatile content of the particle. However, the swelling effect has been found to be more influential on larger particles, while it does not change the small-particle statistics significantly.

4.2.1.2 Network models

This approach involves approximating the break-up of the coal macromolecular structure during pyrolysis. It requires large amounts of input data about the structure of the coal considered. The Functional-Group, Depolymerization, Vaporization, Cross-linking (FG-DVC) modelSolomon et al. (1988), the FLASHCHAIN modelNiksa and Kerstein (1991), and the chemical percolation devolatilization (CPD) modelGrant et al. (1989) are most widely used. They are more accurate models to predict the production rates of the species during the devolatilization based on the physical and chemical transformations of the coal structure. However, these approaches are usually too expensive to be used directly in CFD applications.

4.2.2 Volatile composition

Volatile gases are made up of light gases (CO, CO_2, H_2, H_2O, CH_4, C_2H_2, C_2H_4, ...) and heavy gases such as tar. The composition of these gases significantly differs depending on the type of coal and the pyrolysis temperature Hara et al. (2015); Xu and Tomita (1987a); Xu and Tomita (1987b). They can either be approximated to a single or a few hydrocarbon species, or obtained experimentally, depending on the desired accuracy. However, modeling the release and transport of each species individually would be expensive in LES, and as such in many studies, the volatiles are treated as a single postulate substance $C_aH_bO_c$ Hara et al. (2015); Hashimoto et al. (2012); Hashimoto et al. (2012), in which a, b and c represent the composition ratio of each chemical element.

The volatile combustion reactions are then expressed by the following formulas.

$$C_aH_bO_c + (\frac{a}{2} + \frac{b}{4} - \frac{c}{2})O_2 \rightarrow aCO + \frac{b}{2}H_2O \tag{4.14}$$

$$CO + \frac{1}{2}O_2 \rightarrow CO_2 \tag{4.15}$$

A more comprehensive representation of the volatile gases is to subdivide them into different species. This approach needs a priori knowledge of the composition of the volatile gases. This knowledge can be provided by the CPD model. Hara et al. Hara et al. (2015) chose CH_4, CO, CO_2, H_2, H_2O, C_2H_2, C_2H_4, C_2H_6, C_3H_6, C_3H_8 as light gas species and C_6H_6 to represent tar.

4.2.3 Char combustion

Reactions of the remaining char with O_2, CO_2 and H_2O take place at the particle surface of the porous char particle. Char kinetics strongly vary from individual samples and under different operating conditions. But they may also depend on the preceding devolatilization process, as the initial char structure and morphology as well as the initial reactivity are determined. Unlike pyrolysis, it is often difficult to obtain reliable char kinetics only from coal analysis information.

- **Diffusion-kinetic model**
  This model includes the effects of both diffusion K_d and chemical reaction rate K_c (Baum and Street 1971). K_d and K_c are the incorporates the effects of chemical reaction on the internal surface of the char particle and pore diffusion respectively.

$$\frac{dm_{p,char}}{dt} = \pi d_p^2 P_O \frac{K_c K_d}{K_c + K_d} \tag{4.16}$$

$$K_d = C_1 \frac{\left((T_\infty + T_p)/2\right)^{0.75}}{d_p} \tag{4.17}$$

$$K_c = A_c exp(-E_c/RT_p) \tag{4.18}$$

Where d_p is the particle diameter, P_O is the partial pressure of oxidant species in the gas surrounding the combusting particle and the kinetic rate.

- **Intrinsic model**
  An alternative is to obtain K_c using the physical properties of the char rather than experimental values (Smith 1978; Smith 1982). The chemical rate K_c is expressed in terms of the intrinsic chemical and pore diffusion rates:

$$K_c = \eta\gamma\rho_p A_{is} k_i \tag{4.19}$$

  where k_i is the intrinsic reactivity of Arrhenius form, $\gamma = d_p/6$ is the characteristic size, A_{is} is the internal surface area of the char particle, and η is the effectiveness factor which is the ratio of the actual combustion rate to the rate attainable if no pore diffusion resistance existed.

- **Carbon Burnout Kinetics (CBK) model**
  CBK (Hurt et al. 1998; Hurt and Calo 2001; Backreedy et al. 2006a; Liu and Niksa 2004) is a variation of the intrinsic model and it was specifically designed to predict the total extent of carbon burnout and fly ash carbon content of PCC. This model takes into account both oxidation and gasification reactions and also includes submodels for the pore evolution, thermal annealing, ash inhibition, etc (Zhou et al. 2017).

4.3 Coal kinetics in CFD

4.3.1 Approaches to bridge the gaps

As introduced in the Section 4.2, a number of various coal models have been developed at different complexity levels over the years. Generally, the network models tend to predict coal conversion rate and products more accurately. However, empirical models are most often used in CFD. In the literature, detailed models are used to calibrate the parameters of the empirical models, which help to achieve better results in large-scale computations.

- **Tabulated-devolatilisation-process (TDP) model**
  The main limitation of using the single rate model is that the same kinetic

parameters are used for all coal particles at all temperatures. However, the volatile yield depends on the particle temperature history and heating rate. Hashimoto et al. (2012) proposed a Tabulated Devolatilisation Process (TDP) model, which consists of a pre-processed table with different values of the kinetic parameters $A(T_p)$ and $E(T_p)$, and Q-factor for a set of particle temperature histories. During the simulation the appropriate parameters are then allocated to each particle given its temperature history. Calculation flowcharts for the conventional and the TDP models are given in Fig.4.4.

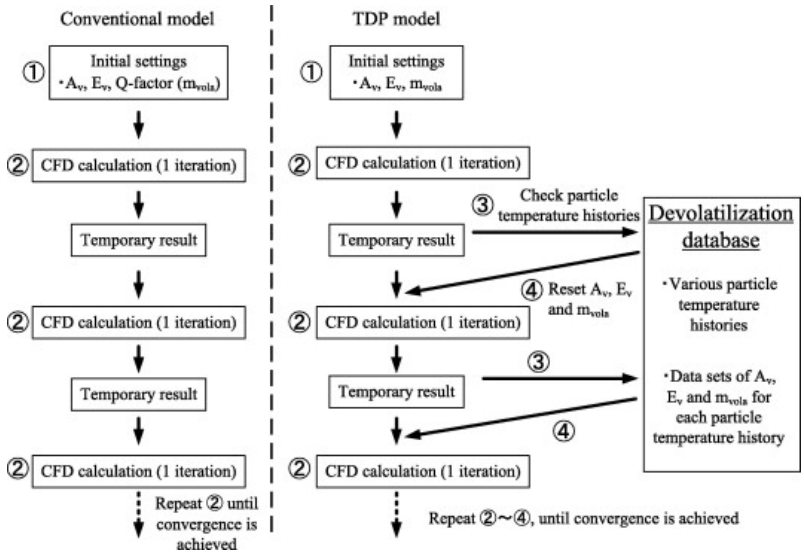

Figure 4.4: *Calculation flowcharts for the conventional and the TDP models from Hashimoto et al. (2012)*

- **Calibration of empirical pyrolysis models**
  Several recent PCC-LES studies used the approach of calibrating the conventional SFOM model with CPD model (Franchetti et al. 2013; Rabacal et al. 2015; Stein et al. 2013; Vascellari et al. 2013; Vascellari et al. 2014), where the CPD model was coupled with the LES solver in by a preprocessing method (Fig4.5). The suggested calibration procedure is reported to give good results comparing with experimental data.

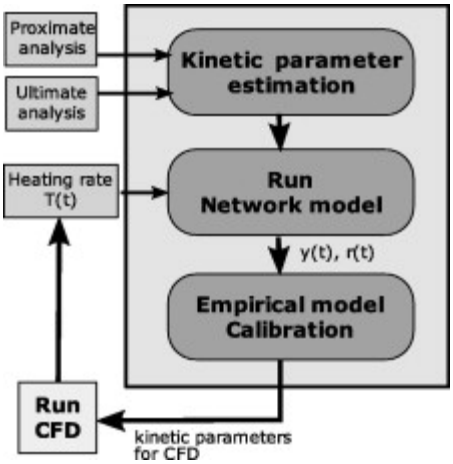

Figure 4.5: *Pyrolysis kinetic preprocessor (PKP) workflow from Vascellari et al. (2013)*

- **Online-CPD-coupled LES**

  In the recent study of Wan et al. (2017), the CPD model, is incorporated into LES in real time (Fig.4.6). The comparison between the CPD-coupled LES and the LES using the SFOM model showed that the CPD-coupled LES approach is able to give a better prediction on particle pyrolysis in the high-temperature turbulent flow.

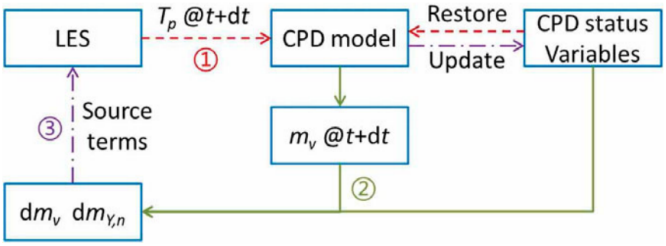

Figure 4.6: *Coupling the CPD model into an LES solver from Wan et al. (2017)*

- **Direct-CPD-flamelet LES**
  Recently, Rieth et al. Rieth et al. (2017) performed direct-CPD-flamelet LES of the CRIEPI jet flame Hwang et al. (2005), where the devolatilization rates are directly determined from CPD model. It is shown that the direct use of CPD in the LES is feasible. Comparison with two empirical models, SFOM and C2SM, showed the influence of devolatilization modeling on the LES results. The difference between CPD and the fitted SFOM model on the instantaneous particle level is significant, so that

the direct CPD coupling may suit better the cases where polydisperse particles experience different thermal histories.

4.4 Summary

To summarize this chapter, detailed coal conversion models are available. However the use of these models in the modeling of practical PCC applications remains limited. Simplified but relatively accurate models are highly required. The current approaches mainly consist of combination between detailed modeling and laboratory-scale experiments for the calibration of simplified models. On the other hand, the commonly used coal sub-models have never been tested and validated in strained laminar configurations. Therefore, parametric studies and analyses of the assumptions that are commonly used in PCC simulations will be studied in the present work.

Chapter 5

Modeling of pulverized coal devolatilization and oxidation in strained $CH_4/O_2/N_2$ flames

This chapter presents the governing equations describing pulverized coal devolatilization and oxidation in strained methane/nitrogen/oxygen flames. First, the governing equations that describe the gaseous phase are presented. The equations will be limited to the 1-D formulation used in this thesis, with the addition of a source term to account for the two-phase coupling between the gas and solid phase. Then an overview of the models used in this work to represent the solid phase and the governing equations are reported. Finally the numerical methods used in this work to discretize the equations in space and time are given.

5.1 The structure of strained premixed laminar flames

Strained premixed laminar flames offer the advantage of well defined flame conditions suitable for experimental investigations and also for numerical studies of the combustion processes (Darabiha et al. 1993). The laminar premixed flat flame archetype retained consists of a burner ejecting fresh gases against a wall (Fig.5.1). The premixed fuel and oxidizer flow with a velocity dependent on the mixture composition. Strain rate ϵ, calculated according to Eq.2.2, increases by increasing the mixture injection velocity. ϵ is thus controlled by modifying the injection velocity V_u. The mixture of fuel and oxidizer impacts onto the stagnation plane, which is here the wall surface. The flame is stabilized when the flow velocity equals the flame speed, thus defining the flame front position.

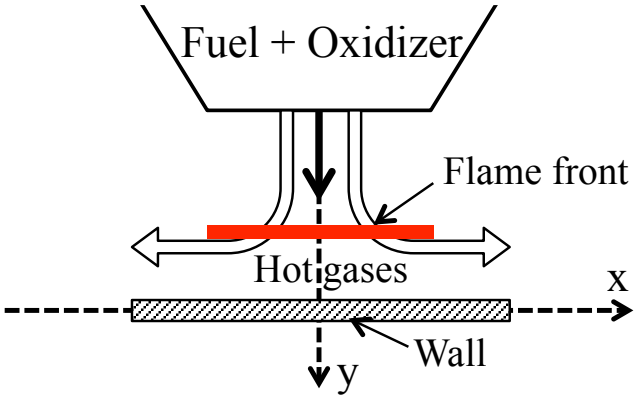

Figure 5.1: *Schematic presentation of a laminar premixed flat flame impinging a wall*

The modeling of laminar strained flames has been well studied in EM2C laboratory for decades. Rolon (1988) studied in detail the structure of a laminar counterflow flame theoretically and experimentally. The thesis of Giovangigli (1988) characterized the extinction limits of premixed flames. DARABIHA and CANDEL (1992) studied the influence of temperature on the limits of ignition and extinction on counterflow diffusion flames. Aguerre (1996) performed experimental and numerical studies of steady and unsteady flames. Daguse (1996) investigated the effect of thermal radiation on the structure of premixed and diffusion counterflow flames. Croonenbroek (1996) studied different optical diagnostics on laminar strained flames. These studies mainly focused on gaseous flames. Versaevel (1996) studied counterflow spray flames from a theoretical and experimental point of view. More recently, several studies on two-phase counterflow flames were conducted in the EM2C laboratory. Betbeder-rey (2008) studied experimentally and numerically n-decane counterflow diffusion

flames. Alviso (2013) investigated the combustion of biodiesel using counterflow spray flames, and validated a biodiesel surrogate chemical kinetic mechanism. Franzelli et al. (2013) evaluated different tabulation techniques for spray combustion. The results proved that the chemical structure of laminar spray flame can be modeled by a multi-regime flamelet combustion model based on gaseous flamelets.

The numerical simulation of the strained coal/methane/air flames is necessary in order to study the characteristics of PCC under this configuration. Therefore, comparisons between experimental and numerical simulations are conducted. The simulations are performed using the 1D-COUNTERFLOW solver integrated with coal reactions in the REGATH package with detailed thermochemical and transport properties developed at EM2C laboratory.

5.2 Modeling of the gaseous phase

We consider an axisymmetric strained configuration as shown in Fig.5.1. Chemically reacting gas-particle flow problems are mathematically formulated using equations for gas and particle conservation of mass, momentum, energy, and species concentration. In order to model reactive two-phase flows, this three-dimensional time-dependent multi-species system of equations can be simplified taking into account the symmetry conditions in counterflow flames. The axisymmetric configuration can be formulated in cylindrical coordinates, and then further simplified to a one-dimensional formulation by a similarity approach, because the species concentrations and temperatures may be considered as independent of the radius in the vicinity of the symmetry axis. The pressure is considered constant thereafter. Volume forces on each species, including gravity, are neglected. Radiative heat transfer from the gaseous phase to the exterior is considered including reabsorption by species such as CO, CO_2, H_2O and OH.

5.2.1 Governing equations

In this section the governing equations for the continuous phase are introduced. Note that the particle diameter d_p and particle density number n are small enough, so that we may consider that the solid phase volume is negligible when compared to the gaseous phase volume. In this case, the density of gas ρ_g is used to present that of the gas-solid mixture ρ. The system of equations is completed by specifying the ideal-gas equation for the gaseous phase giving ρ_g as a function of T_g and $p\,(\rho_g = pW/RT_g\,)$.

We start by writing the equations in radial and axial coordinates respectively x and y.

Mass balance equation

$$\frac{\partial \rho_g}{\partial t} + \frac{1}{x^j}\frac{\partial (x^j \rho_g u_g)}{\partial x} + \frac{\partial (\rho_g v_g)}{\partial y} = n\dot{m}_s \tag{5.1}$$

where x and y respectively denote radial and axial coordinates. Subscripts g and s respectively designate the gaseous and solid phases, ρ, u, v, T and Y_k denote density, radial velocity, axial velocity, temperature and the k^{th} species mass fraction respectively. $\dot{m}_s$ is the mass source term of a single particle.

Species balance equation

$$\frac{\partial (\rho_g Y_k)}{\partial t} + \frac{1}{x^j}\frac{\partial (x^j \rho_g u_g Y_k)}{\partial x} + \frac{\partial (\rho_g v_g Y_k)}{\partial y} = -\frac{\partial}{\partial y}\Big(\rho_g Y_k V_{ky}\Big) + W_k \dot{\omega}_k + \gamma_{sk} n\dot{m}_s \tag{5.2}$$

where γ_{sk} is the mass fraction of k^{th} species in the volatile gases issued from coal particles. W_k and $\dot{\omega}_k$ are the molar weight and the molar chemical production rate of the k^{th} species respectively, and V_{ky} is the diffusion velocity of the k^{th} species in the axial direction. By developing the lefthand side of this equation and using Eq.(5.1), we obtain

$$\rho_g \frac{\partial Y_k}{\partial t} + \rho_g u_g \frac{\partial Y_k}{\partial x} + \rho_g v_g \frac{\partial Y_k}{\partial y} = -\frac{\partial}{\partial y}\Big(\rho_g Y_k V_{ky}\Big) + W_k \dot{\omega}_k + n\dot{m}_s (\gamma_{sk} - Y_k) \tag{5.3}$$

X-momentum continuity

$$\frac{\partial (\rho_g u_g)}{\partial t} + \frac{1}{x^j}\frac{\partial (x^j \rho_g u_g^2)}{\partial x} + \frac{\partial (\rho_g u_g v_g)}{\partial y} = -\frac{\partial p}{\partial x} + \frac{\partial}{\partial y}\Big(\mu_g \frac{\partial u_g}{\partial y}\Big) + n\dot{m}_s u_s - n f_x$$

where f_x is the radial component of the drag $\mathbf{f}$.

Similarly, developing the lefthand side of this equation using Eq.(5.1), we obtain

$$\rho_g \frac{\partial u_g}{\partial t} + \rho_g u_g \frac{\partial u_g}{\partial x} + \rho_g v_g \frac{\partial u_g}{\partial y} = -\frac{\partial p}{\partial x} + \frac{\partial}{\partial y}\Big(\mu_g \frac{\partial u_g}{\partial y}\Big) + n\dot{m}_s (u_s - u_g) - n f_x \tag{5.4}$$

Energy balance equation

$$\begin{aligned}\frac{\partial (\rho_g h_g)}{\partial t} + \frac{1}{x^j}\frac{\partial (x^j \rho_g u_g h_g)}{\partial x} + \frac{\partial (\rho_g v_g h_g)}{\partial y} &= \frac{\partial}{\partial y}\Big(\lambda_g \frac{\partial T_g}{\partial y}\Big) \\ -\frac{\partial}{\partial y}\Big(\sum_{k=1}^{K}(\rho_g Y_k V_k h_k)\Big) + \sum_{k=1}^{K}\gamma_{sk} h_k(T_s) n\dot{m}_s &- n\dot{q} - \dot{q}_R\end{aligned} \tag{5.5}$$

where h_k is the specific enthalpy of the k^{th} species and the total enthalpy h_g can be written as $h_g = \sum_{k=1}^{K} Y_k h_k(T_g)$. $\sum_{k=1}^{K} \gamma_{sk} h_k n\dot{m}_s$ is the total enthalpy issued from the solid particles, and $\dot{q}$ is the heat transfer rate from the gaseous phase to a single particle, which will be discussed later. The term $\dot{q}_R$ corresponds to the radiative heat transfer between the gaseous phase and the environment, of which the modeling method is detailed in Appendix D. Then by developing the lefthand side of this equation using Eq.(5.1), we obtain

$$\rho \frac{\partial h_g}{\partial t} + \rho u_g \frac{\partial h_g}{\partial x} + \rho v_g \frac{\partial h_g}{\partial y} = \frac{\partial}{\partial y}\Big(\lambda_g \frac{\partial T_g}{\partial y}\Big) - \frac{\partial}{\partial y}\Big(\sum_{k=1}^{K}(\rho Y_k V_k h_k)\Big) + n\dot{m}_s\Big(\sum_{k=1}^{K}\gamma_{sk} h_k(T_s) - h_k(T_g)\Big) - n\dot{q} - \dot{q}_R \tag{5.6}$$

The similarity approach is employed by searching for similar solutions of both gaseous and solid phases balance equations in the vicinity of the central axis. The similarity analysis leads to solutions of the form: $u_g = x\,U_g(y)$, $v_g = v_g(y)$, $T_g = T_g(y)$, $\rho_g = \rho_g(y)$, $Y_k = Y_k(y), k = 1, ..., K$, $u_s = x\,U_s(y)$, $v_s = v_s(y)$, $T_s = T_s(y)$, $\rho_s = \rho_s(y)$, $\alpha_s = \alpha_s(y)$, and $Y_{sdry} = Y_{sdry}(y)$. The superscript g represents gaseous phase and the superscript s the solid phase. ρ is density, u and v the radial and axial velocities respectively, T temperature. Y_k is k^{th} species mass fraction, α_s particles volume fraction, and Y_{sdry} dry coal mass fraction. U_g and U_s respectively describe the y-dependence of the transverse velocities u_g and u_s. Assuming a constant radial pressure-gradient, J describes $J = -\frac{1}{x}\frac{\partial p}{\partial x}$, and is considered constant along the axial coordinate: $\partial J/\partial y = 0$. The parameter j corresponds to 0 and 1 for two-dimensional and axisymmetric configurations, respectively. f_x and f_y are the drag forces in x and y directions. The parameter j corresponds to 0 and 1 for two-dimentional and axisymmetric configurations, respectivelely. V_{ky} is the k^{th} species diffusion velocity modeled by using mixture averaged multicomponent transport Kee et al. (1986). The governing equations, which describe the flow conservation of gaseous phase, can be written in the following form:

Mass balance equation

$$\frac{\partial \rho_g}{\partial t} + (1+j)\rho_g U_g + \frac{\partial \rho_g v_g}{\partial y} = \dot{M}_s \tag{5.7}$$

Species balance equation

$$\rho_g \frac{\partial Y_k}{\partial t} + \rho_g v_g \frac{\partial Y_k}{\partial y} = -\frac{\partial}{\partial y}\Big(\rho_g Y_k V_{ky}\Big) + W_k \dot{\omega}_k + \dot{Y}_{s,k}, \quad k = 1, \ldots, N_{sp} \tag{5.8}$$

x-momentum

$$\rho_g \frac{\partial u_g}{\partial t} + \rho_g U_g^2 + \rho_g v_g \frac{\partial U_g}{\partial y} = J + \frac{\partial}{\partial y}\Big(\mu_g \frac{\partial U_g}{\partial y}\Big) + \dot{U}_s \tag{5.9}$$

Energy balance equation

$$\rho_g \frac{\partial h_g}{\partial t} + \rho_g v_g \frac{\partial h_g}{\partial y} = \frac{\partial}{\partial y}\Big(\lambda_g \frac{\partial T_g}{\partial y}\Big) - \frac{\partial}{\partial y}\Big(\sum_{k=1}^{K}(\rho_g Y_k V_{ky} h_k)\Big) - \dot{q}_R + \dot{H}_s \tag{5.10}$$

In these equations $\dot{M}_s$, $\dot{U}_s$ and $\dot{H}_s$ represent the gas-solid coupling terms for mass, momentum and enthalpy respectively; while $\dot{Y}_{s,k}$ is the coupling term of the k^{th} species.

$$\dot{M}_s = n\dot{m}_s \tag{5.11}$$

$$\dot{Y}_{s,k} = n\dot{m}_s(\gamma_{sk} - Y_k), \quad k = 1, \ldots, K \tag{5.12}$$

$$\dot{U}_s = n\dot{m}_s (U_s - U_g) - n f_x \tag{5.13}$$

$$\dot{H}_s = n\dot{m}_s \sum_{k=1}^{K}(\gamma_{sk} h_k(T_s) - Y_k h_k(T_g)) - n\dot{q} \tag{5.14}$$

5.3 Modeling of the particle phase

5.3.1 Coal sub-model assumptions

In this section, we introduce the conservation equations describing the combustion of pulverized coal particles. Therefore, the process of evaporation has been illuminated. The parameters that quantify the heterogeneous and homogeneous reaction during the coal devolatilization and char oxidation will be presented in the next chapter.

We admit these following assumptions :

- We consider only the transformation of solid phase to gaseous phase, i.e. the process of pyrolysis and the surface oxidation of char produced.
- The coal particles are dry, ash-free.
- During the coal conversion process, the diameter of coal particles remains constant.

- All the particles are considered monodisperse.
- The temperature is uniform at the surface of each particles.
- The global particle volume is very small compared to that of the gaseous phase.
- Interactions between the particles are neglected.

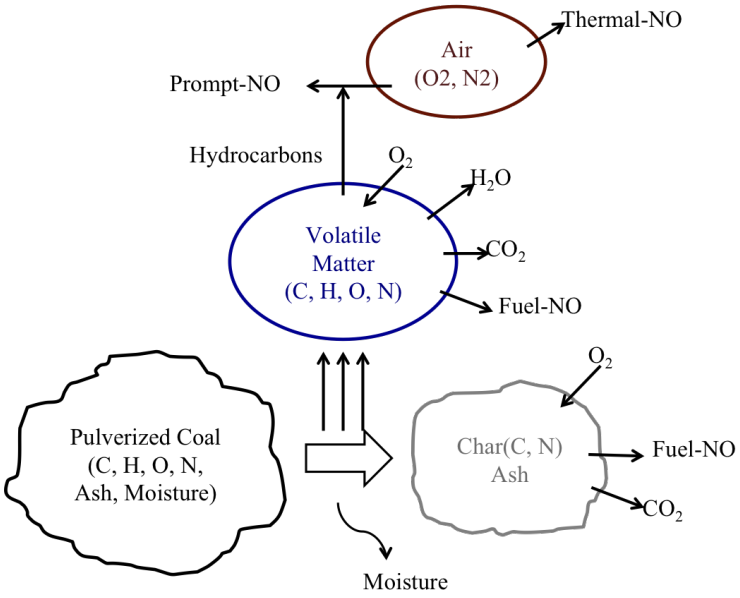

Figure 5.2: *Ilustration of the pyrolysis model*

We define these following terms.
VARIABLES:

- $Y_{s,dry}$: the mass fraction of dry coal contained in the solid phase that will undergo the pyrolysis.
- $Y_{s,char}$: the mass fraction of char contained in the solid phase, which is produced during the pyrolysis and consumed by the combustion. The solid phase is composed by the dry coal and char, so we obtain the following equation:

$$Y_{s,dry} + Y_{s,char} = 1 \tag{5.15}$$

- d_p: the diameter of coal particles.
- ρ_s: the density of solid phase, which decreases during the process of pyrolysis and oxidation, because we assume that the diameter of coal particle remains constant.
- α_s: the volume fraction of solid phase, related to the porosity of coal and

it only changes if the diameter of particles changes during the combustion process.

- T_s: the temperature of coal particle

PARAMETERS:

- $C_{p,s}$: the specific heat value of solid phase
- Δh_{pyr}: the heat of pyrolysis, which can be calculated from
- Δh_{char}: the heat of char combustion, this is the enthalpy change of char oxidation reaction.

SOURCE TERMS

- $\dot{\omega}_{s,pyr}$: the pyrolysis rate of coal from which volatiles are issued and char is derived

$$dry\ coal \quad \rightarrow \quad \nu_{char} char + (1 - \nu_{char})\, volatiles \tag{5.16}$$

where ν_{char} is the mass fraction of char which remains constant during the pyrolysis.

- $\dot{\omega}_{s,char}$: the oxidation rate of char reacting with oxygen at the particle surface. Possible char oxidation reactions are

$$\begin{aligned} char + O_2 \quad &\rightarrow \quad CO_2 \\ char + \frac{1}{2}O_2 \quad &\rightarrow \quad CO \end{aligned} \tag{5.17}$$

which correspond to full and partial oxidation of carbon. The difference between considering full or partial reactions will be discussed later in section 7.4.

- $\dot{m}_s$: the mass source term from the release of volatiles to the gaseous phase due to devolatilization and the consumption and release of gases due to char combustion
- $f_{x,y}$: the drag forces in x and y directions

5.3.2 Governing equations

Employing similarity approach with the assumptions introduced formerly, we can write the conservation equation for the monodisperse particles:
Mass balance equation

$$\frac{\partial\, \alpha_s \rho_s}{\partial t} + (1 + j)\alpha_s \rho_s U_s + \frac{\partial\, (\, \alpha_s\, \rho_s v_s\,)}{\partial y} = -n\dot{m}_s \tag{5.18}$$

Species balance equation

$$\alpha_s \rho_s \frac{\partial Y_{s_{dry}}}{\partial t} + \alpha_s \rho_s v_s \frac{\partial Y_{s_{dry}}}{\partial y} = -\dot{\omega}_{s_{pyr}} + Y_{s_{dry}} n\dot{m}_s \tag{5.19}$$

x-momentum

$$\alpha_s \rho_s \frac{\partial U_s}{\partial t} + \alpha_s \rho_s U_s^2 + \alpha_s \rho_s v_s \frac{\partial U_s}{\partial y} = n f_x \tag{5.20}$$

y-momentum

$$\alpha_s \rho_s \frac{\partial v_s}{\partial t} + \alpha_s \rho_s v_s \frac{\partial v_s}{\partial y} = \alpha_s \rho_s g + n f_y \tag{5.21}$$

Energy balance equation

$$\begin{aligned} \alpha_s \rho_s C_{p_s} \frac{\partial T_s}{\partial t} + \alpha_s \rho_s v_s C_{p_s} \frac{\partial T_s}{\partial y} &= -\dot{\omega}_{s_{pyr}} \Delta h_{pyr} \\ - \dot{\omega}_{s_{char}} \Delta h_{char} - \sum_{k=1}^{K} \gamma_{sk} h_k(T_s) n\dot{m}_s + n\dot{q} \end{aligned} \tag{5.22}$$

5.3.2.1 Reaction rates

The total mass volatilization rate of particles is given by:

$$n\dot{m}_s = (1 - \nu_{char})\dot{\omega}_{s_{pyr}} + \dot{\omega}_{s_{char}} \tag{5.23}$$

The devolatilization rate is modeled using the single-step and two-step model introduced in Section 4.2.1.1,

$$\dot{\omega}_{s_{pyr}} = \left(\alpha_s \rho_s Y_{s_{dry}}\right) k_{pyr} \exp\left(\frac{-E_{pyr}}{RT_s}\right) \tag{5.24}$$

And

$$\dot{\omega}_{s_{pyr}} = \left(\alpha_s \rho_s Y_{s_{dry}}\right) [\alpha_1 k_1 \exp\left(\frac{-E_1}{RT_s}\right) + \alpha_2 k_2 \exp\left(\frac{-E_2}{RT_s}\right)] \tag{5.25}$$

The char reaction rate is modeled by the diffusion-kinetic model presented in Section 4.2.3.

$$\dot{\omega}_{s_{char}} = (\alpha_s \sigma_s) X_{O_2} P_0 \frac{K_c K_d}{K_c + K_d} \tag{5.26}$$

5.3.2.2 Drag forces

The radial and axial components of the drag force are described by the Stokes law

$$f_x = 3\pi \mu_g d_p (U_g - U_s) \tag{5.27}$$

$$f_y = 3\pi \mu_g d_p (v_g - v_s) \tag{5.28}$$

5.3.3 Particle heat transfer

The heat transfer between solid fuel particles and gas consists of particle-gas convective and radiative heat transfers. The energy source term due to convective and radiative heat transfer $n\dot{q}$ is written as

$$n\dot{q} = \dot{Q}_{conv} + \dot{Q}_{rad} \tag{5.29}$$

5.3.3.1 Convective heat transfer

$$\dot{Q}_{conv} = A_p k_{conv} (T_g - T_s) = \alpha_s \sigma_s k_{conv} (T_g - T_s) \tag{5.30}$$

where A_p is the particle surface area. The surface-to-volume ratio σ_s is calculated by particle size given the concentration of coal particles N_{part}/V_{tot} and the particle size r_{part}.

$$\alpha_s = V_s/V_{tot} = N_{part}V_{part}/V_{tot} = 3\pi N_{part} r_{part}^3/4V_{tot} \tag{5.31}$$

$$\sigma_s = A_s/V_s = 3/r_{part} \tag{5.32}$$

k_{conv} is the heat transfer coefficient of coal particles, then

$$k_{conv} = Nu\lambda_g/d_p \tag{5.33}$$

d_p is the diameter of the particle, Nu is the Nusselt number. And according to the Ranz-Marshall correlation model (Ranz and Marshall, 1952):

$$Nu = 2 + 0.6Re_p^{1/2}Pr^{1/3} \tag{5.34}$$

Re_p is the particle Reynolds number, Pr is the Prantl number $Pr = C_p\mu_g/\lambda_g$ calculated from heat capacity of gas, gas viscosity and thermal conductivity. Nu is considered as 2 in the present work.

5.3.3.2 Radiative heat transfer

To compute the net energy flux into a volume element, the radiative heat flux through the medium needs to be known and is thus necessary to be calculated. The solution has to take account for absorption and emission of thermal radiation for both phases, as well as scattering by the coal particles.

Due to the complexity of modeling coal particle radiation, the Stefan-Boltzmann model is considered in our work:

$$\dot{Q}_{rad} = \epsilon A_p \sigma \left(T_w^4 - T_s^4\right) = \epsilon \alpha_s \sigma_s \sigma \left(T_w^4 - T_s^4\right) \tag{5.35}$$

where ϵ is the emissivity of coal particles, which is assumed to be 0.85 from Kurose et al. (2004), σ is the Stefan-Boltzmann constant.

5.4 Numerical methods

The Newton method is used for the resolution of the equations. In general, the partial differential system can be writen as

$$\mathcal{F}(\boldsymbol{U}) = 0 \tag{5.36}$$

where $\mathcal{F}$ is the differential equation system of $\boldsymbol{U}$ and $\boldsymbol{U} = \{U_1, ..., U_j, ..., U_M\}$ is solution vector, M is number of variables in the system.
Here, $\boldsymbol{U} = \{T_g, Y_k, u_g, v_g, T_s, u_s, v_s, \alpha_s, \rho_s, Y_{s_{dry}}\}$.

The problem can then be formulated by introdusing a mesh $\boldsymbol{X} = \{x_1, ..., x_i, ..., x_N\}$, N is number of points in the mesh for the discrete space:

$$\boldsymbol{F}(\boldsymbol{S}) = 0 \tag{5.37}$$

where $\boldsymbol{S}$ is discrete solution vector for each variable at each point of the mesh $\boldsymbol{S} = \{s_j(x_i)\}$. And $\boldsymbol{F}$ is the differential equation system of $\boldsymbol{S}$.

The equation (5.37) is then solved iteratively,

$$\boldsymbol{F}(\boldsymbol{S_k}) + \frac{\partial \boldsymbol{F}}{\partial \boldsymbol{S}}(\boldsymbol{S_k})(\boldsymbol{S_{k+1}} - \boldsymbol{S_k}) = 0 \tag{5.38}$$

where $\boldsymbol{S_k}$ and $\boldsymbol{S_{k+1}}$ are the estimation of $\boldsymbol{S}$ at iteration k and $k+1$, respectively. From Equation 5.23 we can deduce an equation for $\boldsymbol{S_{k+1}}$:

$$\boldsymbol{S_{k+1}} = \boldsymbol{S_k} - [\nabla \boldsymbol{F}(\boldsymbol{S_k})]^{-1} \boldsymbol{F_k} \tag{5.39}$$

The Jacobian matrix $\boldsymbol{J} = \nabla \boldsymbol{F}(\boldsymbol{S_k})$ and its inversion are then calculated numerically.

Summary of the chapter

This chapter presents the 1-D formulation of coupled gas-solid simulations on the current configuration. The system of equations includes radiation heat transfer as well as coal devolatilization and oxidation. This gas-solid coupling is handled by the 1D-couterflow solver developed in the REGATH code, which allows for detailed information on the thermal history of gas and coal particles, along with concentration of reactive species, offering the possibility for comparison with experimental data and validation of the modeling approach. Such numerical configuration is useful to provide a comprehensive understanding of the mechanisms as well as the characteristics of coal conversion. It is also very helpful to evaluate different coal sub-models.

Chapter 6

Numerical setup and validation

This chapter presents the numerical setup used to perform the simulations of coal devolatilization and oxidation in strained $CH_4/O_2/N_2$ flames. The boundary conditions are introduced, followed by the parameters describing coal conversion. Then chosen chemical mechanism along with sub-mechnisms for OH^*, CH^* and C_2^* chemiluminescence reactions used in the simulations will be given. Finally, typical numerical results of one particular condition will be introduced and validated with experiments.

6.1 Numerical setup

6.1.1 Boundary conditions

The set of equations for gaseous and solid phases, as well as the strained flow configuration have been presented in the previous chapter. Concerning boundary conditions, the temperature at the burner exit is at an initial value of T_0 = 310 K. The the temperature of the brass plate is measured by thermocouple which gives T_H = 600 K and is modeled as an isothermal wall. Gas axial velocities at the left side are given in Table 3.1. The particle velocity has been measured by PIV. PIV results show that the particle average velocity matches the gas velocity at the injector exit. A typical profile is available in Appendix B.

The diameter of injected particles corresponds to the Sauter Mean Diameter measured by microscope: $d_p^0 = 15\ \mu m$ and the particle number density (per unit volume) is estimated $n_s = 1.14 \times 10^9$ particles per m^3 from coal mass flow rate measurements, which leads to $\alpha_s^0 = 2.0 \times 10^{-6}$. The initial properties of coal particles used for the simulations are: $\rho_s^0 = 909\ kg/m^3$, and the constant pressure heat capacity $c_{ps} = 1.5\ kJ/(kgK)$. In addition, the pressure is equal to one atmosphere. The distance between the burner exit and the stagnation plane H is equal to 20 mm.

Boudary conditions are given in Table 6.1. In this table, "left" corresponds to the inlet jet position ($y = 0$) and "right" corresponds to the wall postion (y = H).

	left ($y = 0$)	right (y = H)
Gas temperature	$T_g = T_0$	$T_g = T_H$
Species mass fractions	$Y_k = Y_k^0$	zero gradient
Gas axial velocity	$v_g = v_0$	$v_g = 0$
Gas radial velocity	$u_g = u_0$	$u_g = 0$
Particle temperature	$T_s = T_0$	$T_s = T_H$
Particle axial velocity	$v_s = v_0$	$v_s = 0$
Particle radial velocity	$u_s = u_0$	$u_s = 0$
Particle volume fraction	$\alpha_s = \alpha_s^0$	zero gradient
Particle density	$\rho_s = \rho_s^0$	zero gradient
Particle diameter	$d_p = d_p^0$	zero gradient
Particle number density	$n_p = n_p^0$	zero gradient

Table 6.1: *Boundary conditions (gas and particles coming from the left)*

6.1.2 Parameters of coal sub-models

The coal particle is considered dry and ash-free. We consider only the transformation of solid phase to gaseous phase, i.e. the process of pyrolysis:

$$Coal \Longrightarrow (1 - \nu_{char})\, Volatile + \nu_{char}\, Char$$

and the surface oxidation:

$$Char \Longrightarrow (1 + \nu_{O_2})\, CO_2$$

The total mass loss rate of particle phase is given by:

$$n\dot{m}_s = (1 - \nu_{char})\, \dot{\omega}_{s_{pyr}} + \dot{\omega}_{s_{char}}$$

Coal devolatilization source term $\dot{\omega}_{s_{pyr}}$ will be modeled either by first-order single reaction model (Badzioch and Hawksley 1970) or by a 2-step model (Kobayashi et al. 1977). The kinetic-diffusion model (Baum and Street 1971) is used for char oxidation source term $\dot{\omega}_{s_{char}}$. The parameters for single reaction model and char oxidation model are modeled as in Ranade and Gupta (2014), and the 2-step model parameters are taken from Lemaire et al. (2014). The heat transfer between gas and particle phase is decomposed as:

$$n\dot{q} = \dot{Q}_{conv} + \dot{Q}_{rad}$$

The convective heat transfer is given by

$$\dot{Q}_{conv} = \alpha_s \sigma_s k_{conv} (T_g - T_s)$$

where σ_s is the particle surface/volume ratio, k_{conv} is the heat transfer coefficient of coal particles calculated assuming a Nusselt number of 2. The radiative heat transfer is given by

$$\dot{Q}_{rad} = \epsilon \alpha_s \sigma_s \sigma \left(T_w^4 - T_s^4\right)$$

where the radiation temperature T_w is set as the boundary temperature in this configuration, the emissivity of coal particles $\epsilon = 0.85$ is kept constant in all simulations, and σ is the Stefan-Boltzmann constant. The kinetic parameters describing the pyrolysis and char oxidation reactions (equations 5.24 to 5.26) are summarized in Table 6.2.

Item	Parameter	Value
One-step devolatilization	A	$1.58 \times 10^8 1/s$
	E	$1.29 \times 10^5 J/molK$
Two-step devolatilization	A_1	$2.0 \times 10^5 1/s$
	E_1	$1.05 \times 10^5 J/molK$
	A_2	$1.3 \times 10^7 1/s$
	E_2	$1.67 \times 10^5 J/molK$
Diffusion-kinetic char oxidation	A_c	$2.7 \times 10^{-3} kg/(m^2 sPa)$
	E_c	$9.43 \times 10^4 J/molK$

Table 6.2: *Parameters for coal sub-models*

6.1.3 Determination of volatile compositions

As indroduced in section 4.2.1, the composition of volatile matter of a certain coal type can be obtained from network models such as CPD (Chemical Percolation Devolatilization) model (Grant et al. 1989), FG-DVC model (Solomon et al. 1988) and FLASHCHAIN model (Niksa and Kerstein 1991). The lignite employed in the present work is Heizprofi (HP) (see Appendix A). However, there is no volatile mater compostion available for this lignite. Therefore in this study, its total volatile matter (TVM) composition is considered as similar to the composition of lignite coals South Beulah (SB) and Morwell (MW) identified by Xu and Tomita (1987a). We use the data published by Hara et al. (2015) obtained from the CPD model. It predicts the formation of CH_4, CO, CO_2, H_2, H_2O, C_2H_4, C_2H_6, C_3H_6, C_3H_8, and tar (represented by C_6H_6). The properties of these lignite coals, i.e. HP, SB and MW coal, are listed in Table 4.1. Table 6.3 shows the mass percentage of different volatile species of SB and MW coal.

Coal Name	CH_4	CO	CO_2	H_2	H_2O	C_2H_4	C_2H_6	C_3H_6	C_3H_8	tar(C_6H_6)
SB	3.4	17	15	0.66	12	1.04	1.04	1.04	0.52	48.3
MW	4.7	19	24	0.64	15	0.96	0.96	0.96	0.48	33.3

Table 6.3: *Mass percentage of species in TVM from pyrolysis of SB and MW*

6.1.4 Chemical kinetic mechanisms

Simulations are performed using REGATH code for the strained flow flame with detailed chemistry and mixture averaged multicomponent transport. To model the gaseous combustion kinetics, we have employed the $H_2/CO/C_1$-C_4 mechanism USC-Mech II (Wang et al. 2007) consisting of 111 species and 784 reactions.

Flame chemiluminescence has been widely employed as simple and nonintrusive optical diagnostic for combustion systems. The ability of interpreting chemiluminescence intensity to monitor equivalence ratio, heat release rate, pollutant emission and flame front location has been proved by previous studies (Kojima et al. 2005; Leo et al. 2007; Panoutsos et al. 2009; Liu et al. 2017). In order to predict the reaction rates of the excited species formation, kinetic studies of gaseous flames (Smith et al. 2002; Smith et al. 2005; Kathrotia et al. 2012) have been performed by different researchers. However, because of lack of experimental data of coal flames, the ability of chemical kinetics models in prediction of coal flame chemiluminescence is still an open issue.

To enable comparison with OH^*, CH^* and C_2^* measurements, the reaction kinetics used by Alviso et al. (2015) and Kathrotia et al. (2012) have been also added to the USC-Mech II mechanism. This allows us to compute excited-

state concentrations as well as chemiluminescence intensities in the flame. The mechanisms of Alviso et al. (2015) and Kathrotia et al. (2012) are given in Appendix C and are summarized in Table 6.4.

Name	CH_4 mechanism	Excited Species	Source
mech A	USC-Mech II	OH^*, CH^*, C_2	Alviso et al. (2015)
mech K	USC-Mech II	OH^*, CH^*, C_2^*	Kathrotia et al. (2012)

Table 6.4: *Sub-mechanisms of excited species*

We have validated these two mechanisms combined with USC-Mech II for the methane/air combustion and flame speed by performing freely-propagating premixed 1-D flames and by comparing them to experimental data from Vagelopoulos et al. (1994) and Vagelopoulos and Egolfopoulos (1998). Figure 6.1 presents flame speed as a function of equivalence ratio. As expected, due to the low concentration of the excited species, no significant difference in the results was found with the addition of these elementary reactions. The thermochemical data for OH^*, CH^* and C_2^* were added as well. The transport coefficients for the excited species were the same as those of the ground state species. The results presented in this and the next chapter are performed using mech A, if not specified.

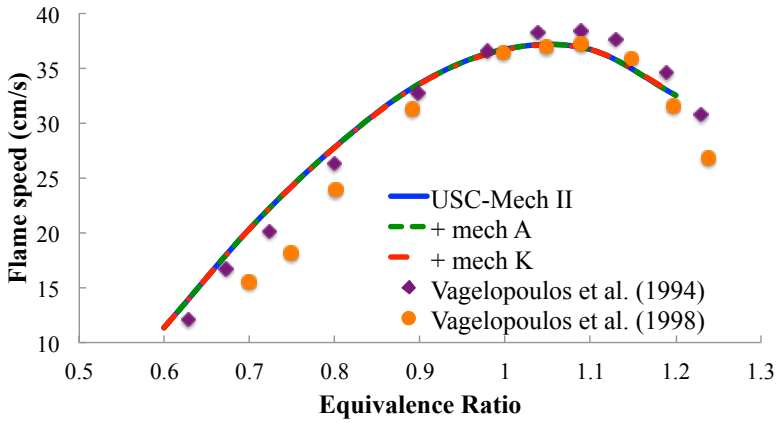

Figure 6.1: *Methane/air flame speed as a function of equivalence ratio*

6.2 Validation case

6.2.1 Typical flame structure

Figure 6.2 presents a typical CH_4/coal/air flame structure. The numerical conditions correspond to CH_4/coal/air flame A1 (see Table.3.1), with a methane/air

equivalence ratio of 0.88 and strain rate of 260 s^{-1}. In all figures in this chapter $y = 0$ corresponds to the burner exit and $y = 20$ to the brass plate. The premixed methane/air flame front is located at about $y = 16.14\,mm$. At this point, the gas temperature increases very rapidly from 310 K to about 1700 K within 0.6 mm. The maximum temperature of gas and particle are 2034 K and 1485 K, respectively. The particle temperature continues to increase in the burnt due to the heat exchange with the gas phase and to the coal devolatilization and oxidation reactions.

This figure also presents the axial velocity profiles of gas and coal particles, where the gas axial velocity decreases from the burner exit due to the presence of the stagnation plane, and it reaches a minimum before the flame front. As the flow enters the flame, due to preheating and thereby thermal expansion, the axial velocity increases and reaches a maximum just after the peak of the heat release. After the heat release, the axial velocity decreases to zero at the stagnation plane.

The difference between gas and particle temperature is essentially due to the endothermic reactions of coal pyrolysis. The exothermic char oxidation reactions, however, does not play an important role under the present configuration (see section 7.1 for detailed discussion). Moreover, the particles reach thermal equilibrium after the rapid heating when passing through the methane flame front.

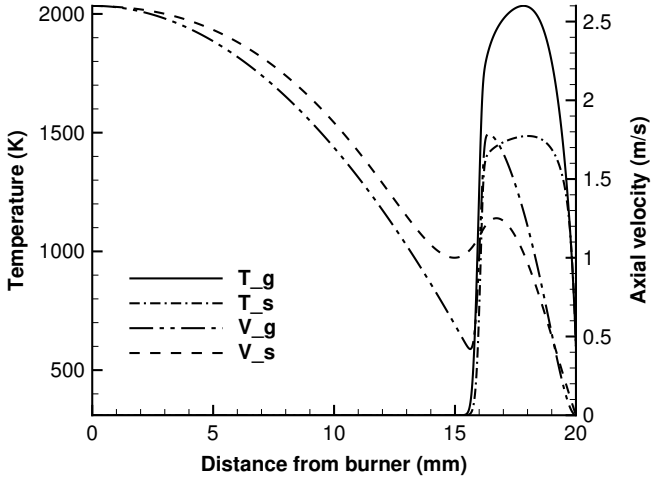

Figure 6.2: *Typical flame structure: temperature and axial velocity profiles of gas and particle for CH_4/coal/air flame A1*

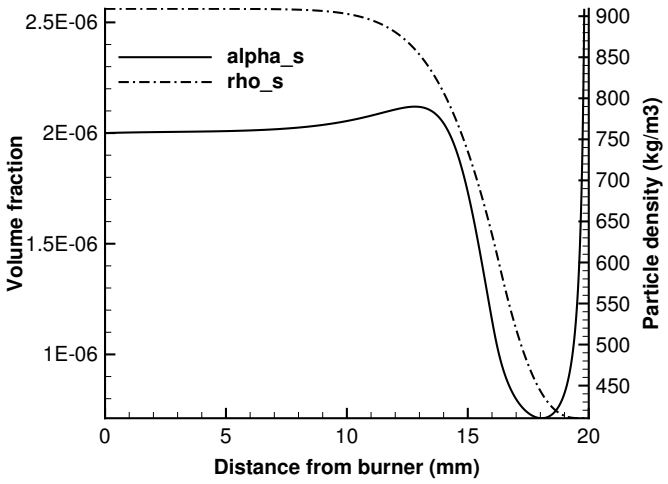

Figure 6.3: *Particle volume fraction and density profiles of CH_4/coal/air flame A1*

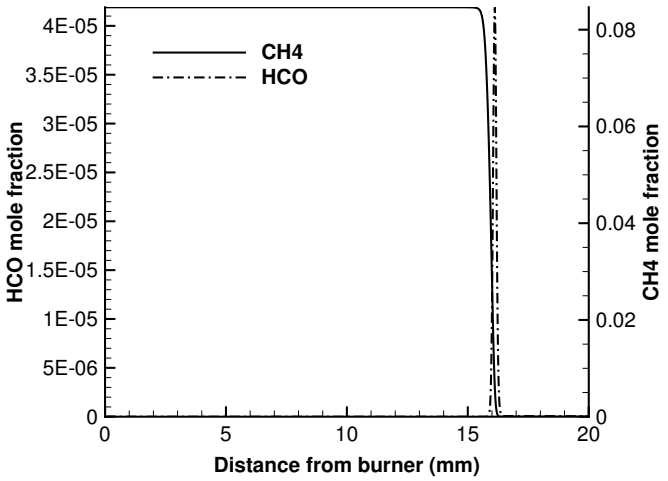

Figure 6.4: *CH_4 and HCO mole fractions of CH_4/coal/air flame A1*

Devolatilization results in the release of volatile gases, therefore the particle density decreases, see Fig.6.3, partly because of char oxidation as well. The particle number density increases slightly before the flame front due to the decrease of the flow velocity and then diminishes very rapidly as the flow velocity increases with heat release, thus increasing the profile of particle volume fraction α_s.

Figures 6.4 to 6.6 present typical CH_4/coal/air flame species profiles. All species concentrations are presented in mole fractions. The boundary conditions cor-

respond to CH_4/coal/air flame A1. Figure 6.4 presents CH_4 and HCO species profiles. HCO is a major intermediate species in the oxidation of CH_4 to CO_2. It is considered as a good indicator of the heat release rate (HRR) for premixed methane-air flames, according to Nikolaou and Swaminathan (2014). HCO also indicates the flame front position because this species is present only in the reaction zone. CH_4 mole fraction remains constant until it reaches the flame front position, then decreases rapidly. As for the coal particles, CH_4 mole fraction is relatively small compared to other volatile species, therefore methane is not formed in large quantities.

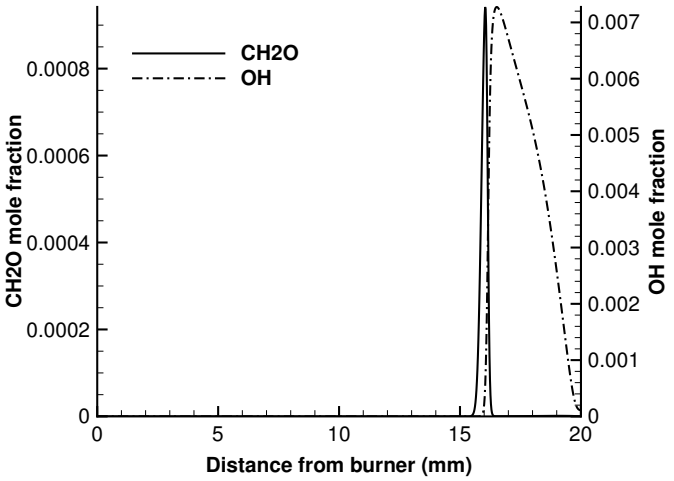

Figure 6.5: *CH_2O and OH mole fractions of CH_4/coal/air flame A1*

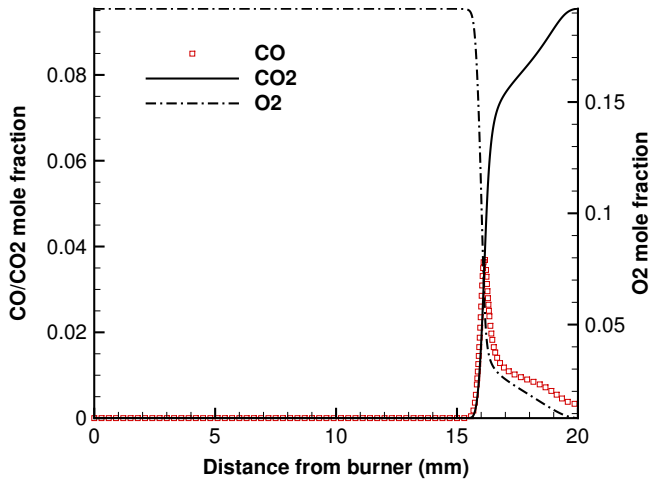

Figure 6.6: *CO, CO_2 and O_2 mole fractions of CH_4/coal/air flame A1*

CH_2O and OH species profiles are presented in Fig.6.5. CH_2O profile reaches a peak and drops sharply. The location where CH_2O peaks is also approximately the flame front position. The maximum of the CH_2O profile lies slightly ahead of the rising slop of OH. Mulla et al. (2016) compared the correlation between HRR and the product of CH_2O and OH concentrations. They concluded that [OH]×[CH2O] is suitable markers of HRR for premixed methane-air flames.

In Fig.6.6 are presented CO, CO_2 and O_2 species profiles. Concerning O_2 the oxidizer, the mole fraction remains constant from the burner exit until it reaches the flame zone, then decreases very sharply due to the rapid reactions of CH_4 with oxygen. However, the volatile species as well as coal char continue to react with the oxidizer, O_2 mole fraction decreases in the burnt gases instead of a plateau. In the burnt gases, CO and CO_2 mole fraction also increase due to the contribution of coal pyrolysis and char oxidation. Finally, in Fig.6.7 it is shown that C_2H species has a similar profile as CH^* radical. This explains the main formation paths of CH^* via reactions 2.6.

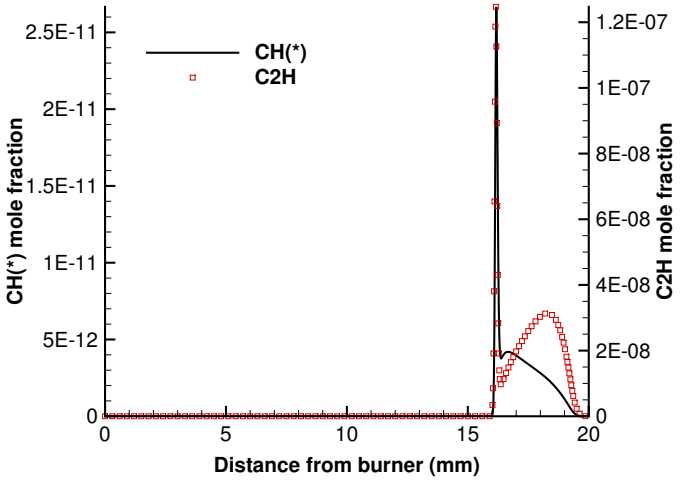

Figure 6.7: *CH^* and C_2H mole fractions of CH_4/coal/air flame A1*

6.2.2 Comparison between CH_4/air and CH_4/coal/air flames

Figure 6.8 gives a comparison of gas temperature and HCO species mole fraction between CH_4/air and CH_4/coal/air for Flame A1. The coupling between gaseous and solid phases will result in the mass and heat transfer between gas and solid, which originates the variation of local equivalence ratio and flame speed, as well as convection and radiation due to the presence of coal particles. The gas temperature increases when the impact of coal devolatilization and oxidation on the gaseous phase is accounted for. This increase of temperature is due to the local augmentation of the fuel/air equivalence ratio induced by

the release of volatile gases, which has similar effect on flame speed. According to the HCO species profile in Fig.6.8, it can be seen that there is a noticeable difference of the flame front positions. This is beacuse the CH_4/coal/air flame speed is slightly higher than that of the CH4/air flame, therefore the flame front slightly moves towards upstream.

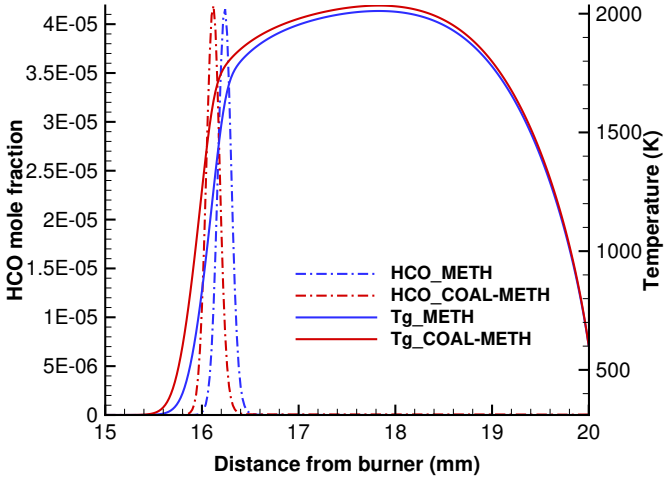

Figure 6.8: *Comparison of gas temperature and HCO mole fraction of CH_4/air and CH_4/coal/air flame A1*

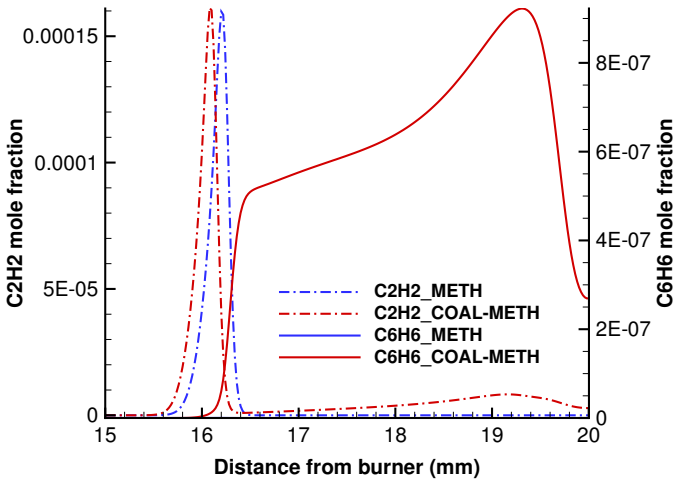

Figure 6.9: *Comparison of C_2H_2 and C_6H_6 mole fraction of CH_4/air and CH_4/coal/air flame A1*

Concerning other species profiles, the difference of peak position and maximum

value has been observed between CH_4/air and CH_4/coal/air solutions. Figure 6.9 presents mole fraction profiles of C_6H_6 and C_2H_2, which are linked to the volatile species of coal pyrolysis. Formation of these two species, also involved in the soot formation process, are mainly influenced by the coal devolatilization. As shown in Fig.6.9, in the hot region, C_2H_2 mole fraction increases in CH_4/coal/air flame, while it is localized at the flame front in CH_4/air flame. C_6H_6 is not present in CH_4/air flame. Indeed, the presence of heavy hydrocarbons in the TVM promotes the formation of soot precursors in the burnt gases, localized between the flame front and the wall. More discussion on the TVM compostion will be presented in the next chapter.

6.2.3 Comparison between experimental and numerical profiles of OH^* and CH^* and C_2^*

6.2.3.1 Normalization procedure

As the measurements do not give absolute values, in order to make comparisons, all numerical profiles are normalized by the maxima of OH^*, CH^* and C_2^* concentration calculated using mech A and mech K (Table 6.4) corresponding to CH_4/air Flame A1 (without coal particles) respectively. All experimental profiles are normalized by the maxima of OH^*, CH^* and C_2^* emission corresponding to CH_4/air Flame A1 from FES signals respectively. Figure 6.10 shows an example how the normalization is performed. CH_4/air Flame A1 is chosen as the reference case. The normalized experimental and numerical OH^* mole fractions $X^*_{OH^*}$ are then calculated by the following equations:

$$[X^*_{OH^*}]_{exp} = \frac{OH^*_{FES}}{max([OH^*_{FES}]_{A1})} \tag{6.1}$$

$$[X^*_{OH^*}]_{num} = \frac{OH^*_{num}}{max([OH^*_{num}]_{A1})} \tag{6.2}$$

Therefore experimental and numerical OH^* profiles of this flame is normalized from the maxima of 700 and 4.5E-10 to 1 respectively. Since the two sub-mechanisms result in different absolute values, as shown in Fig.6.12, the normalization is performed respectively correponding to the CH_4/air Flame A1 predicted using each sub-mechanism. The similar procedure is applied to CH^* and C_2^* profiles respectively.

For C_2^* profiles, the C_2 in mech A (Appendix C) is used to represent the C_2^* radical, because no quenching reactions is included for C_2^* radical in both mech A and K, therefore the mole fraction of C_2 is suitable to present C_2^* radical. This assumption is validated by mech K, where the calculated absolute C_2^* mole fraction equals to that of C_2 in Fig.6.11.

The reason for this normalization procedure is that all the other operating conditions are therefore comparable with the "calibration" case A1. The comparisons with experimental profiles can be then considered semi-quantitative.

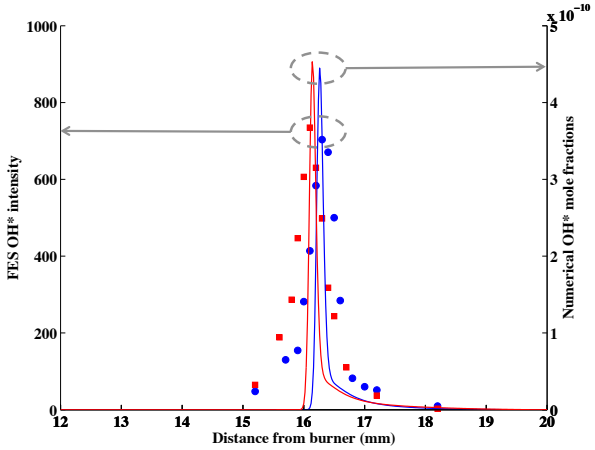

Figure 6.10: *Comparison of OH* between spectroscopy measurements (circle and square) and numerical profiles (using mech A) for CH_4/air (blue) and CH_4/Coal/air (red) flame A1*

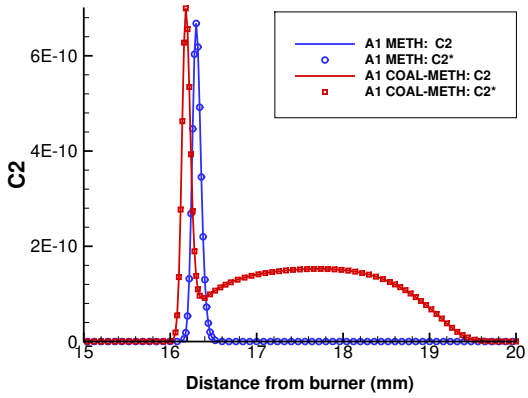

Figure 6.11: *Comparison of C_2 and C_2^* absolute numerical profiles using mech K for CH_4/air (blue) and CH_4/Coal/air (red) flame A1*

Normalized experimental and numerical OH* and CH* and C_2^* profiles are thus shown in Fig.6.13.

6.2.3.2 Comparison of flame A1

Comparisons between numerical results and FES signals of flame A1 are presented as the validation of numerical setup. The simulations are performed for

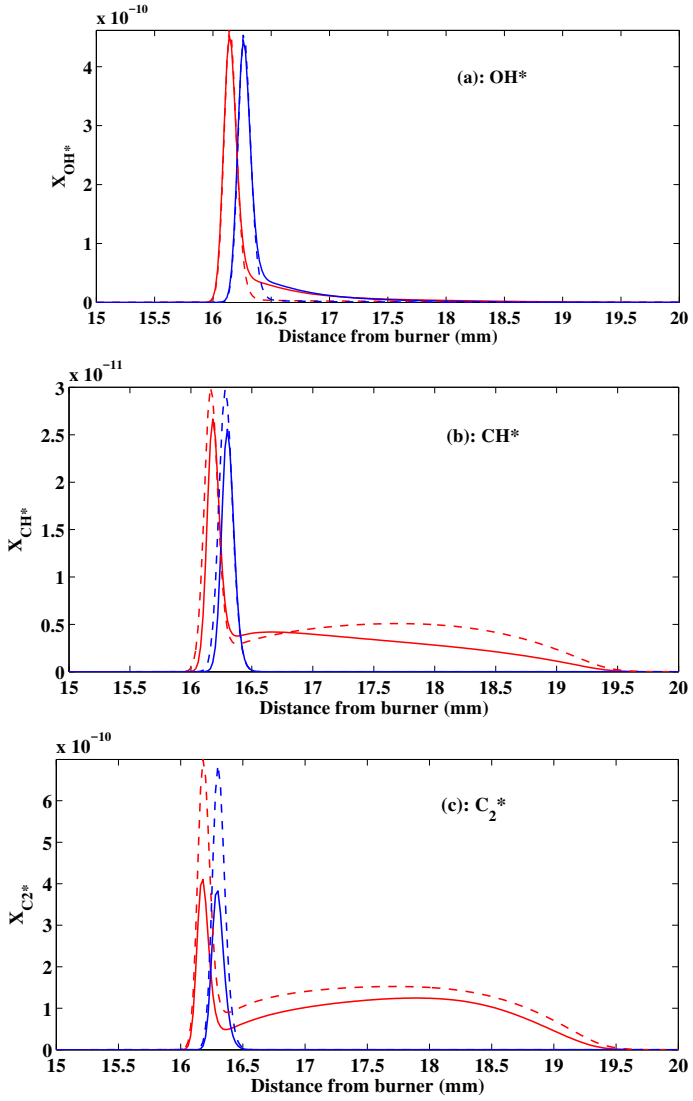

Figure 6.12: *Comparison between numerical profiles (mech A: solid line, mech K: dased line) for CH_4/air (blue) and CH_4/Coal/air (red) flame A1: (a) OH^*, (b) CH^*, (c) C_2^**

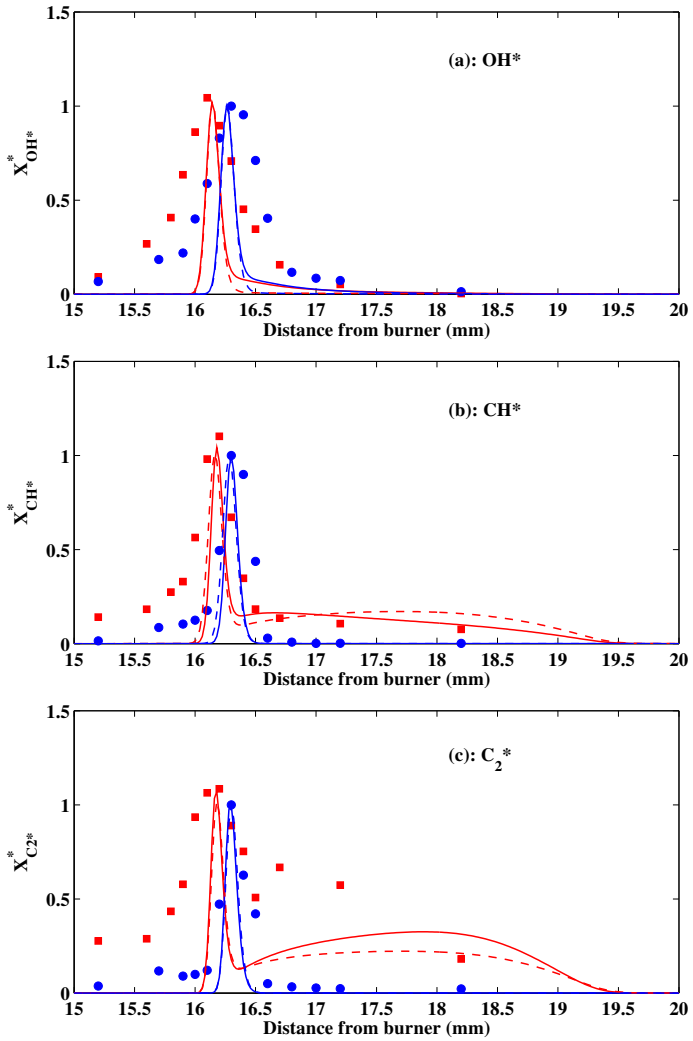

Figure 6.13: *Comparison between spectroscopy measurements (circle and square) and numerical (mech A: solid line, mech K: dased line) profiles for CH_4/air (blue) and CH_4/Coal/air (red) flame A1: (a) OH^*, (b) CH^*, (c) C_2^**

the same operating condition using two sub-mechanisms for chemiluminescent species. The aim is to better understand the dependency of simulated OH^*, CH^* and C_2^* emission characteristics on chemical kinetic schemes. The two sub-mechnisms have been introduced in Table 6.4.

As we can see in Fig.6.13, the numerical predictions of OH^*, CH^* and C_2^* mole fractions are very close to the experimental profiles along the axis. The positions of the peaks match both for CH_4/air and CH_4/coal/air flames. The experimental profiles have larger thickness than the simulated ones. This may be explained by the broadening of the experimental profiles. According to Alviso (2013), one possible cause is photon deviation due to a high temperature gradient. In fact, in a counterflow premixed flame, the temperature gradient induces a change in the milieu refractive index, causing a deviation of photons emitted by the flame, and therefore producing a broadening of species experimental profiles. Furthermore, the FES signal may contain the projection of the whole detected volume. This may be why the signal before flame front is more affected.

The variation trends of all three species are well predicted by both sub-mechanisms, that is, chemical reactions in the hot gases related to the coal conversion are detected through flame chemiluminescence, considering the very small concentration of the measured species and the uncertainties in the excited radical kinetic modeling. The abusolute values of OH^* and CH^* predicted by two sub-mechanisms are slightly different. The predicted C_2^* concentration, however, shows more important difference in terms of absolute value. This is due to the difference in the sub-mechanisms for C_2 reactions. Another source of discrepancy in the hot region between the predicted and measured intensities of CH_4/Coal/air flames can be due to the uncertainty of coal feeding rate.

Summary of the chapter

This chapter presents the numerical setup and simulation results based on the approach developed in the previous chapter. The coupled 1-D calculations are representative of the devolatilization and oxidation of pulverized coal particles in a laminar strained flow configuration. The chemical mechanisms underlying methane combustion as well as chemiluminecent reactions are used. The thermal conversion of coal particles that produces volatile gas reactants is considered in the solid phase, while and the oxidation of these gas reactants is taken into account by the combined mechanisms. Two sub-mechanisms are validated by the comparison with experimental data. They are both able to predict the emission characteristics of CH_4/coal/air flames, although differences in absolute values are observed. This modeling approach will be further evaluated by the comparative study of experiments and simulations in the next chapter. The relevance of coal sub-models as well as the assumptions used to describe coal

conversion will be examined in detail.

Chapter 7

Parametric studies and discussion

In the present chapter, results of numerical simulations for different experimental conditions presented in Section 3.2.1 are analyzed. Parametric studies are performed to investigate the influences of CH_4/O_2 equivalence ratio and O_2 mole fraction in the oxidizer stream on flame emission characteristics. In addition, coal sub-models are varied for one particular operating point. The effects of coal sub-models on the prediction of flame emission characteristics are also highlighted. We observe that the accuracy of coal combustion prediction depends greatly on the choice of coal-related models and parameters. Different coal sub-models enable to better understand the mechanisms leading to coal conversion process as well as the influence on flame chemiluminescence.

7.1 Influence of strain rate

In order to study the influence of strain rate on OH^*, CH^*, and C_2^* mole fraction profiles, two numerical simulations are performed by varying the injection velocity V_u (Eq.2.2) in order to compare with CH_4/coal/air flame A1. The simulations are performed using sub-mechanism A (Table 6.4). The strain rate ϵ increases by increasing V_u while methane/air equivalence ratio remains constant. Figure 7.1 shows that the flame front is displaced by about 3.5 mm each time towards the wall with increasing ϵ. However the mole fractions of OH^*, CH^* and C_2^* do not exhibit significant difference with moderate changes of strain rate.

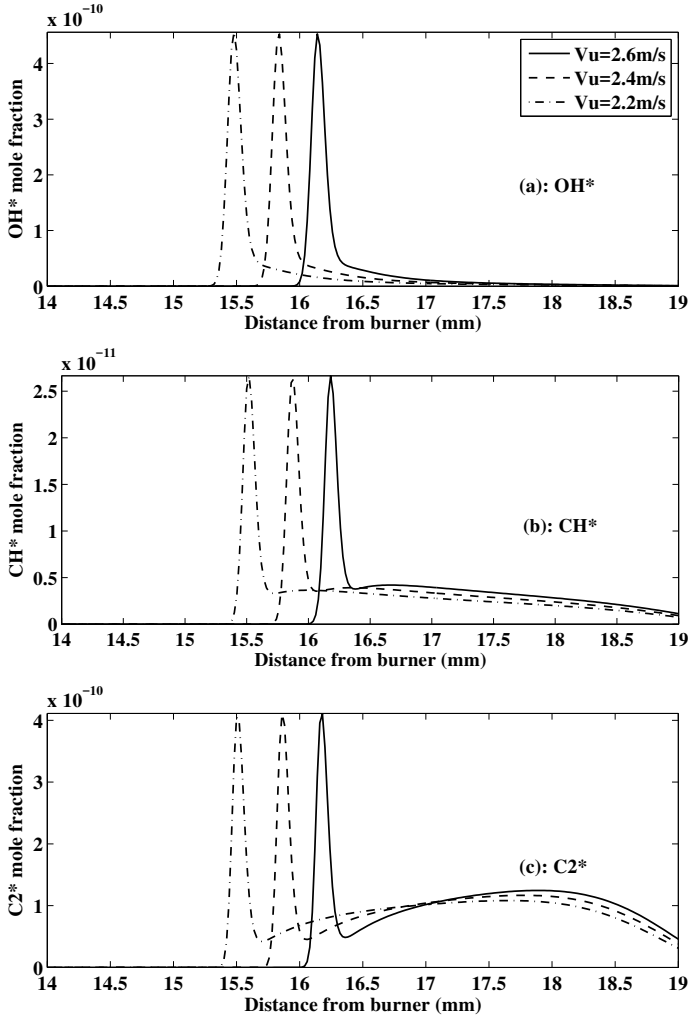

Figure 7.1: *OH^*, CH^* and C_2^* non-normalized numerical profiles for CH_4/coal/air flame A1, comparisons for different values of V_u = 2.6 m/s, 2.4 m/s and 2.2 m/s*

7.2 Influence of equivalence ratio

In this section, the influence of CH_4/O_2 equivalence ratio Φ (defined by Eq.2.2) with constant strain rate as shown in Table 3.1 is discussed. Experimental data and numerical profiles of OH^*, CH^* and C_2^* obtained by both sub-mechanisms mech A and K for CH_4/coal/air flames A1, A2, A3 and A4 (Φ = 0.88, 1.0, 1.12 and 1.2 respectively) are compared and shown in Fig.7.2 through Fig.7.5. All experimental profiles are normalized respectively by the maxima of OH^*, CH^* and C_2^* emission corresponding to CH_4/coal/air Flame A1 for spectroscopic measurements. All numerical profiles are normalized respectively by the maxima of OH^*, CH^* and C_2^* mole fractions calculated using mech A (Table 6.4) corresponding to CH_4/coal/air Flame A1.

The variation trends of all three species are well predicted by both sub-mechanisms, considering the very small concentrations of the measured species and the uncertainties in the excited radical kinetic modeling. The flame front position is also well predicted as a function of equivalence ratio. For flame A1 in Fig.7.2, there is significant effect from coal particles at the hot zone (between the flame front and the wall). However for flames A2, A3 and A4, the presence of coal particles results in richer flames. Therefore the emissions of CH^* and C_2^* are not as significant as for flame A1.

Considering the difference from two investigated sub-mechanisms, it mainly lies in the prediction of CH^* and C_2^* mole fractions. For a better understanding of the influence of Φ on CH_4/air and CH_4/coal/air flames, we first focus on the peak intensities (the maximum value of the chemiluminescence intensity), which have a further advantage in the better signal-to-noise ratio. Figure 7.6 shows the normalized OH^*, CH^* and C_2^* maximum chemiluminescent intensities at the flame front of CH_4/air and CH_4/coal/air flames A1, A2, A3 and A4 obtained by experiments and numerical simulations. Both OH^* and CH^* chemiluminescence are maximum near the stoichiometric conditions (Φ=1.0 for OH^* and Φ=1.12 for CH^*). However C_2^* chemiluminescent intensity increases monotonically from Φ=0.88 to Φ=1.2. These results agree qualitatively with experimental results of CH_4/air flames (Panoutsos et al. 2009; Liu et al. 2017) found in the literature.

The presence of coal particles shows insignificant influence on the OH^*, CH^* and C_2^* maximum chemiluminescent intensities at the flame front. In order to study the effect of coal particles in the hot zone, the experimental and numerical values at the middle position between the flame front and the wall are plotted in Fig.7.7 as a function of CH_4/air equivalence ratio. For CH_4/air flames, the CH^* and C_2^* chemiluminescent intensities are negligeable in the hot zone. However, for CH_4/coal/air flames, the CH^* and C_2^* intensities in the hot zone become less significant comparing with the peak value as the equivalence ratio increases. This is due to the fact that in rich flames such as A3 and A4, there is not enough oxygen left for the reaction with coal-related gaseous species.

Figure 7.8 shows the numerical C_2H_2 mole fraction profiles of CH_4/coal/air flames A1 to A4 calculated using mech A. The concentration of C_2H_2 in the burnt gases increases with the increase of equivalence ratio.

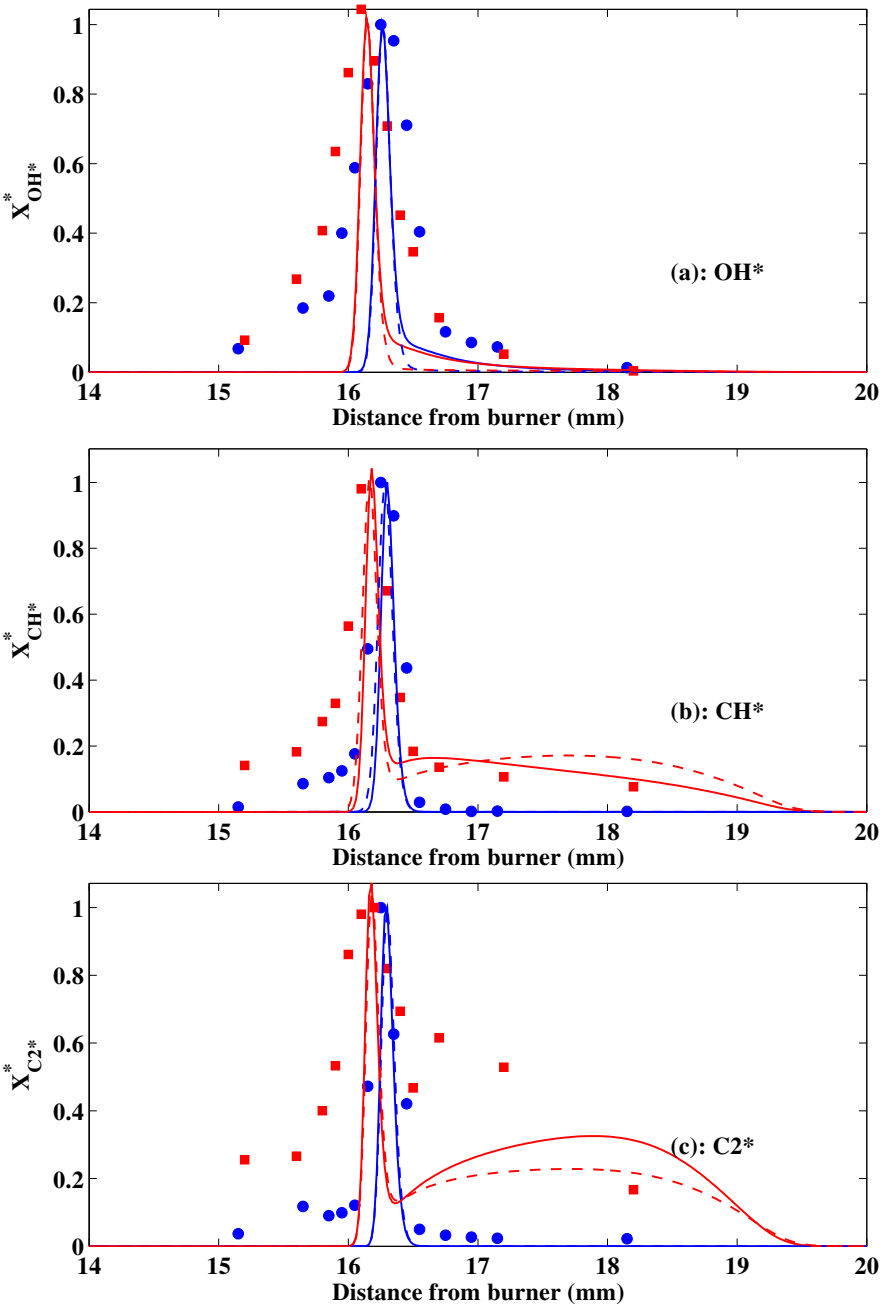

Figure 7.2: *Comparison of spectroscopy (symbols) and numerical (mech A: solid line, mech K: dashed line) profiles for CH_4/air (blue) and CH_4/coal/air (red) Flame A1 (Φ=0.88): (a) OH^*, (b) CH^*, (c) C_2^**

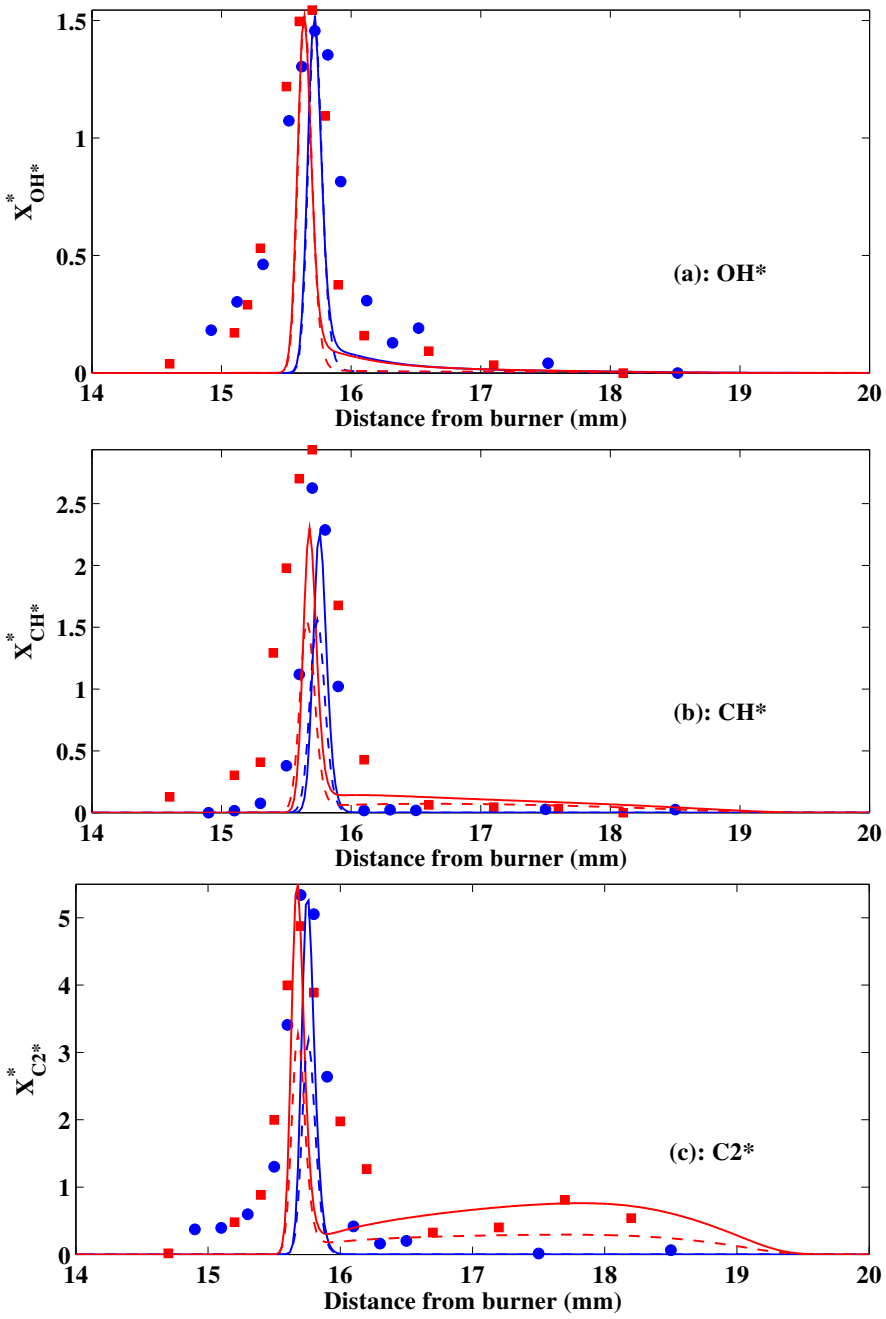

Figure 7.3: *Comparison of spectroscopy (symbols) and numerical (mech A: solid line, mech K: dashed line) profiles for CH_4/air (blue) and CH_4/coal/air (red) Flame A2 (Φ=1.0): (a) OH^*, (b) CH^*, (c) C_2^**

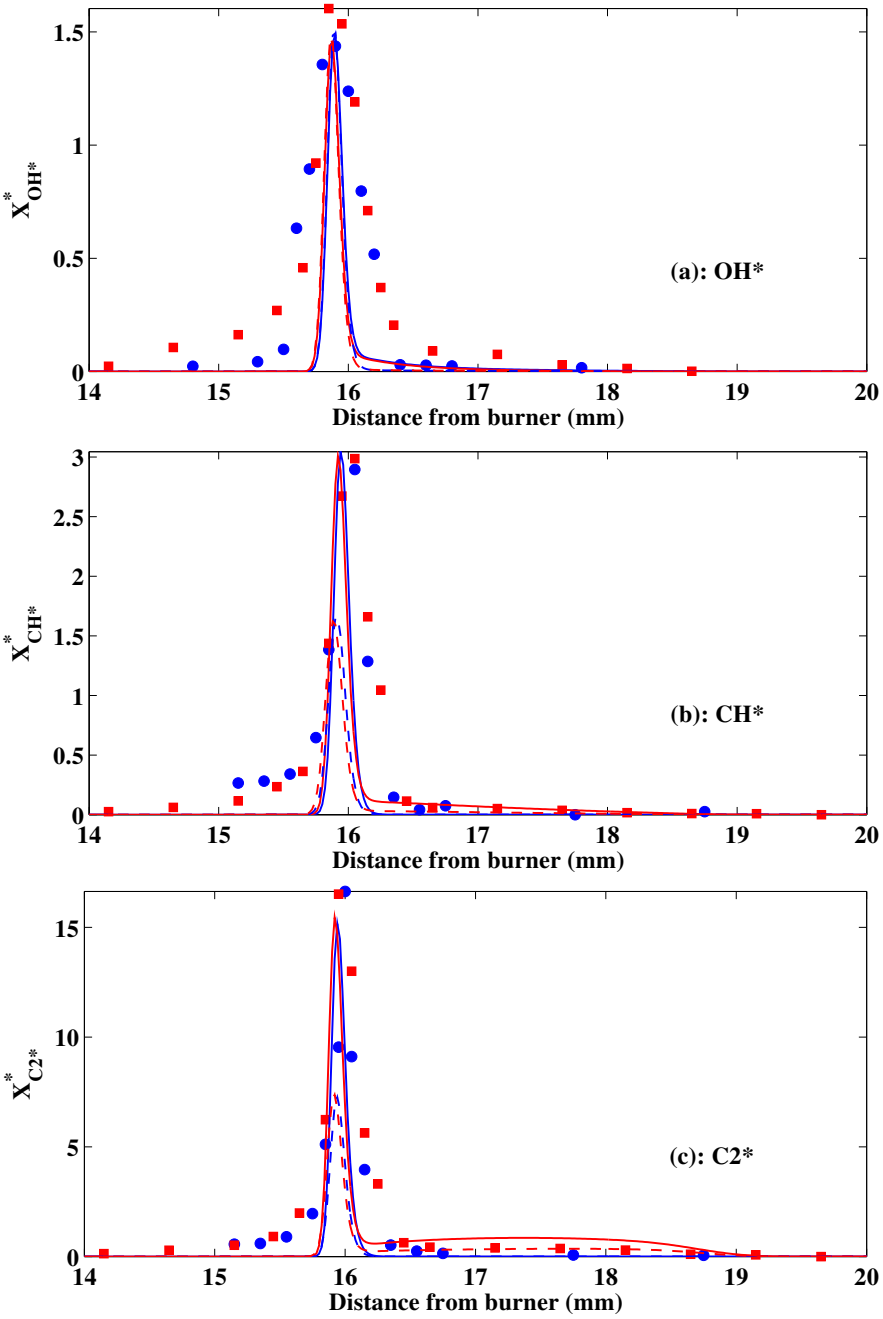

Figure 7.4: *Comparison of spectroscopy (symbols) and numerical (mech A: solid line, mech K: dashed line) profiles for CH_4/air (blue) and CH_4/coal/air (red) Flame A3 (Φ=1.12): (a) OH^*, (b) CH^*, (c) C_2^**

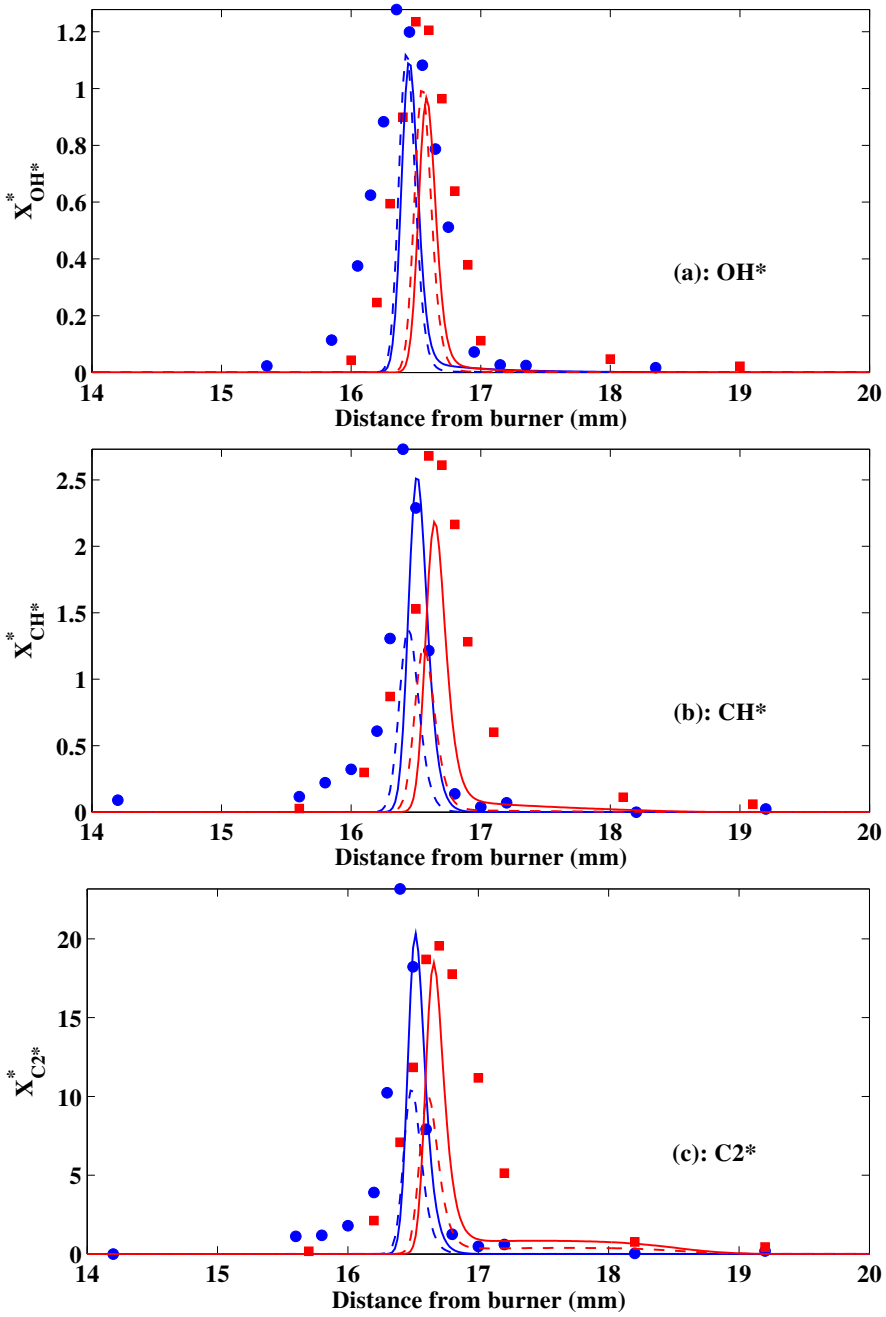

Figure 7.5: *Comparison of spectroscopy (symbols) and numerical (mech A: solid line, mech K: dashed line) profiles for CH_4/air (blue) and CH_4/coal/air (red) Flame A4 (Φ=1.2): (a) OH^*, (b) CH^*, (c) C_2^**

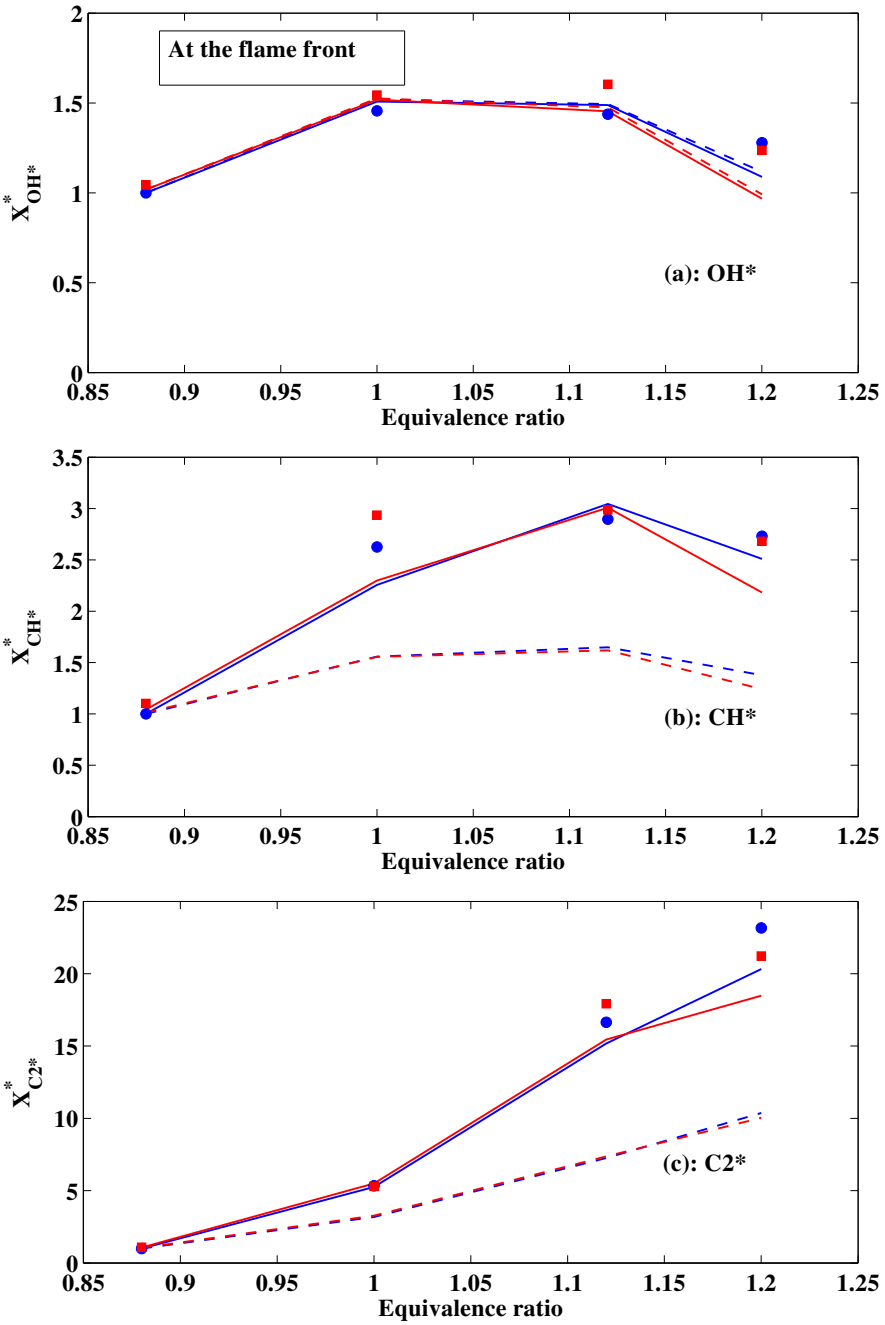

Figure 7.6: *Comparison of experimental (symbols) and numerical peak values (mech A: solid line, mech K: dashed line) of OH^*, CH^* and C_2^* as a function of equivalence ratio for CH_4/air flames (blue), CH_4/coal/air flames(red): (a) OH^*, (b) CH^*, (c) C_2^**

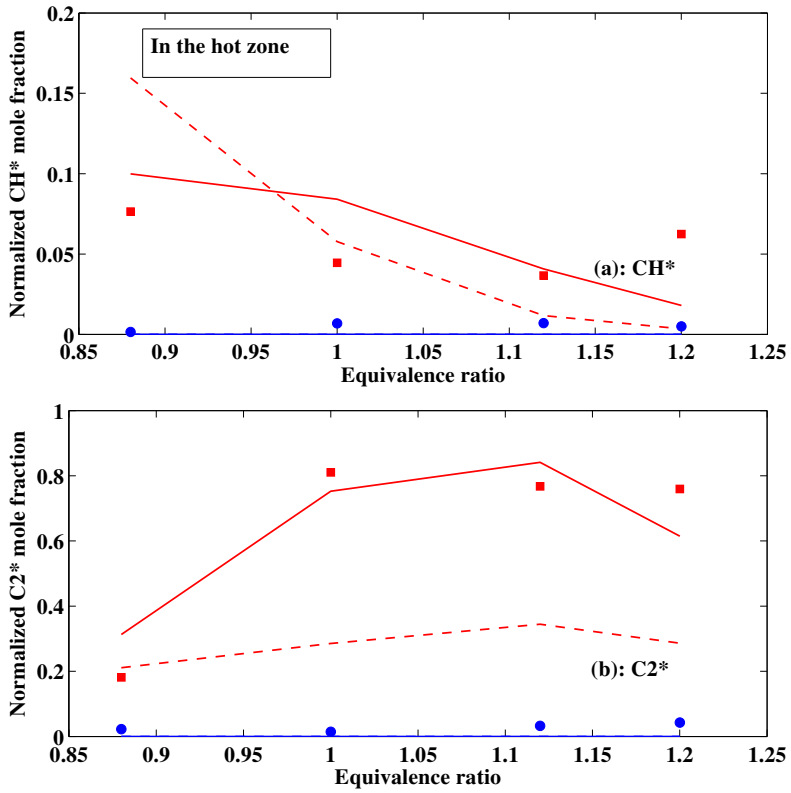

Figure 7.7: *Comparison of experimental (symbols) and numerical values (mech A: solid line, mech K: dashed line) of CH^* and C_2^* in the hot zone as a function of equivalence ratio for CH_4/air flames (blue), CH_4/coal/air flames (red): (a) CH^*, (b) C_2^**

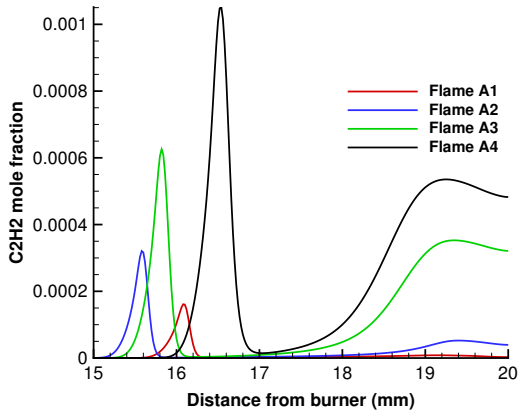

Figure 7.8: *Comparison of numerical C_2H_2 mole fraction (using mech A) in Flame A1 - A4*

Based on the analyses in Fig.7.6 and Fig.7.7, the mech A is able to better predict the peak value at the flame front position, both for CH_4/air and CH_4/coal/air flames.

7.3 Influence of oxygen enrichment

In this section, the influence of the oxygen mole fraction in the oxidizer stream is discussed. Figures 7.9 through 7.11 present OH^* and CH^* and C_2^* profiles respectively for three values of O_2 mole fraction 21%, 23% and 25% (flames A1, B1, and C1 from Table 3.2) for constant $\Phi = 0.88$. On each figure, $CH_4/O_2/N_2$ flame (blue) is compared to CH_4/coal/O_2/N_2 flame (red). Symbols correspond to experimental data obtained by spectroscopy. Two sub-mechanisms A and K are used for simulations: solid lines correspond to mech A and dashed lines to mech K.

The peak location of OH^* and CH^* and C_2^* measured in both $CH_4/O_2/N_2$ and CH_4/coal/O_2/N_2 flames are well retrieved by the simulations. The maximum gas temperature increases from 2030K to 2280K, while X_{O_2} in the oxidizer stream varies from 21% to 25%. Both chemiluminescence sub-mechanisms used in this study are able to well predict the chemiluminescence intensity when coal particles are added to the flame.

For a better understanding of the influence of oxygen enrichement, the peak values of each species are investigated. Figure 7.12 shows the normalized OH^*, CH^* and C_2^* maximum chemiluminescent intensities at the flame front of CH_4/air and CH_4/coal/air flames A1, B1 and C1 obtained by experiments and numerical simulations. The variation trends of all three species are well predicted by both sub-mechanisms, that is, the concentration increases with oxygen concentration, considering the very small concentration of the measured species and the uncertainties in the excited radical kinetic modeling. However only a fair agreement is achieved between calculated and measured chemiluminescence intensity ratios in terms of oxygen concentration variations. Both sub-mechanisms A and K overpredict the OH^* intensities for higher oxygen contents, while the mech K is able to better predict the CH^* and C_2^* maximum chemiluminescent intensities at the flame front, especially for the $CH_4/O_2/N_2$ flames. This may highlight the need to investigate the dependency of kinetic parameters under enriched air conditions.

In order to study the effect of coal particles in the hot zone, the experimental and numerical values of at the middle position between the flame front and the wall are plotted in Fig.7.13 as a function of oxygen mole fraction. In general, both mechanisms are able to predict the CH^* and C_2^* intensities caused by the presence of coal particles. However, discrepancy in the hot region between the predicted and measured intensities of coal/methane flames may be due to the

uncertainty of coal feeding rate.

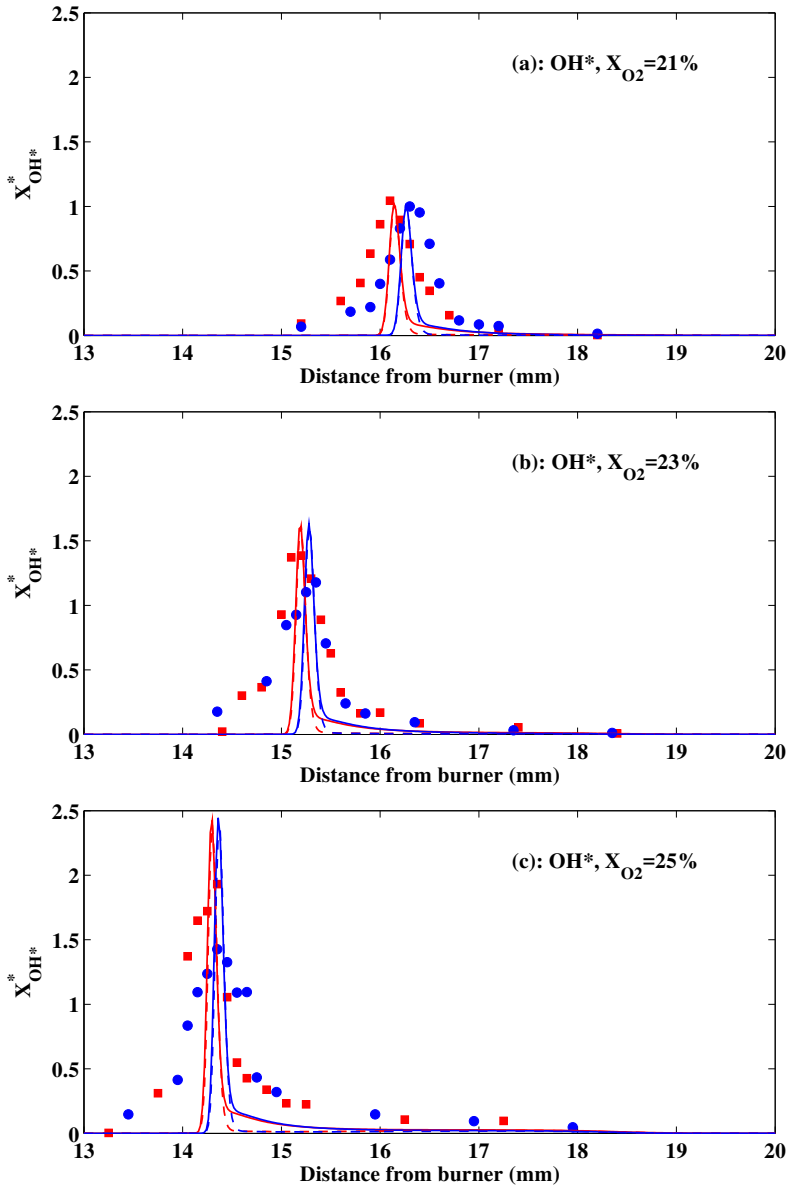

Figure 7.9: *Comparison of OH* spectroscopy (circle and square) and numerical (mech A: solid line, mech K: dashed line) profiles for $CH_4/O_2/N_2$ (blue) and $CH_4/coal/O_2/N_2$ (red) flames for different O_2 mole fractions: (a) Flame A1 X_{O_2}=21%, (b) Flame B1 X_{O_2}=23%, (c) Flame C1 X_{O_2}=25%*

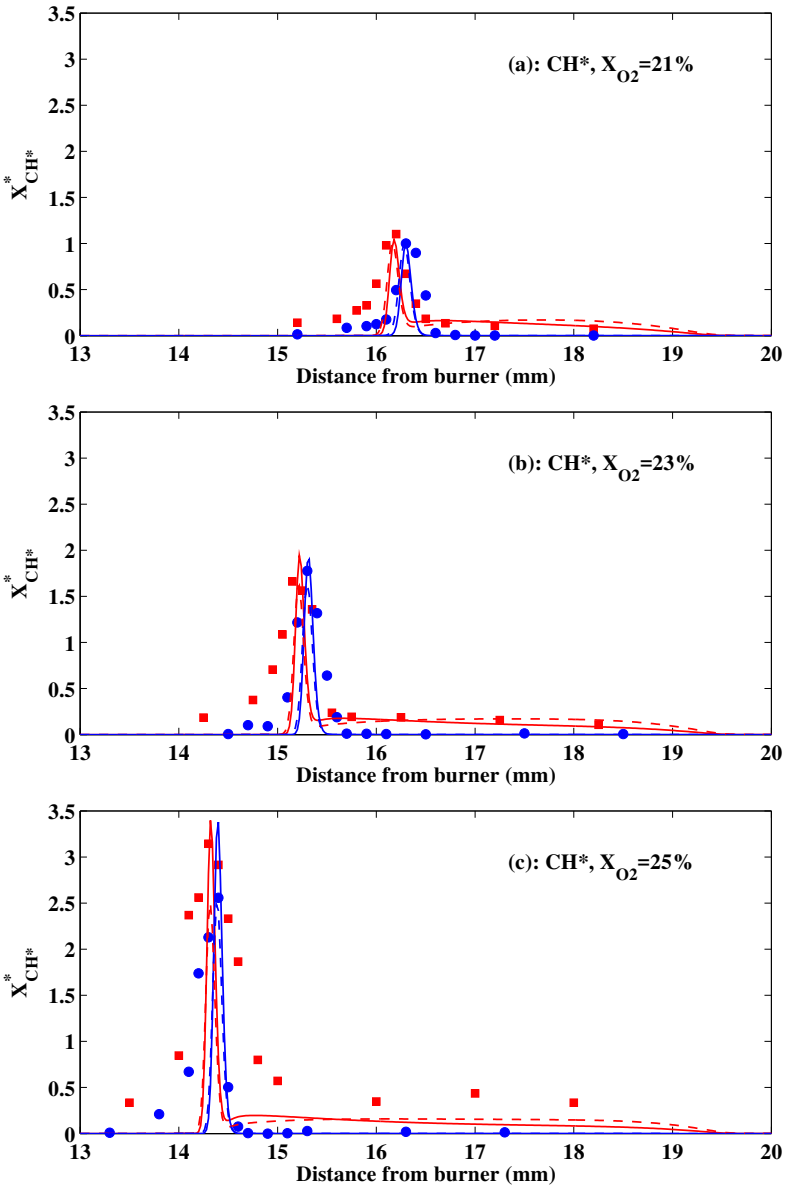

Figure 7.10: *Comparison of CH^* spectroscopy (circle and square) and numerical (mech A: solid line, mech K: dashed line) profiles for $CH_4/O_2/N_2$ (blue) and $CH_4/coal/O_2/N_2$ (red) flames for different O_2 mole fractions: (a) Flame A1, (b) Flame B1, (c) Flame C1*

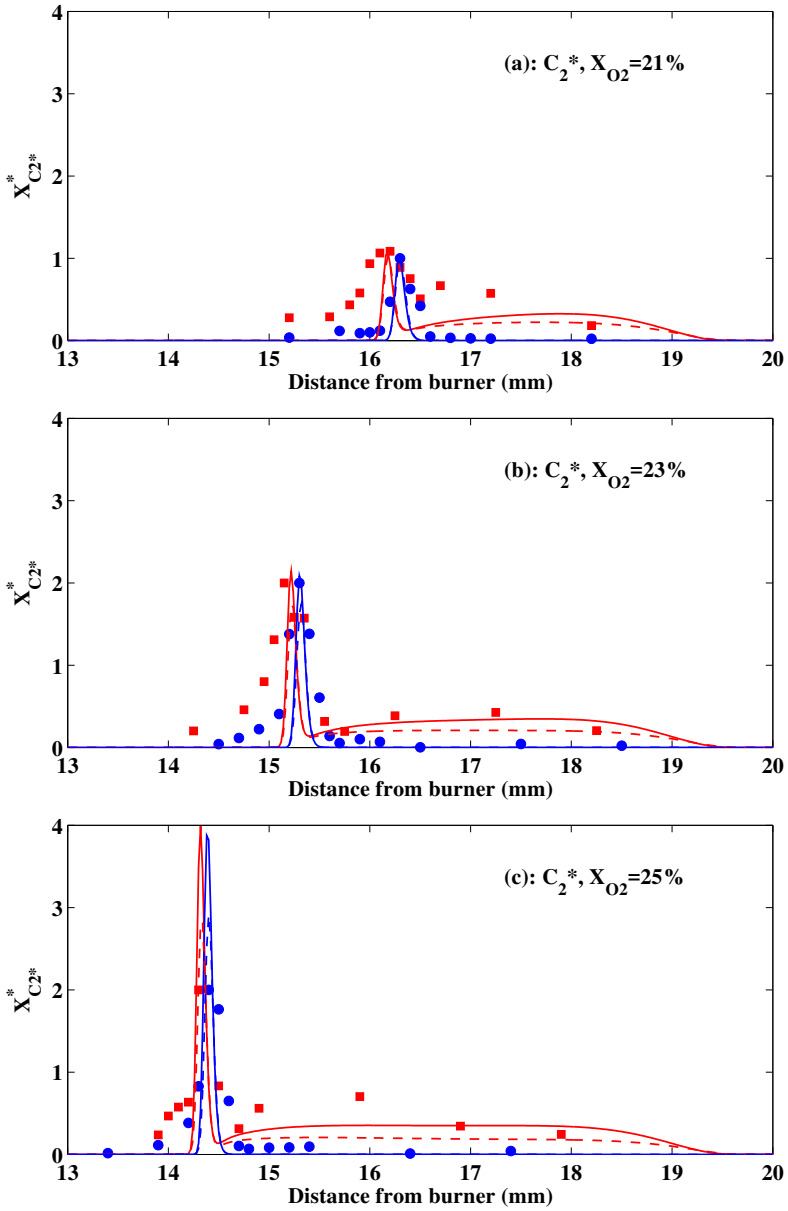

Figure 7.11: *Comparison of C_2^* spectroscopy (circle and square) and numerical (mech A: solid line, mech K: dashed line) profiles for $CH_4/O_2/N_2$ (blue) and $CH_4/coal/O_2/N_2$ (red) flames for different O_2 mole fractions: (a) Flame A1, (b) Flame B1, (c) Flame C1*

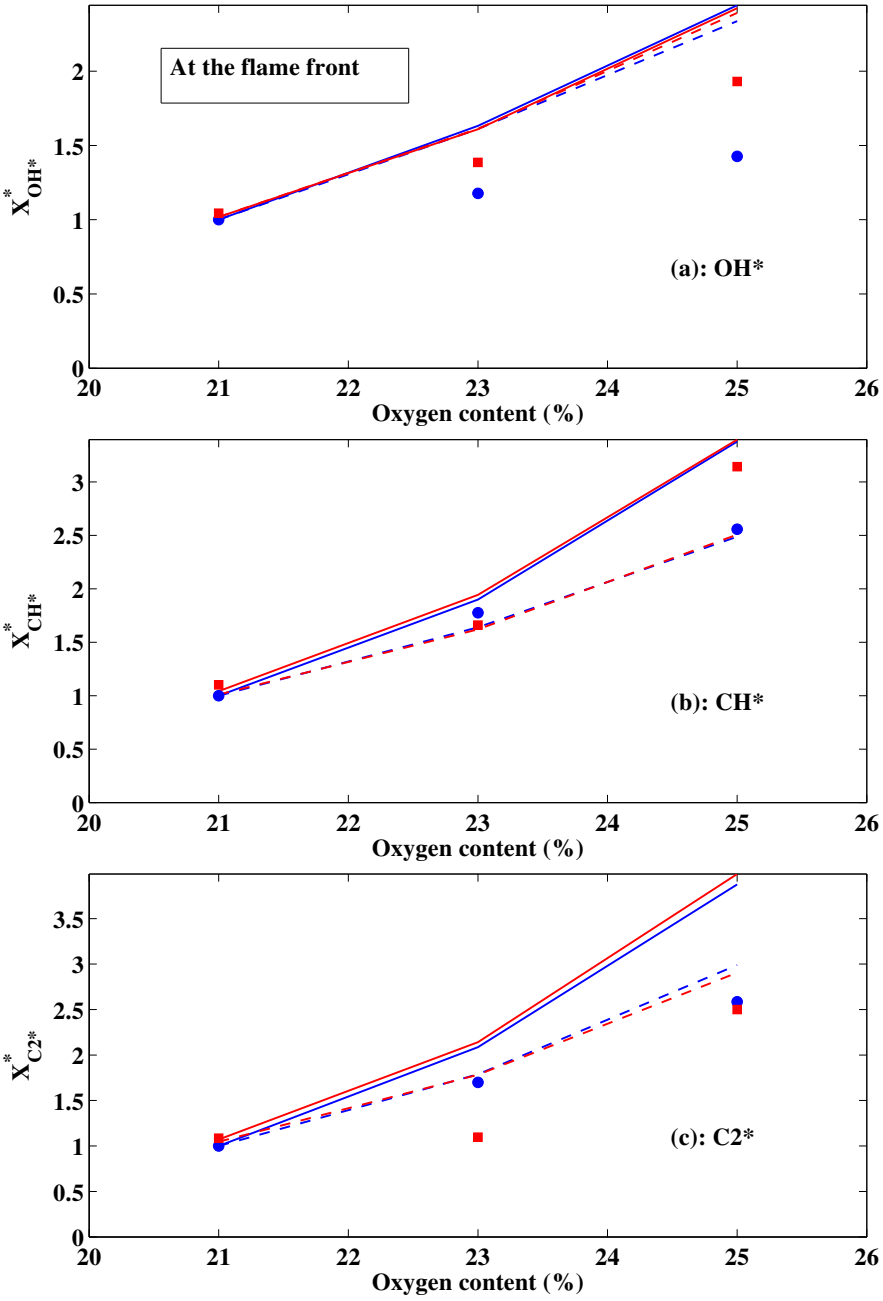

Figure 7.12: *Comparison of experimental (symbols) and numerical peak values (mech A: solid line, mech K: dashed line) of OH^*, CH^* and C_2^* as a function of O_2 mole fractions: CH_4/air flames (blue), CH_4/coal/air flames (red): (a) OH^*, (b) CH^*, (c) C_2^**

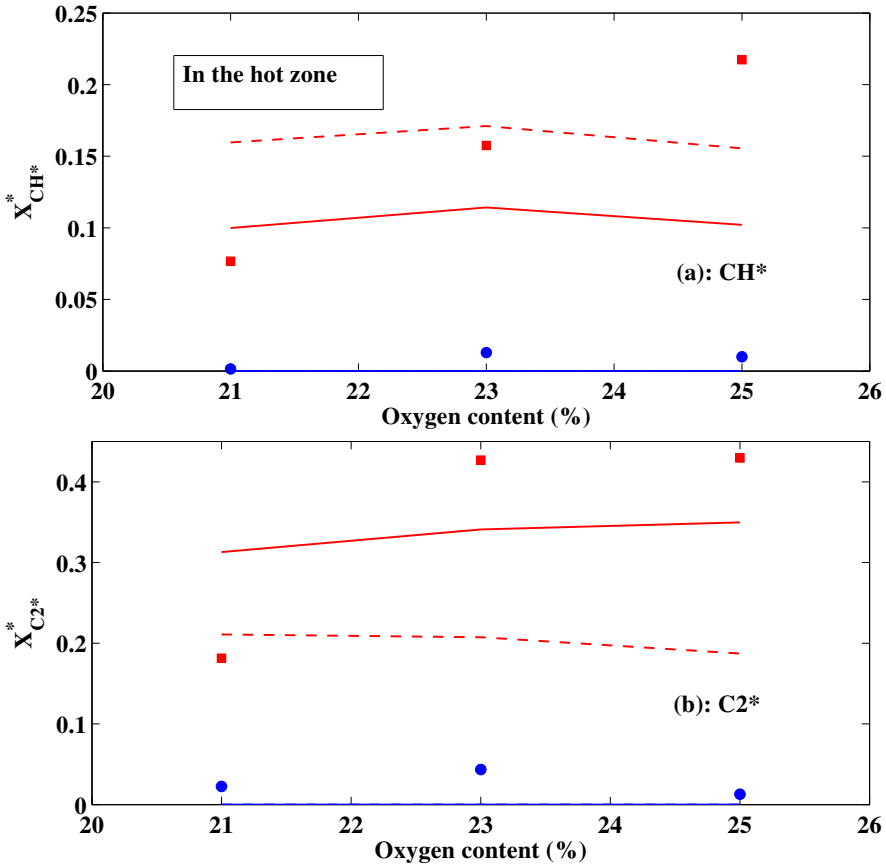

Figure 7.13: *Comparison of experimental (symbols) and numerical values (mech A: solid line, mech K: dashed line) of CH^* and C_2^* in the hot zone as a function of O_2 mole fractions: CH_4/air flames (blue), CH_4/coal/air flames (red): (a) CH^*, (b) C_2^**

7.4 Analysis of coal sub-models

The influence of TVM composition and coal combustion sub-models are explored in this section. Table 7.1 shows the different cases studied by numerical simulations. Case A1 corresponding to CH_4/coal/air flame from Table 3.1 is chosen as a reference case, all other cases differing by only one parameter from it. In this section, all the simulations are performed using mech A. Cases A1, A1c, A1d and A1e use the 1-step devolatilization model (Badzioch and Hawksley 1970), while case A1b uses the 2-step devolatilization model (Kobayashi et al. 1977). Cases A1, A1b, A1d and A1e employ the TVM composition of SB coal (Table 6.3). Case A1c corresponds to the TVM composition of MW coal (Table 6.3). In order to analyze the influence of unburned hydrocarbons present in the volatile matter on the flame structure, they are considered in case A1d as only CH_4 (55.34 %). Case A1e considers the oxidation product of

char as CO instead of CO_2 in cases A1 to A1d.

Case	Description	Devolatilization	TVM	Char oxidation
A1	Reference case (Table 3.1)	1-step	SB	CO_2
A1b	2-step devolatilization	2-step	SB	CO_2
A1c	TVM = MW compostion	1-step	MW	CO_2
A1d	TVM HC considered as CH_4 only	1-step	SB	CO_2
A1e	char + $O_2 \rightarrow$ CO (Eq. 5.17)	1-step	SB	CO

Table 7.1: *Variations in TVM composition and coal combustion sub-models for CH_4/coal/air flame A1*

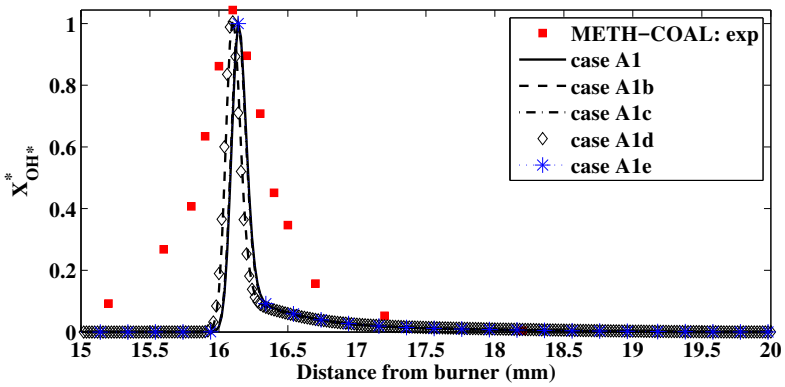

Figure 7.14: *Comparison of experimental and numerical OH^* mole fraction profiles in cases A1 to A1e*

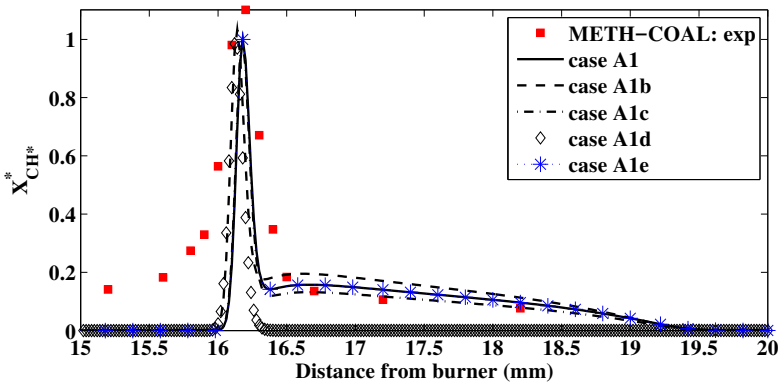

Figure 7.15: *Comparison of experimental and numerical CH^* mole fraction profiles in cases A1 to A1e*

Absolute non-normalized numerical profiles of OH^* mole fraction are shown in Fig.7.14. The flame front positions predicted by cases A1b to A1e match

the reference case A1. In general, the variation of TVM composition and coal devolatilization model show slight influence in the predicted OH^* concentration. However significant differences in the predicted CH^* and C_2^* mole fraction profiles are observed.

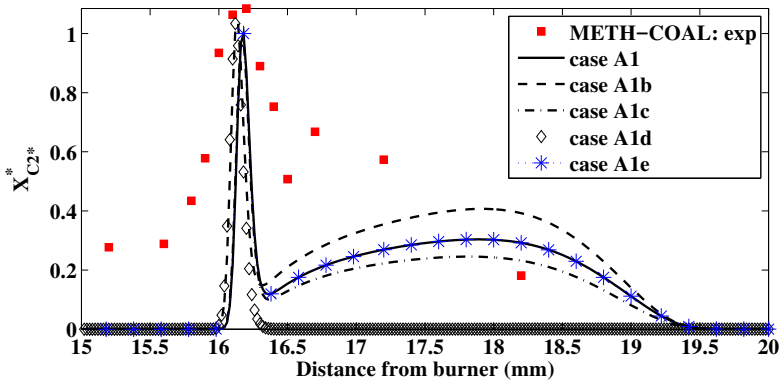

Figure 7.16: *Comparison of experimental and numerical C_2^* mole fraction profiles in cases A1 to A1e*

Absolute non-normalized numerical profiles of CH^* and C_2^* mole fraction predicted by the computation are presented in Figs 7.15 and 7.16, respectively. The peak location of CH^* and C_2^* are well retrieved by all simulated cases. Measurements in case METH-COAL A1 (Figs 7.10a and 7.11a) highlight a prolongation of the coal reaction zone in the burnt gases which is not observed in the methane flame. This effect is not observed in case A1d where the TVM unburned hydrocarbons are simplified as CH_4 only. The results obtained with MW coal in case A1c also show that the difference of TVM composition has a significant effect on the hot zone where coal pyrolysis products play an important role in the emission of CH^* and C_2^* radicals.

The comparison of case A1b with case A1 shows that the complexity of the devolatilization model will change the predicted CH^* and C_2^* mole fraction. However no definitive conclusions considering the "better" model can be drawn before more accurate measurements are available. The assumption of char oxidation product (case A1e) has little influence on the predicted CH^* and C_2^* mole fraction profiles. The reason may be the relative small conversion rate of char, considering the short residence time and moderate temperature of coal particles in the hot zone. Another possible variable is the oxygen content. In order to better understand the phenomenon of char oxidation, a numerical parametric study is performed in the following section.

Finally, formation of C_2H_2 and C_6H_6, involved in the soot formation process, are influenced by the coal devolatilization, as shown in Fig.7.17. In particular, the presence of heavy hydrocarbons (case A1d compared with A1) in the TVM

promotes the formation of soot precursors in the burnt gases, localized between the flame front and the wall.

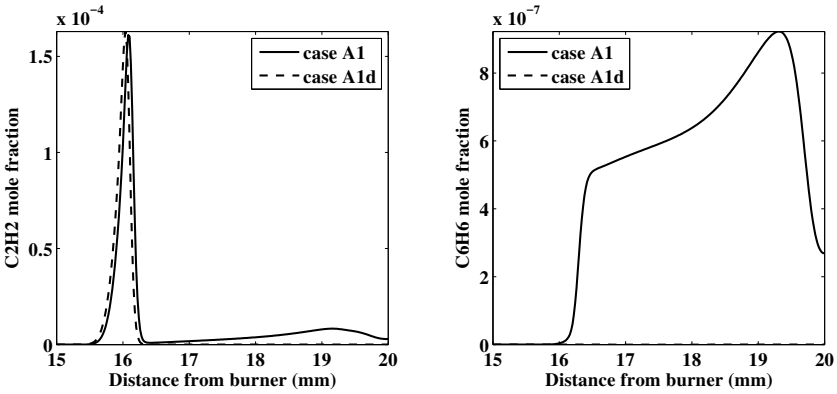

Figure 7.17: *Comparison of absolute numerical mole fraction profiles in cases A1 and A1d: (left) C_2H_2, (right) C_6H_6*

7.4.1 Numerical study of char oxidation

Due to the limitation of the experimental configuration, the oxygen mole fraction in the oxidizer stream does not go beyond 25%, while the injection velocity as well as the coal feeding rate are also limited with a small range. Numerical cases D1 and D1e are performed for a better understanding of the influence of oxygen enrichment on char oxidation reactions. In these cases, the equivalence ratio and injection velocity as well as the coal feeding rate are kept constant, while the O_2 mole fraction in the oxidizer stream is increase to 30%. Flame D1 considers full oxidation of char, while partial oxidation is used in flame D1e.

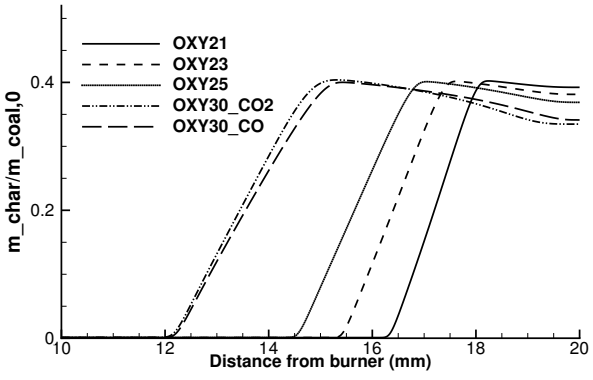

Figure 7.18: *Comparison of normalized char mass fraction of flame A1 (OXY21), flame A1 (OXY23), flame A1 (OXY25) , flame D1 (OXY30-CO2) and flame D1e (OXY30-CO)*

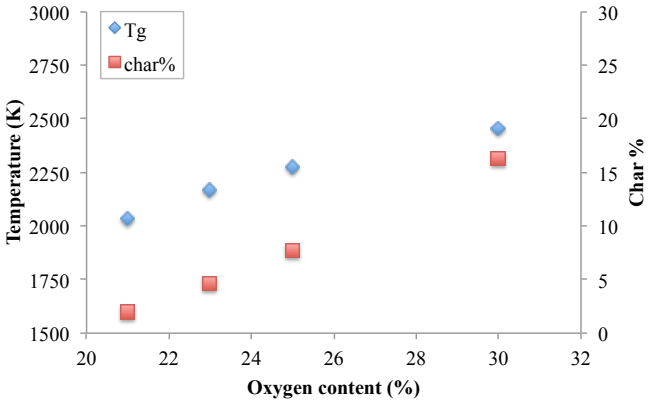

Figure 7.19: *Comparison of maximum gas temperature and char mass loss (%) as a function of oxygen content (%)*

In fig.7.18, normalized char mass fraction $\frac{m_{char}}{m_{coal,0}}$ is plotted for CH_4/coal/O_2/N_2 flames A1, B1, C1, D1 and D1e. Due to the oxidation process, the char mass fraction will decrease. With higher oxygen content, especially for flames D1 and D1e, the char burnout levels increase. The difference between the cases D1 and D1e comes from the fact that different values of heat of reaction are used in the oxidation calculations, therefore the particle temperature is different. However, this difference is relatively insignificant. In fig.7.19, the maximum gas temperature and the char mass loss $1 - m_{char}/m_{char,max}$ of flames A1, B1, C1 and D1 are plotted as a function of oxygen content. It is clear that the char burnout process is enhanced due to the higher oxygen content.

Summary of the chapter

The numerical simulations carried out on the coal devolatilization and oxidation in strained CH_4/O_2/N_2 flames are compared with experimental data. The results demonstrate good agreements between experimental and numerical predictions of OH^*, CH^* and C_2^* emissions. In particular, the influences of CH_4/O_2 equivalence ratio and O_2 mole fractions in the oxidizer stream are investigated. According to the comparisons, mech A is proved to be suitable for the predictions of CH_4/coal/O_2/N_2 flames, while the mech K, more detailed concerning C_2^* reactions, does not show more convincing results. In addition to validation with experiments, parametric studies by varying coal combustion sub-models as well as coal devolatilization products are performed. Analyses of the assumptions that are commonly used in PCC simulations are checked under the current configuration. Limited by the experimental configuration, char oxidation is investigated by numerical parametric studies of oxygen enrichment.

Conclusion

In the present work, the devolatilization and oxidation of pulverized coal particles in a strained flame configuration has been studied by both experimental and numerical approaches.

In Part I, the experimental approach was proposed. First, a review of the latest experimental studies of coal devolatilization and oxidation, especially the different measurement techniques and diagnostics commonly used in laboratory-scale experiments was presented. They have been grouped based on the target phenomena and the type of the reactor used. After comparing the advantages and limitations of those configurations, the premixed laminar strained flow configuration was chosen for our study. Then, the experimental configuration of the strained flames established by the flow of mono-disperse coal particles with a stream of $CH_4/O_2/N_2$ was presented. The description of the burner, the setup of positioning system as well as the coal feeding system were explained. Finally, different measurement techniques used in this work were outlined. In particular, we discussed two optical diagnostics used to investigate the flame structure and emission characteristics: measurements of OH^*, CH^*, and C_2^* spontaneous emission (ASE) and flame emission spectroscopy (FES). The experimental and post-processing procedures of each diagnostic were presented. The results from two diagnostics were compared for CH_4/air and CH_4/coal/air flames respectively.

In Part II, the numerical approach used to carry the simulations was presented. First the characterization of coal, the kinetics of devolatilization, volatile combustion and char combustion were reviewed. Commonly used coal sub-models and modeling assumptions were explained and were employed in the present work. Then the governing equations describing pulverized coal devolatilization and oxidation in strained $CH_4/O_2/N_2$ flames and the numerical simulation conditions along with coal sub-models and parameters were given. The same operating conditions studied experimentally were simulated. To enable the calculation of OH^*, CH^* and C_2^* radicals concentrations, the sub-mechanisms used by Alviso et al. (2015) and Kathrotia et al. (2012) have been also added to the USC-Mech II mechanism. These two mechanisms were validated by comparisons with experiments. The results showed that both mechanisms were able

to predict the OH^*, CH^* and C_2^* emission of CH_4/air and CH_4/coal/air flames, although differences in absolute values were observed. This modeling approach was further evaluated by the comparative study of experiments and simulations of different operating conditions. The results demonstrate good agreements between experimental and numerical prediction of OH^*, CH^* and C_2^* emission in terms of various CH_4/O_2 equivalence ratios and O_2 mole fractions in the oxidizer stream. Additional studies of coal combustion sub-models as well as coal devolatilization products were performed.

The following conclusions can be driven from the observations in both experimental and numerical studies:

- From the experimental point of view, the presence of pulverized coal particles in strained $CH_4/O_2/N_2$ flames added complexity to the physical phenomena of CH_4 combustion. First, noticeable differences of the flame front positions as well as increase of gas temperature have been observed due to the variation of local equivalence ratio and flame speed. Second, the comparisons between ASE and FES results were consistent at the fresh gas side. However in the burnt gases OH^* profiles from both methods are consistent but CH^* and C_2^* signals significantly differ. This can be explained that in this region the ASE signal is more important due to blackbody emission because it cannot be eliminated from the measurement. FES signal is possible with a correction of blackbody emission. Finally, the energy related to coal particles is small comparing with the total energy from methane combustion. Therefore, the influence from coal particles on the flame structure is less significant than expected. Numerical studies are needed to further investigate coal combustion propertities such as char oxidation.

- From the simulation point of view, both chemiluminescence sub-mechanisms used in this study were able to well predict the chemiluminescence intensity when coal particles are added to the flame. The variation trends were predicted by the simulations with different equivalence ratios and oxygen concentrations, considering the very small concentration of the measured species and the uncertainties in the excited radical kinetic modeling. Then, it can be seen from the discussions in Chapter 7 that the predicted results from the modeling approach differed significantly with changes to the coal sub-models and kinetic parameters. Especially, the devolatilization model and coal pyrolysis products seem to play more important roles. Comparison with experiments showed that the current numerical configuration was suitable for the prediction of OH^*, CH^* and C_2^* emission. However, it is difficult to reach definitive conclusion that which sub-model or set of parameters is better due to the limitation of experimental data. Finally, numerical simulations are used to investigated higher oxygen enrichment that experimental conditions do not al-

low. More parametric studies concerning char oxidation are needed for the current configuration.

Perspectives

The perspectives opened by this work concern both experimental procedure and numerical setup that are not realized or considered in the present study.

- **Experimental design**: More effort is needed to improve the current coal feeding system in order to reduce the uncertainty of coal mass flow rate measurements. Also, due to the difficulty of stabilization of the flat flame, the investigated range of CH_4/O_2 equivalence ratio as well as oxygen enrichment remained limited. More leaner $CH_4/O_2/N_2$ flames and higher O_2 mole fractions are expected to complement the experimental database, where more O_2 promotes the reaction of coal devolatilization and especially char oxidation reactions.
- **Experimental characterization**: There are still unclear points in the characterization of the current $CH_4/coal/O_2/N_2$ flames. These data are necessary for the validation of modeling, for example, measurements of particle temperature, evolution of particle size, concentration of burnt gases, analysis of coal ash, etc. Other diagnostic techniques such as LDA and LIF are expected to help better understand the physical phenomena involved in the combustion process.
- **Coal sub-models**: We have shown that the prediction of species concentration in $CH_4/coal/O_2/N_2$ flames depends greatly on the choice of coal-related sub-models and parameters. In particular, more detailed devolatilization models, such as the chemical percolation devolatilization (CPD) model, or well-validated model parameters for simple devolatilization models, are expected to give more reliable predictions.
- **Radiation Modeling**: Radiation models of solid phase have not been explored in detail in this work. However, radiation effect of coal particles is expected to be important when the particle number density increases. Moreover, in oxygen enriched combustion environments, the radiative heat transfer between coal particles and the gaseous phase is significant due to high temperature. Therefore, the implementation of high-fidelity radiation models will be of great interest.

Appendix A

Analysis reference values of Heizprofi lignite briquettes

Proximate analysis (annual average)		
Moisture	wt%	19.0
Ash	wt%	4.3
Fixed Carbon	wt%	50.6
Volatile Matter	wt%	45.1
Lower Calorific Value	MJ/kg	19.8
Ultimate analysis (annual average)		
Carbon	wt%	69.0
Hydrogen	wt%	5.0
Oxygen	wt%	24.7
Nitrogen	wt%	0.8
Sulfur	wt%	0.5
Analysis of oxides in ash on dry basis (annual average)		
SiO_2	wt%	4.0
Fe_2O_3	wt%	12.0
Al_2O_3	wt%	5.0
SO_3	wt%	20.0
CaO	wt%	36.0
MgO	wt%	16.0
Na_2O	wt%	6.0
K_2O	wt%	1.0

Table A.1: *Analysis reference values of Heizprofi lignite briquettes provided by the manufacturer*

Appendix B

Particle image velocimetry (PIV) of the current configuration

Particle image velocimetry (PIV) is an optical laser diagnostic that indirectly measures the gas flow velocity field through the reconstructed displacement of tracer particles in the flow.

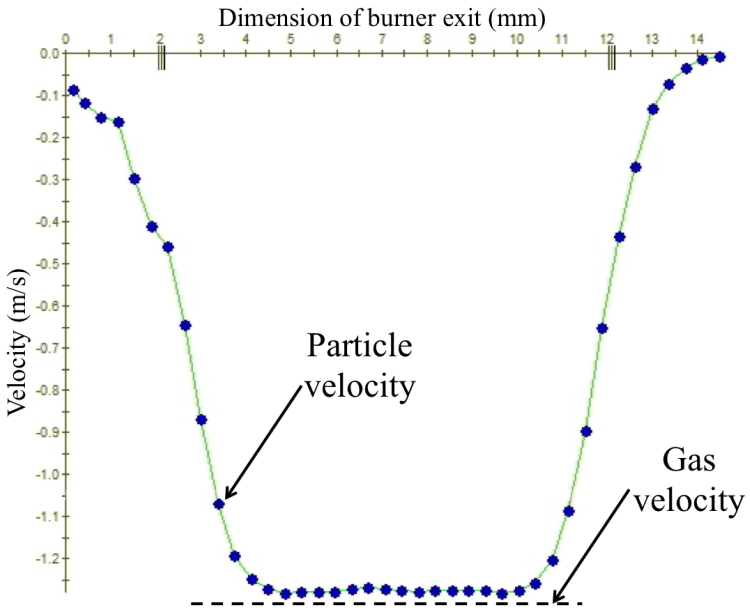

Figure B.1: *Typical PIV profiles at the burner exit*

PIV has been performed as a prelimenary study of the current strained CH_4/coal/air flame. A typical profile is presented in Figure B.1. The result shows that the particle average velocity matches the gas velocity at the injector exit. Therefore, the particles velocity is equal to the gas velocity, assumed as a boundary condition used in numerical simulations.

Appendix C

Reaction Kinetics of OH^*, CH^*, and C_2^* Chemiluminescence

Chemical reactions describing the production, quenching and chemiluminescence of OH^*, CH^* and C_2^* are added to the USC mechanism. Two sub-mechanisms found in literature are presented in Table C.1 and C.2. The units are *mol*, *cm*, *cal* and *s*.The first sub-mechanism has been validated by Alviso et al. (2015) for biodiesel fuels in a laminar counterflow spray configuration. The second one is recently developped by Kathrotia et al. (2012) which includes more elementary reactions such as C_3 species. It is used by Liu et al. (2017) for the validation with methane flames.

The reactions for each radical (OH^*, CH^* and C_2^*) are presented separately. In Table C.1 (mech A), for example, the reactions for the production and destruction of OH^* radical are presented in R1-R10. Those of CH^* radical are presented by R11-R22. R22-R26 correspond to the formation and destruction reactions of species C and C_2, which is necessary because C and C_2 are invloved in the formation of CH^* radical via the C_2H species. Here, no quenching reactions is considered for C_2 radical therefore the mole fraction of C_2 is used to present C_2^* radical. This assumption is validated by mech K, where the calculated C_2^* mole fraction equals to that of C_2.

#	Reactions	A	n	E
R1	$CH + O_2 \Leftrightarrow OH^* + CO$	1.80×10^{11}	0	0
R2	$O + H + M \Leftrightarrow OH^* + M$	3.63×10^{13}	0	0
R3	$OH^* \Rightarrow OH + h\nu$	1.45×10^{6}	0	0
R4	$OH^* + N_2 \Leftrightarrow OH + N_2$	1.08×10^{11}	0.5	-1238
R5	$OH^* + O_2 \Leftrightarrow OH + O_2$	2.10×10^{12}	0.5	-482
R6	$OH^* + H_2O \Leftrightarrow OH + H_2O$	5.92×10^{12}	0.5	-861
R7	$OH^* + H_2 \Leftrightarrow OH + H_2$	2.95×10^{12}	0.5	-444
R8	$OH^* + CO_2 \Leftrightarrow OH + CO_2$	2.75×10^{12}	0.5	-968
R9	$OH^* + CO \Leftrightarrow OH + CO$	3.23×10^{12}	0.5	-787
R10	$OH^* + CH_4 \Leftrightarrow OH + CH_4$	3.36×10^{12}	0.5	-635
R11	$C_2H + O \Leftrightarrow CH^* + CO$	6.20×10^{12}	0	0
R12	$C + H + M \Leftrightarrow CH^* + M$	3.63×10^{13}	0	0
R13	$CH^* \Rightarrow CH + h\nu$	1.86×10^{6}	0	0
R14	$CH^* + N_2 \Leftrightarrow CH + N_2$	3.03×10^{2}	3.40	-381
R15	$CH^* + O_2 \Leftrightarrow CH + O_2$	2.48×10^{6}	2.14	-1720
R16	$CH^* + H_2O \Leftrightarrow CH + H_2O$	5.30×10^{13}	0	0
R17	$CH^* + H_2 \Leftrightarrow CH + H_2$	1.47×10^{14}	0	1361
R18	$CH^* + CO_2 \Leftrightarrow CH + CO_2$	2.41×10^{-1}	4.30	-1694
R19	$CH^* + CO \Leftrightarrow CH + CO$	2.44×10^{12}	0.50	0
R20	$CH^* + CH_4 \Leftrightarrow CH + CH_4$	1.73×10^{13}	0	167
R21	$C_2 + H_2 \Leftrightarrow C_2H + H$	4.00×10^{5}	2.40	1000
R22	$CH + CH \Leftrightarrow C_2 + H_2$	5.00×10^{12}	0	0
R23	$C + C + M \Leftrightarrow C_2 + M$	3.00×10^{14}	0	-1000
R24	$C + CH \Leftrightarrow C_2 + H$	5.00×10^{13}	0	0
R25	$O + C_2 \Leftrightarrow C + CO$	5.00×10^{13}	0	0
R26	$C_2 + O_2 \Leftrightarrow CO + CO$	9.00×10^{12}	0	980

Table C.1: *Mech A: OH^*, CH^* and C_2 formation, chemiluminescence and quenching reactions from Alviso et al. (2015); Panoutsos et al. (2009)*

#	Reactions	A	n	E
R1	$H + O + M \Leftrightarrow OH^* + M$	1.50×10^{13}	0	5975
R2	$CH + O_2 \Leftrightarrow OH^* + CO$	1.80×10^{11}	0	0
R3	$OH^* \Leftrightarrow OH$	1.45×10^{6}	0	0
R4	$OH^* + O_2 \Leftrightarrow OH + O_2$	2.10×10^{12}	0.5	-482
R5	$OH^* + H_2O \Leftrightarrow OH + H_2O$	5.93×10^{12}	0.5	-861
R6	$OH^* + H_2 \Leftrightarrow OH + H_2$	2.95×10^{12}	0.5	-444
R7	$OH^* + CO_2 \Leftrightarrow OH + CO_2$	2.76×10^{12}	0.5	-968
R8	$OH^* + CO \Leftrightarrow OH + CO$	3.23×10^{12}	0.5	-787
R9	$OH^* + CH_4 \Leftrightarrow OH + CH_4$	3.36×10^{12}	0.5	-635
R10	$OH^* + OH \Leftrightarrow OH + OH$	6.01×10^{12}	0.5	-762
R11	$OH^* + H \Leftrightarrow OH + H$	1.31×10^{13}	0.5	-167
R12	$OH^* + Ar \Leftrightarrow OH + Ar$	1.69×10^{12}	0	4137
R13	$C_2H + O_2 \Leftrightarrow CH(A) + CO_2$	3.20×10^{11}	0	1600
R14	$C_2H + O \Leftrightarrow CH(A) + CO$	2.50×10^{12}	0	0
R15	$C_2 + OH \Leftrightarrow CH(A) + CO$	1.11×10^{13}	0	0
R16	$C + H + M \Leftrightarrow CH(A) + M$	3.63×10^{13}	0	0
R17	$CH(A) \Leftrightarrow CH$	1.86×10^{6}	0	0
R18	$CH(A) + O_2 \Leftrightarrow CH + O_2$	2.48×10^{6}	2.14	-1720
R19	$CH(A) + CO_2 \Leftrightarrow CH + CO_2$	2.41×10^{-1}	4.3	-1696
R20	$CH(A) + CO \Leftrightarrow CH + CO$	2.44×10^{12}	0.5	0
R21	$CH(A) + CH_4 \Leftrightarrow CH + CH_4$	1.73×10^{13}	0	167
R22	$CH(A) + H_2O \Leftrightarrow CH + H_2O$	5.30×10^{13}	0	0
R23	$CH(A) + H \Leftrightarrow CH + H$	2.01×10^{14}	0	1362
R24	$CH(A) + OH \Leftrightarrow CH + OH$	7.13×10^{13}	0	1362
R25	$CH(A) + H_2 \Leftrightarrow CH + H_2$	1.47×10^{14}	0.5	1362
R26	$CH(A) + Ar \Leftrightarrow CH + Ar$	3.13×10^{11}	0	0
R27	$C_2H + O_2 \Leftrightarrow CH(B) + CO_2$	4.27×10^{10}	0	1600
R28	$C_2H + O \Leftrightarrow CH(B) + CO$	3.33×10^{11}	0	0
R29	$C_2 + OH \Leftrightarrow CH(B) + CO$	1.48×10^{12}	0	0
R30	$C + H + M \Leftrightarrow CH(B) + M$	4.84×10^{12}	0	0
R31	$CH(B) \Leftrightarrow CH$	2.50×10^{6}	0	0
R32	$CH(B) + O_2 \Leftrightarrow CH + O_2$	3.90×10^{13}	0	0
R33	$CH(B) + CO_2 \Leftrightarrow CH + CO_2$	4.00×10^{13}	0	0
R34	$CH(B) + CO \Leftrightarrow CH + CO$	2.44×10^{12}	0	0
R35	$CH(B) + CH_4 \Leftrightarrow CH + CH_4$	1.65×10^{13}	0	0
R36	$CH(B) + H_2O \Leftrightarrow CH + H_2O$	5.30×10^{13}	0	0
R37	$CH(B) + H \Leftrightarrow CH + H$	2.01×10^{14}	0	1362
R38	$CH(B) + OH \Leftrightarrow CH + OH$	7.13×10^{13}	0	1362
R39	$CH(B) + H_2 \Leftrightarrow CH + H_2$	1.47×10^{14}	0.5	1362
R40	$CH(B) + Ar \Leftrightarrow CH + Ar$	6.60×10^{11}	0	0
R41	$CH(B) \Leftrightarrow CH(A)$	5.00×10^{7}	0	0

R42	$CH_2 + C \Leftrightarrow C_2^* + H_2$	2.40×10^{12}	0	0
R43	$C_3 + O \Leftrightarrow C_2^* + CO$	4.22×10^{12}	0	0
R44	$C_2^* \Leftrightarrow C_2$	1.00×10^{7}	0	0
R45	$C_2^* + M \Leftrightarrow C_2 + M$	4.80×10^{13}	0	0
R46	$C + H_2O \Leftrightarrow HCO + H$	3.00×10^{12}	0	0
R47	$C + OH \Leftrightarrow H + CO$	5.00×10^{13}	0	0
R48	$C + OH \Leftrightarrow CH + O$	2.40×10^{14}	0	21735
R49	$C + CH \Leftrightarrow C_2 + H$	1.00×10^{13}	0	0
R50	$C + CH_2 \Leftrightarrow C_2 + H_2$	3.00×10^{12}	0	0
R51	$C_2H + O \Leftrightarrow C_2 + OH$	1.20×10^{13}	0	0
R52	$C_2H + H \Leftrightarrow C_2 + H_2$	6.20×10^{13}	0	17436
R53	$C_2 + OH \Leftrightarrow C_2O + H$	5.00×10^{13}	0	0
R54	$C_2 + O_2 \Leftrightarrow CO + CO$	9.00×10^{12}	0	979
R55	$C_2 + O \Leftrightarrow CO + C$	1.00×10^{14}	0	0
R56	$C_2 + OH \Leftrightarrow CH + CO$	5.00×10^{13}	0	0
R57	$C_2 + CH_4 \Leftrightarrow C_2H + CH3$	3.00×10^{13}	0	590
R58	$C_2 + C_2H_2 \Leftrightarrow C_2H + C_2H$	1.00×10^{14}	0	0
R59	$C_2 + C_2H_4 \Leftrightarrow C_2H + C_2H3$	1.00×10^{14}	0	0
R60	$C_2 + C_2H6 \Leftrightarrow C_2H + C_2H5$	5.00×10^{13}	0	0
R61	$C_2 + O_2 \Leftrightarrow C_2O + O$	2.00×10^{14}	0	8073
R62	$CH + CO \Leftrightarrow C_2O + H$	1.90×10^{11}	0	0
R63	$C_2O + O \Leftrightarrow CO + CO$	4.80×10^{13}	0	0
R64	$C_2O + OH \Leftrightarrow CH + CO_2$	2.00×10^{13}	0	0
R65	$C + C_2H \Leftrightarrow C_3 + H$	2.00×10^{16}	-1.0	0
R66	$C_2 + CH \Leftrightarrow C_3 + H$	5.00×10^{13}	0	0
R67	$C_3 + OH \Leftrightarrow CO + C_2H$	8.00×10^{13}	0	0
R68	$C_3 + O_2 \Leftrightarrow CO_2 + C_2$	9.00×10^{11}	0	21855
R69	$C_3 + O \Leftrightarrow CO + C_2$	5.00×10^{13}	0	0
R70	$CH + C_2H_2 \Leftrightarrow C_3H_2 + H$	9.40×10^{13}	0	-500
R71	$C_3H + H_2 \Leftrightarrow C_3H_2 + H$	4.00×10^{5}	2.4	1003
R72	$C_3H_2 + O \Leftrightarrow HCO + C_2H$	4.00×10^{13}	0	0
R73	$C_3H_2 + OH \Leftrightarrow HCO + C_2H_2$	1.00×10^{13}	0	0
R74	$C_3 + H_2 \Leftrightarrow C_3H + H$	4.10×10^{5}	2.4	21974
R75	$CH + C_2H \Leftrightarrow C_3H + H$	5.00×10^{13}	0	0
R76	$C_3H + O \Leftrightarrow CO + C_2H$	4.00×10^{13}	0	0
R77	$C_3H + OH \Leftrightarrow CO + C_2H_2$	2.00×10^{13}	0	0
R78	$C_3H + O_2 \Leftrightarrow CO + HCCO$	3.00×10^{13}	0	0

Table C.2: *Mech K: OH^*, CH^* and C_2^* formation, chemiluminescence and quenching reactions from Kathrotia et al. (2012)*

Appendix D

Radiative heat transfer of gaseous phase

D.1 Radiative Transfer Equation(RTE)

The intensity field inside a medium is governed by the radiative transfer equation (RTE). For a medium that emits, absorbs, and/or scatters radiation,

$$dL'_\nu = (dL'_\nu)_{abs} + (dL'_\nu)_{em} + (dL'_\nu)^{out}_{sca} + (dL'_\nu)^{in}_{sca} \tag{D.1}$$

where L'_ν the radiative intensity for wave number ν can be written by the influence of absorption, emission, and scattering.

D.1.1 Absorption

$$(dL'_\nu)_{abs} = -\kappa_\nu L'_\nu ds \tag{D.2}$$

where the constant κ_ν is the absorption coefficient. Integration of equation (D.2) over the geometric path $\widehat{s}$ results in

$$L'_\nu = L'_\nu(0)\exp(-\int_0^s \kappa_\nu ds) = L'_\nu(0)\tau_\nu \tag{D.3}$$

The transmissivity τ_ν between the abscissas s and s' and absorptivity α_ν is defined as

$$\tau_\nu(s,s') = 1-\alpha_\nu = \exp(-\int_s^{s'} \kappa_\nu(s'')ds'') \tag{D.4}$$

D.1.2 Emission

$$(dL'_\nu)_{em} = \kappa_\nu L^0_\nu(T)ds \tag{D.5}$$

where $L^0_\nu(T)$ is the blackbody intensity at local equilibrium. The emissivity ϵ_ν is defined as

$$\epsilon_\nu \;=\; 1-\tau_\nu \;=\; 1-\exp(-\int_s^{s'}\kappa_\nu(s'')ds'') \tag{D.6}$$

And $\epsilon_\nu = \alpha_\nu$ as is the case with surface radiation.

D.1.3 Scattering

The attenuation by scattering, or "out-scattering"

$$(dL'_\nu)^{out}_{sca} \;=\; -\sigma_\nu L'_\nu ds \tag{D.7}$$

where σ_ν is the scattering coefficient.
And augmentation due to scattering, or "in-scattering"

$$(dL'_\nu)^{in}_{sca} \;=\; ds\frac{\sigma_\nu}{4\pi}\int_0^{4\pi} p_\nu(\mathbf{u}',\mathbf{u})L'_\nu d\Omega \tag{D.8}$$

where p_ν is the scattering phase function.

From equations (D.2), (D.5), (D.7), and (D.8)

$$\frac{d}{ds}\left[L'_\nu\big(\mathbf{u}(s),s\big)\right] \;=\; -(\kappa_\nu+\sigma_\nu)L'_\nu(\mathbf{u}(s),s)+\kappa_\nu(\mathbf{u},s)L^0_\nu(T)+\frac{\sigma_\nu}{4\pi}\int_0^{4\pi} p_\nu(\mathbf{u}',\mathbf{u},s)L'_\nu(\mathbf{u}',s)d\Omega \tag{D.9}$$

By introducing an extinction coefficient is defined as $\beta_\nu = \kappa_\nu + \sigma_\nu$, the RTE is rewritten in the form

$$\frac{d}{ds}L'_\nu + \beta_\nu L'_\nu \;=\; S_\nu \tag{D.10}$$

with the source term S_ν

$$S_\nu(\mathbf{u},s) \;=\; \kappa_\nu(s)L^0_\nu[T(s)] + \frac{\sigma_\nu(s)}{4\pi}\int_0^{4\pi} p_\nu(\mathbf{u}'\to\mathbf{u},s)L'_\nu(\mathbf{u}',s)d\Omega' \tag{D.11}$$

If the source term S_ν is assumed known, the equation(D.10) has a solution under the form Taine et al. (2014):

$$L'_\nu(\mathbf{u},s) \;=\; L'_\nu(\mathbf{u}_0,0)\exp[-\int_0^s \beta_\nu(s')ds'] + \int_0^s S_\nu(\mathbf{u},s')\exp[-\int_{s'}^s \beta_\nu(s'')ds'']ds' \tag{D.12}$$

Introducing the transmissivity from s' to s

$$\tau'_{\nu,s'\to s} \;=\; \exp[-\int_{s'}^s \beta_\nu(s'')ds''] \tag{D.13}$$

Equation(D.12) becomes

$$L'_\nu(\mathbf{u},s) \;=\; L'_\nu(\mathbf{u}_0,0)\tau'_{\nu,0\to s} + \int_0^s S_\nu(\mathbf{u},s')\beta_\nu^{-1}(s')\frac{\partial}{\partial s'}\tau'_{\nu,s'\to s}ds' \tag{D.14}$$

Neglecting the scattering effect: $\sigma_\nu = 0$, therefore $\beta_\nu = \kappa_\nu$

$$L'_\nu(\mathbf{u},s) \;=\; L'_\nu(\mathbf{u}_0,0)\tau'_{\nu,0\to s} + \int_0^s L^0_\nu[T(s')]\frac{\partial\tau'_{\nu,s'\to s}}{\partial s'}ds' \tag{D.15}$$

Rewrite in the discret form with index j, length l_j and absorption coefficient $\kappa_{\nu,j}$ for N_c elements

$$L'_\nu(\mathbf{u},N_c) \;=\; L'_\nu(\mathbf{u}_0,0)\tau'_{\nu,0\to N_c} + \sum_{j=1}^{N_c} L^0_\nu(T_j)(\tau'_{\nu,j\to N_c} - \tau'_{\nu,j-1\to N_c}) \tag{D.16}$$

with

$$\tau'_{\nu,j\to N_c} \;=\; \exp(-\sum_{j'=j+1}^{N_c}\kappa_{\nu,j'}l_{j'}) \tag{D.17}$$

D.2 General equation for radiative power

The radiative power $P^R(\mathbf{r},t)$ at point $\mathbf{r}$ is calculated by the divergence of the spectral radiative flux $\mathbf{q}^R$.

$$\mathbf{q}^R \;=\; \int_0^\infty d\nu \int^{4\pi} L'_\nu(\mathbf{u},\mathbf{r})\mathbf{u}d\Omega \tag{D.18}$$

$$P^R(\mathbf{r},t) \;=\; -div(\mathbf{q}^R) \;=\; -\int_0^\infty \int^{4\pi} div[L'_\nu(\mathbf{u},\mathbf{r})\mathbf{u}]d\Omega d\nu \tag{D.19}$$

Another way of expressing P^R from the RTE

$$\frac{d}{ds}L'_\nu \;=\; div(L'_\nu\mathbf{u}) \tag{D.20}$$

By Eq (D.10), and since the scattering terms outweigh each other, the equation (D.19) can be simplified to the power due to absorption P^a and emission P^e

$$P^R(\mathbf{r},t) \;=\; \int_0^\infty \int^{4\pi} \kappa_\nu(\mathbf{r})L'_\nu(\mathbf{u},\mathbf{r})d\Omega d\nu - 4\pi\int_0^\infty \kappa_\nu(\mathbf{r})L^0_\nu(T)d\nu \;=\; P^a - P^e \tag{D.21}$$

D.3 Numerical Methods: Statistical Narrow Band (SNB) Model

The gas absorption coefficient (and with it, the radiative intensity) varies much more rapidly across the spectrum than other quantities, such as blackbody intensity, etc. Therefore, to calculate spectral radiative fluxes from a molecular gas, we can replace the actual absorption coefficient (and intensity) by smoothened values appropriately averaged over a narrow spectral range (Modest 2013). Consider an interval $\Delta\nu_k = [\nu_k - \Delta\nu_k/2, \nu_k + \Delta\nu_k/2]$ centered around the wave number ν_k. The local averages of the spectral absorption coefficient and of the spectral emissivity are indicated respectively by

$$\bar{\kappa}_\nu(\nu_k) = \frac{1}{\Delta\nu_k}\int_{\nu_k-\Delta\nu_k/2}^{\nu_k+\Delta\nu_k/2} \kappa_\nu d\nu'$$

$$\bar{\epsilon}_\nu(\nu_k) = \frac{1}{\Delta\nu_k}\int_{\nu_k-\Delta\nu_k/2}^{\nu_k+\Delta\nu_k/2} [1-\exp(\int_0^X \kappa_\nu dX)]d\nu'$$

The SNB model, based on the Mayer and Goody approach, is chosen here in association with the Malkmus exponential-tailed S^{-1} line intensity distribution to express column transmissivities (Riviere and Soufiani 2012). The mean transmissivity of a uniform column of length l, at total pressure p, and with a molar fraction X_j of the absorbing species j, averaged on a narrow band of width $\Delta\nu_k$ is given by

$$\bar{\tau}_{\nu_k}(l, X_j, T, p) \;=\; \exp[-\frac{2\bar{\gamma}_k}{\bar{\delta}_k}(\sqrt{1+\frac{X_j p l \bar{k}_k \bar{\delta}_k}{\bar{\gamma}_k}}-1)] \tag{D.22}$$

The model parameters $\bar{k}_k$, $\bar{\gamma}_k$ and $\bar{\delta}_k$ are the mean line intensity to line spacing ratio, the average line Lorentz halfwidth, and the mean line spacing, as identified in the strong absorption limit, respectively. The transmissivity can be expressed by two parameters $\bar{k}_{\nu_k}$ and $\bar{\beta}_{\nu_k}$

$$\bar{\tau}_{\nu_k}(l, X_j, T, p) \;=\; \exp[-\frac{\bar{\beta}_{\nu_k}}{\pi}(\sqrt{1+\frac{2\pi X_j p l \bar{k}_{\nu_k}}{\bar{\beta}_{\nu_k}}}-1)] \tag{D.23}$$

where

$$\bar{\beta}_{\nu_k} = \frac{2\pi\bar{\gamma}_k}{\bar{\delta}_k}$$

D.4 1D formulation

Considering the participating media to be monodimensional, the solid angle can be chosen $d\Omega = 2\pi\sin\theta d\theta$ where θ is the angle between $\mathbf{u}$ and $\mathbf{n}$, which is

the direction vector of axis y, so equation (D.18) can be written as

$$\mathbf{q}^R = \left[\int_0^\infty d\nu \int_{\theta=0}^{\pi} L'_\nu(y,\theta) 2\pi \sin\theta \cos\theta d\theta\right]\mathbf{n} \tag{D.24}$$

$$P^R = \frac{d}{dy}\mathbf{q}^R = \int_0^\infty d\nu \int_{\theta=0}^{\pi} \frac{\partial L'_\nu(y,\theta)}{\partial y} 2\pi \sin\theta \cos\theta d\theta \tag{D.25}$$

Apllying Eq (D.15) and since

$$\cos\theta \frac{\partial L'_\nu(y,\theta)}{\partial y} = \frac{\partial L'_\nu(s,\theta)}{\partial y} \tag{D.26}$$

The radiative source term can be represented by

$$\begin{aligned} P^R(\mathbf{r},t) &= \frac{d}{dy}\mathbf{q}^R \\ &= \int_0^\infty d\nu \int_{\theta=0}^{\pi} \left[L'_\nu(0,\theta)\frac{\partial \tau_\nu}{\partial s}(0,s) + L^0_\nu(s)\frac{\partial \tau_\nu}{\partial s} + \int_0^s L^0_\nu(s')\frac{\partial^2 \tau_\nu}{\partial s \partial s'}(s',s) ds'\right] 2\pi \sin\theta d\theta \end{aligned} \tag{D.27}$$

More detail for the discretization and numerical solution of Eq (D.27) can be referred to the PhD thesis of Daguse (1996).

References

Aboyade, A. O., J. F. Gorgens, M. Carrier, E. L. Meyer, and J. H. Knoetze (2013). Thermogravimetric study of the pyrolysis characteristics and kinetics of coal blends with corn and sugarcane residues. *Fuel Processing Technology 106*, 310 – 320. *(p. 30)*

Agarwal, T. (2013). *Development of diagnostics for the experimental studies of ignition in sprays*. Ph. D. thesis, Ecole Centrale Paris. *(p. 29)*

Aguerre, F. (1996). *Etude expérimentale et numerique des flammes laminaires étirées stationnaires et instationnaires*. Ph. D. thesis, Ecole Centrale Paris. *(p. 82)*

Alviso, D. (2013). *Experimental and numerical characterization of the biodiesel combustion in a counterflow burner*. Ph. D. thesis, Ecole Centrale Paris. *(p. 58, 83, 107)*

Alviso, D., J. Rolon, P. Scouflaire, and N. Darabiha (2015). Experimental and numerical studies of biodiesel combustion mechanisms using a laminar counterflow spray premixed flame. *Fuel 153*, 154 – 165. *(p. xi, 18, 38, 96, 97, 129, 137, 138)*

Andersson, K., R. Johansson, S. Hjartstam, F. Johnsson, and B. Leckner (2008). Radiation intensity of lignite-fired oxy-fuel flames. *Experimental Thermal and Fluid Science 33*(1), 67 – 76. *(p. 12)*

Andersson, K. and F. Johnsson (2007). Flame and radiation characteristics of gas-fired o2/co2 combustion. *Fuel 86*(5 - 6), 656 – 668. *(p. 12)*

Anthony, D., J. Howard, H. Hottel, and H. Meissner (1975). Rapid devolatilization of pulverized coal. *Symposium (International) on Combustion 15*(1), 1303 – 1317. *(p. 73)*

Authier, O., E. Thunin, P. Plion, and L. Porcheron (2015). Global kinetic modeling of coal devolatilization in a thermogravimetric balance and drop-tube furnace. *Energy & Fuels 29*(3), 1461–1468. *(p. xiv, 31, 33)*

Backreedy, R., L. Fletcher, L. Ma, M. Pourkashanian, and A. Williams (2006a). Modelling pulverised coal combustion using a detailed coal combustion model. *Combustion Science and Technology 178*(4), 763–787. *(p. 12, 76)*

Backreedy, R., R. Habib, J. Jones, M. Pourkashanian, and A. Williams (1999). An extended coal combustion model. *Fuel 78*(14), 1745 – 1754.

(p. 12)

Backreedy, R. I., L. M. Fletcher, L. Ma, M. Pourkashanian, and A. Williams (2006b). Modelling pulverised coal combustion using a detailed coal combustion model. *Combustion Science and Technology 178*(4), 763–787. *(p. 70)*

Badzioch, S. and P. G. W. Hawksley (1970). Kinetics of thermal decomposition of pulverized coal particles. *Ind. Eng. Chem. Proc. DD. 9*(4), 521–530. *(p. 72, 95, 123)*

Bai, X., G. Lu, T. Bennet, A. Sarroza, C. Eastwick, H. Liu, and Y. Yan (2017). Combustion behavior profiling of single pulverized coal particles in a drop tube furnace through high-speed imaging and image analysis. *Experimental Thermal and Fluid Science 85*, 322 – 330. *(p. 32, 69)*

Bai, Y., K. Luo, K. Qiu, and J. Fan (2016). Numerical investigation of two-phase flame structures in a simplified coal jet flame. *Fuel 182*, 944 – 957. *(p. xiii, 15, 16)*

Balusamy, S., M. M. Kamal, S. M. Lowe, B. Tian, Y. Gao, and S. Hochgreb (2015). Laser diagnostics of pulverized coal combustion in o2/n2 and o2/co2 conditions: velocity and scalar field measurements. *Experiments in Fluids 56*(5), 108. *(p. xiv, 11, 14, 25, 26, 28, 29)*

Balusamy, S., A. Schmidt, and S. Hochgreb (2013). Flow field measurements of pulverized coal combustion using optical diagnostic techniques. *Experiments in Fluids 54*(5), 1534. *(p. xiv, 11, 25, 29, 30)*

Baum, M. and P. Street (1971). Predicting the combustion behaviour of coal particles. *Combust. Sci. Technol. 3*(5), 231–243. *(p. 75, 95)*

Bejarano, P. A. and Y. A. Levendis (2008). Single-coal-particle combustion in O2/N2 and O2/CO2 environments. *Combustion and Flame 153*(1-2), 270 – 287. *(p. 32)*

Bermudez, A., J. Ferrin, A. Linan, and L. Saavedra (2011). Numerical simulation of group combustion of pulverized coal. *Combustion and Flame 158*(9), 1852 – 1865. *(p. 13)*

Betbeder-rey, E. (2008). *Vers la prédiction des hydrocarbures imbrulés pour la combustion diesel: étude expérimentale et numérique de flammes de diffusion à contre-courant*. Ph. D. thesis, Ecole Centrale Paris. *(p. 82)*

Bradley, D., M. Lawes, H.-Y. Park, and N. Usta (2006). Modeling of laminar pulverized coal flames with speciated devolatilization and comparisons with experiments. *Combustion and Flame 144*(1-2), 190 – 204. *(p. 40)*

Bradley, D., M. Lawes, M. Scott, and N. Usta (2001). The structure of coal-air-ch4 laminar flames in a low-pressure burner: cars measurements and modeling studies. *Combustion and Flame 124*(1-2), 82 – 105. *(p. 39)*

Brosh, T. and N. Chakraborty (2014). Effects of equivalence ratio and turbulent velocity fluctuation on early stages of pulverized coal combustion following localized ignition: A direct numerical simulation analysis. *Energy & Fuels 28*(9), 6077–6088. *(p. 15)*

Brosh, T., D. Patel, D. Wacks, and N. Chakraborty (2015). Numerical in-

vestigation of localised forced ignition of pulverised coal particle-laden mixtures: A direct numerical simulation (dns) analysis. *Fuel 145*, 50 – 62. *(p. 15)*

Brown, M. E. (2001). *Introduction to Thermal Analysis: Techniques and Applications*. Springer. *(p. xiv, 31)*

Butler, B., M. Denison, and B. Webb (1994). Radiation heat transfer in a laboratory-scale, pulverized coal-fired reactor. *Experimental Thermal and Fluid Science 9*(1), 69 – 79. *(p. 26)*

Chen, L., S. Z. Yong, and A. F. Ghoniem (2012). Oxy-fuel combustion of pulverized coal: Characterization, fundamentals, stabilization and CFD modeling. *Progress in Energy and Combustion Science 38*(2), 156 – 214. *(p. 9)*

Clements, A. G., S. Black, J. Szuhanszki, K. Stechly, A. Pranzitelli, W. Nimmo, and M. Pourkashanian (2015). LES and RANS of air and oxy-coal combustion in a pilot-scale facility: Predictions of radiative heat transfer. *Fuel 151*, 146 – 155. The 10th European Conference on Coal Research and its Applications. *(p. 14)*

ClimateTechWiki (2010). Pulverised coal combustion with higher efficiency. http://www.climatetechwiki.org/technology/sup_crit_coal. Accessed: 2017-06-20. *(p. 7)*

Cordoba, P. (2015). Status of flue gas desulphurisation (FGD) systems from coal-fired power plants: Overview of the physic-chemical control processes of wet limestone FGDs. *Fuel 144*, 274–286. *(p. 7)*

Costa, M. and J. L. T. Azevedo (2007). Experimental characterization of an industrial pulverized coal-fired furnace under deep staging conditions. *Combustion Science and Technology 179*(9), 1923–1935. *(p. 11)*

Costa, M., P. Silva, and J. L. T. Azevedo (2003). Measurements of gas species, temperature, and char burnout in a low-no x pulverized-coal-fired utility boiler. *Combustion Science and Technology 175*(2), 271–289. *(p. 11)*

Croonenbroek, T. (1996). *Diagnostics optiques appliqués aux milieux réactifs: Application aux flammes laminaires étirées à contre-courant*. Ph. D. thesis, Ecole Centrale Paris. *(p. 82)*

Daguse, T. (1996). *Effets du rayonnement thermique sur la structure de flammes laminaires de diffusion ou de prémelange*. Ph. D. thesis, Ecole Centrale Paris. *(p. 82, 145)*

Daguse, T., T. Croonenbroek, J. Rolon, N. Darabiha, and A. Soufiani (1996). Study of radiative effects on laminar counterflow H2/O2/N2 diffusion flames. *Combust. Flame 106*(3), 271–287. *(p. 18)*

DARABIHA, N. and S. CANDEL (1992). The influence of the temperature on extinction and ignition limits of strained hydrogen-air diffusion flames. *Combustion Science and Technology 86*(1-6), 67–85. *(p. 82)*

Darabiha, N., F. Lacas, J. Rolon, and S. Candel (1993). Laminar counterflow spray diffusion flames: A comparison between experimental results and complex chemistry calculations. *Combustion and Flame 95*(3), 261 – 275.

(p. 38, 82)

de Jong, W. (2005). *Combustion of solid fuels, Course on Combustion*. Burgers Centrum. *(p. xiii, 25)*

Demirbas, A. and M. Balat (2004). Coal desulfurization via different methods. *Energy Sources 26*(6), 541–550. *(p. 7)*

Demtröder, W. (2008). *Laser Spectroscopy: Vol.1 Basic Principles*. Springer Berlin Heidelberg. *(p. xiii, 27)*

Docquier, N., S. Belhalfaoui, F. Lacas, N. Darabiha, and C. Rolon (2000). Experimental and numerical study of chemiluminescence in methane/air high-pressure flames for active control applications. *Proceedings of the Combustion Institute 28*(2), 1765 – 1774. *(p. 27)*

Donahue, C. J. and E. A. Rais (2009). Proximate analysis of coal. *Journal of Chemical Education 86*(2), 222. *(p. 68)*

Edge, P., M. Gharebaghi, R. Irons, R. Porter, R. Porter, M. Pourkashanian, D. Smith, P. Stephenson, and A. Williams (2011). Combustion modelling opportunities and challenges for oxy-coal carbon capture technology. *Chemical Engineering Research and Design 89*(9), 1470 – 1493. Special Issue on Carbon Capture and Storage. *(p. 13)*

Edge, P., S. Gubba, L. Ma, R. Porter, M. Pourkashanian, and A. Williams (2011). LES modelling of air and oxy-fuel pulverised coal combustion-impact on flame properties. *Proceedings of the Combustion Institute 33*(2), 2709 – 2716. *(p. 14)*

Franchetti, B., F. C. Marincola, S. Navarro-Martinez, and A. Kempf (2013). Large eddy simulation of a pulverised coal jet flame. *Proceedings of the Combustion Institute 34*(2), 2419 – 2426. *(p. 13, 77)*

Franchetti, B., F. C. Marincola, S. Navarro-Martinez, and A. Kempf (2016). Large eddy simulation of a 100 kwth swirling oxy-coal furnace. *Fuel 181*, 491 – 502. *(p. 70)*

Franzelli, B., B. Fiorina, and N. Darabiha (2013). A tabulated chemistry method for spray combustion. *Proc. Combust. Inst. 34*(1), 1659 – 1666. *(p. 18, 38, 83)*

Gaydon, A. (1957). *The Spectroscopy of Flames*. Wiley. *(p. 27, 47, 51)*

Gharebaghi, M., R. Irons, L. Ma, M. Pourkashanian, and A. Pranzitelli (2011). Large eddy simulation of oxy-coal combustion in an industrial combustion test facility. *International Journal of Greenhouse Gas Control 5, Supplement 1*, S100 – S110. Oxyfuel Combustion Technology - Working Toward Demonstration and Commercialisation. *(p. 13)*

Giovangigli, V. (1988). *Structure et extinction de flammes laminaires premelangées*. Ph. D. thesis, Université Paris VI. *(p. 82)*

Godridge, A. (2010). Pulverized coal furnaces. DOI:10.1615/AtoZ.p.pulverized_coal_furnaces. Accessed: 2017-06-20. *(p. 6)*

Grant, D. M., R. J. Pugmire, T. H. Fletcher, and A. R. Kerstein (1989). Chemical model of coal devolatilization using percolation lattice statistics. *Energy & Fuels 3*(2), 175–186. *(p. 74, 96)*

Graves, D. and J. Wendt (1982). Flammability characteristics and structure of a pulverized coal, laminar opposed jet diffusion flame. *Symposium (International) on Combustion 19*(1), 1189 – 1196. *(p. 38)*

Gubba, S., D. Ingham, K. Larsen, L. Ma, M. Pourkashanian, H. Tan, A. Williams, and H. Zhou (2012). Numerical modelling of the co-firing of pulverised coal and straw in a 300 MWe tangentially fired boiler. *Fuel Processing Technology 104*, 181 – 188. *(p. 12)*

Hancock, R. D., K. W. Boyack, and P. O. Hedman (1992). *Coherent Anti-Stokes Raman Spectroscopy (CARS) in Pulverized Coal Flames*. Boston, MA: Springer US. *(p. 26)*

Hara, T., M. Muto, T. Kitano, R. Kurose, and S. Komori (2015). Direct numerical simulation of a pulverized coal jet flame employing a global volatile matter reaction scheme based on detailed reaction mechanism. *Combustion and Flame 162*(12), 4391 – 4407. *(p. 15, 69, 75, 96)*

Hashimoto, N., J. Hayashi, N. Nakatsuka, K. Tainaka, S. Umemoto, H. Tsuji, F. Akamatsu, H. Watanabe, and H. Makino (2016). Primary soot particle distributions in a combustion field of 4 kw pulverized coal jet burner measured by time resolved laser induced incandescence (TiRe-LII). *Journal of Thermal Science and Technology 11*(3), JTST0049–JTST0049. *(p. 26)*

Hashimoto, N., R. Kurose, S.-M. Hwang, H. Tsuji, and H. Shirai (2012). A numerical simulation of pulverized coal combustion employing a tabulated-devolatilization-process model (TDP model). *Combustion and Flame 159*(1), 353 – 366. *(p. 12, 13, 75)*

Hashimoto, N., R. Kurose, and H. Shirai (2012). Numerical simulation of pulverized coal jet flame employing the TDP model. *Fuel 97*, 277 – 287. *(p. xv, 12, 75, 77)*

Hayashi, J., N. Hashimoto, N. Nakatsuka, H. Tsuji, H. Watanabe, H. Makino, and F. Akamatsu (2013). Soot formation characteristics in a lab-scale turbulent pulverized coal flame with simultaneous planar measurements of laser induced incandescence of soot and mie scattering of pulverized coal. *Proceedings of the Combustion Institute 34*(2), 2435 – 2443. *(p. 26)*

Hees, J., D. Zabrodiec, A. Massmeyer, S. Pielsticker, B. Govert, M. Habermehl, O. Hatzfeld, and R. Kneer (2016). Detailed analyzes of pulverized coal swirl flames in oxy-fuel atmospheres. *Combustion and Flame 172*, 289 – 301. *(p. xiii, 12, 13)*

Heil, P., D. Toporov, H. Stadler, S. Tschunko, M. Forster, and R. Kneer (2009). Development of an oxycoal swirl burner operating at low O2 concentrations. *Fuel 88*(7), 1269 – 1274. Selected Papers from the 2007 World of Coal Ash Conference. *(p. 12, 13)*

Hjartstam, S., K. Andersson, F. Johnsson, and B. Leckner (2009). Combustion characteristics of lignite-fired oxy-fuel flames. *Fuel 88*(11), 2216 – 2224. *(p. 12)*

Hurt, R., J.-K. Sun, and M. Lunden (1998). A kinetic model of carbon burnout in pulverized coal combustion. *Combustion and Flame 113*(1-

2), 181 – 197. *(p. 76)*

Hurt, R. H. and J. M. Calo (2001). Semi-global intrinsic kinetics for char combustion modeling. *Combustion and Flame 125*(3), 1138 – 1149. *(p. 76)*

Hurt, R. H. and J. R. Gibbins (1995). Residual carbon from pulverized coal fired boilers: 1. size distribution and combustion reactivity. *Fuel 74*(4), 471 – 480. *(p. 31)*

Hwang, S. m., R. Kurose, F. Akamatsu, H. Tsuji, H. Makino, and M. Katsuki (2005). Application of optical diagnostics techniques to a laboratory-scale turbulent pulverized coal flame. *Energy & Fuels 19*(2), 382–392. *(p. 11, 15, 25, 26, 28, 78)*

International Energy Agency (2012). Technology roadmap: High-efficiency, low-emissions coal-fired power generation. Technical report, OECD/IEA. *(p. xiii, 6, 9)*

International Energy Agency (2016). Medium-Term Coal Market Report 2016. https://www.iea.org/newsroom/news/2016/december/medium-term-coal-market-report-2016.html. Accessed: 2017-06-10. *(p. 2)*

Jovanovic, R., B. Rasuo, P. Stefanovic, D. Cvetinovic, and B. Swiatkowski (2013). Numerical investigation of pulverized coal jet flame characteristics under different oxy-fuel conditions. *International Journal of Heat and Mass Transfer 58*(1-2), 654 – 662. *(p. 13)*

Kathrotia, T., U. Riedel, A. Seipel, K. Moshammer, and A. Brockhinke (2012). Experimental and numerical study of chemiluminescent species in low-pressure flames. *Applied Physics B 107*(3), 571–584. *(p. xi, 96, 97, 129, 137, 140)*

Kee, R. J., G. Dixon-lewis, J. Warnatz, M. E. Coltrin, and J. A. Miller (1986). A fortran computer code package for the evaluation of gas-phase, multicomponent transport properties. Technical report, Sand86-8246. *(p. 85)*

Khatami, R., C. Stivers, K. Joshi, Y. A. Levendis, and A. F. Sarofim (2012). Combustion behavior of single particles from three different coal ranks and from sugar cane bagasse in O2/N2 and O2/CO2 atmospheres. *Combustion and Flame 159*(3), 1253 – 1271. *(p. 31, 32)*

Kobayashi, H., J. Howard, and A. Sarofim (1977). Coal devolatilization at high temperatures. *Symposium (International) on Combustion 16*(1), 411 – 425. *(p. 73, 95, 123)*

Kojima, J., Y. Ikeda, and T. Nakajima (2005). Basic aspects of OH(A), CH(A), and C2(d) chemiluminescence in the reaction zone of laminar methane-air premixed flames. *Combustion and Flame 140*(1-2), 34 – 45. *(p. 96)*

Korytnyi, E., R. Saveliev, M. Perelman, B. Chudnovsky, and E. Bar-Ziv (2009). Computational fluid dynamic simulations of coal-fired utility boilers: An engineering tool. *Fuel 88*(1), 9 – 18. *(p. 12)*

Köser, J., L. G. Becker, N. Vorobiev, M. Schiemann, V. Scherer, B. Böhm, and A. Dreizler (2015). Characterization of single coal particle combustion

within oxygen-enriched environments using high-speed oh-plif. *Applied Physics B 121*(4), 459–464. *(p. 32)*

Kuo, K. (2005). *Principles of combustion*. John Wiley. *(p. 30)*

Kurose, R. and H. Makino (2003). Large eddy simulation of a solid-fuel jet flame. *Combustion and Flame 135*(1), 1–16. *(p. 13)*

Kurose, R., H. Makino, and A. Suzuki (2004). Numerical analysis of pulverized coal combustion characteristics using advanced low-nox burner. *Fuel 83*(6), 693 – 703. *(p. 12, 90)*

Kurose, R., H. Tsuji, and H. Makino (2001). Effects of moisture in coal on pulverized coal combustion characteristics. *Fuel 80*(10), 1457 – 1465. *(p. 12)*

Kurose, R., H. Watanabe, and H. Makino (2009). Numerical simulations of pulverized coal combustion. *KONA Powder and Particle Journal 27*, 144–156. *(p. 12, 13)*

Lacas, F., N. Darabiha, P. Versaevel, J. Rolon, and S. Candel (1992). Influence of droplet number density on the structure of strained laminar spray flames. *Symposium (International) on Combustion 24*(1), 1523 – 1529. *(p. 18, 38)*

Lacas, F., B. Leroux, and N. Darabiha (2005). Experimental study of air dilution in oxy-liquid fuel flames. *Proceedings of the Combustion Institute 30*(2), 2037 – 2045. *(p. 28)*

Le Manquais, K., C. Snape, I. McRobbie, J. Barker, and V. Pellegrini (2009). Comparison of the combustion reactivity of tga and drop tube furnace chars from a bituminous coal. *Energy & Fuels 23*(9), 4269–4277. *(p. 31)*

Lemaire, R., D. Menage, S. Menanteau, and J.-L. Harion (2014). Experimental study and kinetic modeling of pulverized coal devolatilization under air and oxycombustion conditions at a high heating rate. *Fuel Processing Technology 128*, 183 – 190. *(p. 25, 26, 34, 72, 95)*

Lemaire, R. and S. Menanteau (2016). Development and numerical/experimental characterization of a lab-scale flat flame reactor allowing the analysis of pulverized solid fuel devolatilization and oxidation at high heating rates. *Review of Scientific Instruments 87*(1), 015104. *(p. xiv, 35)*

Leo, M. D., A. Saveliev, L. A. Kennedy, and S. A. Zelepouga (2007). OH and CH luminescence in opposed flow methane oxy-flames. *Combustion and Flame 149*(4), 435 – 447. *(p. 96)*

Li, B., G. Chen, H. Zhang, and C. Sheng (2014). Development of non-isothermal tga-dsc for kinetics analysis of low temperature coal oxidation prior to ignition. *Fuel 118*, 385 – 391. *(p. 31)*

Li, H., L. Elliott, H. Rogers, P. Austin, Y. Jin, and T. Wall (2012). Reactivity study of two coal chars produced in a drop-tube furnace and a pulverized coal injection rig. *Energy & Fuels 26*(8), 4690–4695. *(p. 31)*

Li, Z., J. Jing, Z. Chen, F. Ren, B. Xu, H. Wei, and Z. Ge (2008). Combustion characteristics and no x emissions of two kinds of swirl burners in a

300-mwe wall-fired pulverized-coal utility boiler. *Combustion Science and Technology 180*(7), 1370–1394. *(p. 11)*

Liu, G.-S. and S. Niksa (2004). Coal conversion submodels for design applications at elevated pressures. part ii. char gasification. *Progress in Energy and Combustion Science 30*(6), 679 – 717. *(p. 76)*

Liu, Y., M. Geier, A. Molina, and C. R. Shaddix (2011). Pulverized coal stream ignition delay under conventional and oxy-fuel combustion conditions. *International Journal of Greenhouse Gas Control 5, Supplement 1*, S36 – S46. *(p. 33)*

Liu, Y., X. Guo, H. Lu, and X. Gong (2015). An investigation of the effect of particle size on the flow behavior of pulverized coal. *Procedia Engineering 102*, 698 – 713. *(p. 69)*

Liu, Y., G. Vourliotakis, Y. Hardalupas, and A. M. Taylor (2017). Experimental and numerical study of chemiluminescence characteristics in premixed counterflow flames of methane based fuel blends. *55th AIAA Aerospace Sciences Meeting*, AIAA 2017–0153. *(p. 96, 111, 137)*

Lockwood, F. and A. Salooja (1983). The prediction of some pulverized bituminous coal flames in a furnace. *Combustion and Flame 54*(1), 23 – 32. *(p. 12)*

Lockwood, F., A. Salooja, and S. Syed (1980). A prediction method for coal-fired furnaces. *Combustion and Flame 38*, 1 – 15. *(p. 12)*

Lu, J. and X. Ren (2014). Analysis and discussion on formation and control of primary particulate matter generated from coal-fired power plants. *Journal of the Air & Waste Management Association 64*(12), 1342–1351. *(p. 8)*

Luo, K., H. Wang, J. Fan, and F. Yi (2012). Direct numerical simulation of pulverized coal combustion in a hot vitiated co-flow. *Energy & Fuels 26*(10), 6128–6136. *(p. 15)*

Ma, L., M. Gharebaghi, R. Porter, M. Pourkashanian, J. Jones, and A. Williams (2009). Modelling methods for co-fired pulverised fuel furnaces. *Fuel 88*(12), 2448 – 2454. 7th European Conference on Coal Research and Its Applications. *(p. 12)*

Makino, K. (2016). *Clean Coal Technology—For the Future Utilization*, pp. 3–9. Springer Singapore. *(p. 10)*

Mathews, J. P., S. Eser, P. G. Hatcher, and A. W. Scaroni (2007). The shape of pulverized bituminous vitrinite coal particles. *KONA Powder and Particle Journal 25*, 145–152. *(p. 69)*

Merotto, L., M. Sirignano, M. Commodo, A. D'Anna, R. Donde, and S. De Iuliis (2017). Experimental characterization and modeling for equivalence ratio sensing in non-premixed flames using chemiluminescence and laser-induced breakdown spectroscopy techniques. *Energy & Fuels 31*(3), 3227–3233. *(p. 46)*

Merrick, D. (1983). Mathematical models of the thermal decomposition of coal. *Fuel 62*(5), 540 – 546. *(p. 70)*

Messig, D., M. Vascellari, and C. Hasse (2017). Flame structure analysis and flamelet progress variable modelling of strained coal flames. *Combustion Theory and Modelling 21*(4), 700–721. *(p. 38, 70)*

Midou, D. (2017). *Large-Eddy Simulation of Pulverised-Coal Combustion*. Ph. D. thesis, CORIA. *(p. 14)*

Minchener, A. (2013). *Coal and Clean Coal Technology: Challenges and Opportunities*, pp. 3–10. Springer Berlin Heidelberg. *(p. 10)*

Modest, M. (2013). *Radiative Heat Transfer*. Elsevier Science. *(p. 144)*

Molina, A. and C. R. Shaddix (2007). Ignition and devolatilization of pulverized bituminous coal particles during oxygen/carbon dioxide coal combustion. *Proceedings of the Combustion Institute 31*(2), 1905 – 1912. *(p. xiv, 11, 25, 27, 28, 33, 34)*

Mulla, I. A., A. Dowlut, T. Hussain, Z. M. Nikolaou, S. R. Chakravarthy, N. Swaminathan, and R. Balachandran (2016). Heat release rate estimation in laminar premixed flames using laser-induced fluorescence of ch2o and h-atom. *Combustion and Flame 165*, 373 – 383. *(p. 101)*

Muto, M., K. Tanno, and R. Kurose (2016). A DNS study on effect of coal particle swelling due to devolatilization on pulverized coal jet flame. *Fuel 184*, 749 – 752. *(p. 15)*

Muto, M., H. Watanabe, R. Kurose, S. Komori, S. Balusamy, and S. Hochgreb (2015). Large-eddy simulation of pulverized coal jet flame - effect of oxygen concentration on NOx formation. *Fuel 142*, 152–163. *(p. 14)*

Muto, M., K. Yuasa, and R. Kurose (2017). Numerical simulation of ignition in pulverized coal combustion with detailed chemical reaction mechanism. *Fuel 190*, 136 – 144. *(p. 15)*

Nalbandian, H. (2009, Jul). Performance and risks of advanced pulverized-coal plants. *Energeia (Lexington) 20*(1). *(p. 7)*

Nikolaou, Z. M. and N. Swaminathan (2014). Heat release rate markers for premixed combustion. *Combustion and Flame 161*(12), 3073 – 3084. *(p. 100)*

Niksa, S. and A. R. Kerstein (1991). Flashchain theory for rapid coal devolatilization kinetics. 1. formulation. *Energy & Fuels 5*(5), 647–665. *(p. 74, 96)*

Olenik, G., O. Stein, and A. Kronenburg (2015). LES of swirl-stabilised pulverised coal combustion in IFRF furnace no. 1. *Proceedings of the Combustion Institute 35*(3), 2819 – 2828. *(p. 14)*

Panoutsos, C., Y. Hardalupas, and A. Taylor (2009). Numerical evaluation of equivalence ratio measurement using oh and ch chemiluminescence in premixed and non-premixed methane-air flames. *Combustion and Flame 156*(2), 273 – 291. *(p. xi, 48, 96, 111, 138)*

Parameswaran, T., R. Hughes, P. Gogolek, and P. Hughes (2014). Gasification temperature measurement with flame emission spectroscopy. *Fuel 134*, 579 – 587. *(p. 26)*

Partha Das Sharma (2008). Supercritical coal-fired power plant. https://saferenvironment.wordpress.com/2008/12/29/. Accessed: 2017-06-20. *(p. xiii, 5)*

Peters, A. A. F. and R. Weber (1997). Mathematical modeling of a 2.4 mw swirling pulverized coal flame. *Combustion Science and Technology 122*(1-6), 131 – 182. *(p. 12)*

Peters, N. (1984). Laminar diffusion flamelet models in non-premixed turbulent combustion. *Progress in Energy and Combustion Science 10*(3), 319 – 339. *(p. 14)*

Peters, N. (2000). *Turbulent Combustion*. Cambridge University Press. *(p. 18)*

Rabacal, M., B. Franchetti, F. C. Marincola, F. Proch, M. Costa, C. Hasse, and A. Kempf (2015). Large eddy simulation of coal combustion in a large-scale laboratory furnace. *Proceedings of the Combustion Institute 35*(3), 3609 – 3617. *(p. 14, 77)*

Ranade, V. and D. Gupta (2014). *Computational Modeling of Pulverized Coal Fired Boilers*. Taylor & Francis. *(p. 95)*

Reverte, C., J.-L. Dirion, and M. Cabassud (2007). Kinetic model identification and parameters estimation from TGA experiments. *Journal of Analytical and Applied Pyrolysis 79*(1-2), 297 – 305. *(p. 30)*

Riaza, J., R. Khatami, Y. A. Levendis, L. Alvarez, M. V. Gil, C. Pevida, F. Rubiera, and J. J. Pis (2014). Single particle ignition and combustion of anthracite, semi-anthracite and bituminous coals in air and simulated oxy-fuel conditions. *Combustion and Flame 161*(4), 1096 – 1108. *(p. 31)*

Ribeirete, A. and M. Costa (2009). Detailed measurements in a pulverized-coal-fired large-scale laboratory furnace with air staging. *Fuel 88*(1), 40 – 45. *(p. 11)*

Rieth, M., A. Clements, M. Rabacal, F. Proch, O. Stein, and A. Kempf (2017). Flamelet LES modeling of coal combustion with detailed devolatilization by directly coupled CPD. *Proceedings of the Combustion Institute 36*(2), 2181 – 2189. *(p. 38, 78)*

Rieth, M., F. Proch, M. Rabacal, B. Franchetti, F. C. Marincola, and A. Kempf (2016). Flamelet LES of a semi-industrial pulverized coal furnace. *Combustion and Flame 173*, 39 – 56. *(p. xiii, 14, 15, 70)*

Riviere, P. and A. Soufiani (2012). Updated band model parameters for H2O, CO2, CH4 and CO radiation at high temperature. *International Journal of Heat and Mass Transfer 55*(13-14), 3349 – 3358. *(p. 144)*

Rolon, J. (1988). *Etude théorique et expérimentale de la flamme de diffusion à contre-courant*. Ph. D. thesis, Ecole Centrale Paris. *(p. 82)*

Sadiki, A., S. Agrebi, M. Chrigui, A. Doost, R. Knappstein, F. D. Mare, J. Janicka, A. Massmeyer, D. Zabrodiec, J. Hees, and R. Kneer (2017). Analyzing the effects of turbulence and multiphase treatments on oxy-coal combustion process predictions using LES and RANS. *Chemical Engineering Science 166*, 283 – 302. *(p. 12, 13, 14)*

Schiemann, M., S. Haarmann, and N. Vorobiev (2014). Char burning kinetics from imaging pyrometry: Particle shape effects. *Fuel 134*, 53 – 62. *(p. xv, 69, 70)*

Schiemann, M., V. Scherer, and S. Wirtz (2009). Optical coal particle temperature measurement under oxy-fuel conditions: Measurement methodology and initial results. *Chemical Engineering & Technology 32*(12), 2000–2004. *(p. 26, 34)*

Seo, D. K., S. S. Park, Y. T. Kim, J. Hwang, and T.-U. Yu (2011). Study of coal pyrolysis by thermo-gravimetric analysis (tga) and concentration measurements of the evolved species. *Journal of Analytical and Applied Pyrolysis 92*(1), 209 – 216. *(p. 30)*

Shaddix, C. R. and A. Molina (2009). Particle imaging of ignition and devolatilization of pulverized coal during oxy-fuel combustion. *Proceedings of the Combustion Institute 32*(2), 2091 – 2098. *(p. 25, 33)*

Shanthakumar, S., D. Singh, and R. Phadke (2008). Flue gas conditioning for reducing suspended particulate matter from thermal power stations. *Progress in Energy and Combustion Science 34*(6), 685 – 695. *(p. 8)*

Shi, L., Q. Liu, X. Guo, W. Wu, and Z. Liu (2013). Pyrolysis behavior and bonding information of coal - a TGA study. *Fuel Processing Technology 108*, 125 – 132. *(p. 30)*

Smart, J., K. Knill, B. Visser, and R. Weber (1989). Reduction of nox emissions in a swirled coal flame by particle injection into the internal recirculation zone. *Symposium (International) on Combustion 22*(1), 1117 – 1125. *(p. 12)*

Smith, G. P., J. Luque, C. Park, J. B. Jeffries, and D. R. Crosley (2002). Low pressure flame determinations of rate constants for oh(a) and ch(a) chemiluminescence. *Combustion and Flame 131*(1-2), 59 – 69. *(p. 49, 96)*

Smith, G. P., C. Park, and J. Luque (2005). A note on chemiluminescence in low-pressure hydrogen and methane-nitrous oxide flames. *Combustion and Flame 140*(4), 385 – 389. *(p. 48)*

Smith, G. P., C. Park, J. Schneiderman, and J. Luque (2005). C2 swan band laser-induced fluorescence and chemiluminescence in low-pressure hydrocarbon flames. *Combustion and Flame 141*(1-2), 66 – 77. *(p. 49, 96)*

Smith, I. (1982). The combustion rates of coal chars: A review. *Symposium (International) on Combustion 19*(1), 1045 – 1065. *(p. 76)*

Smith, I. W. (1978). The intrinsic reactivity of carbons to oxygen. *Fuel 57*(7), 409 – 414. *(p. 76)*

Smolarz, A., A. Kotyra, W. Wojcik, and J. Ballester (2012). Advanced diagnostics of industrial pulverized coal burner using optical methods and artificial intelligence. *Experimental Thermal and Fluid Science 43*, 82 – 89. Seventh Mediterranean Combustion Symposium. *(p. 26)*

Solomon, P. R., D. G. Hamblen, R. M. Carangelo, M. A. Serio, and G. V.

Deshpande (1988). General model of coal devolatilization. *Energy & Fuels 2*(4), 405–422. *(p. 74, 96)*

Speight, J. (2005). *Handbook of Coal Analysis*. Chemical Analysis: A Series of Monographs on Analytical Chemistry and Its Applications. Wiley. *(p. 68, 69)*

Stein, O., G. Olenik, A. Kronenburg, F. Cavallo Marincola, B. Franchetti, A. Kempf, M. Ghiani, M. Vascellari, and C. Hasse (2013). Towards comprehensive coal combustion modelling for les. *Flow, Turbulence and Combustion 90*(4), 859–884. *(p. xiii, 13, 14, 77)*

Taine, J., F. Enguehard, and E. Iacona (2014). *Transferts thermiques: Introduction aux transferts d'énergie : cours et exercices d'application*. Sciences sup. Dunod. *(p. 142)*

Tognotti, L., A. Malotti, L. Petarca, and S. Zanelli (1985). Measurement of ignition temperature of coal particles using a thermogravimetric technique. *Combustion Science and Technology 44*(1-2), 15–28. *(p. 31)*

Toporov, D., P. Bocian, P. Heil, A. Kellermann, H. Stadler, S. Tschunko, M. Forster, and R. Kneer (2008). Detailed investigation of a pulverized fuel swirl flame in co2/o2 atmosphere. *Combustion and Flame 155*(4), 605 – 618. *(p. 12)*

Truelove, J. (1988). Prediction of the near-burner flow and combustion in swirling pulverized-coal flames. *Symposium (International) on Combustion 21*(1), 275 – 284. *(p. 12)*

Truelove, J. and R. Williams (1989). Coal combustion models for flame scaling. *Symposium (International) on Combustion 22*(1), 155 – 164. *(p. 12)*

Tufano, G., O. Stein, A. Kronenburg, A. Frassoldati, T. Faravelli, L. Deng, A. Kempf, M. Vascellari, and C. Hasse (2016). Resolved flow simulation of pulverized coal particle devolatilization and ignition in air- and o2/co2-atmospheres. *Fuel 186*, 285 – 292. *(p. 17)*

Ubhayakar, S. K., D. B. Stickler, C. W. V. Rosenberg, and R. E. Gannon (1977). Rapid devolatilization of pulverized coal in hot combustion gases. *Symposium (International) on Combustion 16*(1), 427 – 436. *(p. 73)*

U.S. Energy Information Administration (2016). International energy outlook 2016. Technical report, U.S. Energy Information Administration. *(p. 2, 3)*

Vagelopoulos, C., F. Egolfopoulos, and C. Law (1994). Further considerations on the determination of laminar flame speeds with the counterflow twin-flame technique. *Symposium (International) on Combustion 25*(1), 1341 – 1347. Twenty-Fifth Symposium (International) on Combustion. *(p. 97)*

Vagelopoulos, C. M. and F. N. Egolfopoulos (1998). Direct experimental determination of laminar flame speeds. *Symposium (International) on Combustion 27*(1), 513 – 519. Twenty-Seventh Sysposium (International) on Combustion Volume One. *(p. 97)*

Vascellari, M., R. Arora, and C. Hasse (2014). Simulation of entrained flow gasification with advanced coal conversion submodels. part 2: Char con-

version. *Fuel 118*, 369 – 384. *(p. 77)*

Vascellari, M., R. Arora, M. Pollack, and C. Hasse (2013). Simulation of entrained flow gasification with advanced coal conversion submodels. part 1: Pyrolysis. *Fuel 113*, 654 – 669. *(p. xv, 77, 78)*

Vascellari, M., H. Xu, and C. Hasse (2013). Flamelet modeling of coal particle ignition. *Proceedings of the Combustion Institute 34*(2), 2445 – 2452. *(p. 15, 17, 38)*

Versaevel, P. (1996). *Combustion laminaire diphasique: Etude théorique et expérimentale*. Ph. D. thesis, Ecole Centrale Paris. *(p. 82)*

Wan, K., J. Xia, Z. Wang, L. C. Wrobel, and K. Cen (2017). Online-cpd-coupled large-eddy simulation of pulverized-coal pyrolysis in a hot turbulent nitrogen jet. *Combustion Science and Technology 189*(1), 103–131. *(p. xv, 71, 78)*

Wang, G., R. Silva, J. Azevedo, S. Martins-Dias, and M. Costa (2014). Evaluation of the combustion behaviour and ash characteristics of biomass waste derived fuels, pine and coal in a drop tube furnace. *Fuel 117, Part A*, 809 – 824. *(p. 32)*

Wang, G., R. Zander, and M. Costa (2014). Oxy-fuel combustion characteristics of pulverized-coal in a drop tube furnace. *Fuel 115*, 452 – 460. *(p. xiv, 31, 32)*

Wang, H., X. You, A. V. Joshi, S. G. Davis, A. Laskin, F. Egolfopoulos, and C. K. Law (2007). USC Mech Version II. High-Temperature Combustion Reaction Model of H2/CO/C1-C4 Compounds. http://ignis.usc.edu/USC_Mech_II.htm. Accessed: 2017-06-10. *(p. 96)*

Warzecha, P. and A. Boguslawski (2014). LES and RANS modeling of pulverized coal combustion in swirl burner for air and oxy-combustion technologies. *Energy 66*, 732 – 743. *(p. 13, 14)*

Watanabe, J., T. Okazaki, K. Yamamoto, K. Kuramashi, and A. Baba (2017). Large-eddy simulation of pulverized coal combustion using flamelet model. *Proceedings of the Combustion Institute 36*(2), 2155 – 2163. *(p. 14)*

Watanabe, J. and K. Yamamoto (2015). Flamelet model for pulverized coal combustion. *Proceedings of the Combustion Institute 35*(2), 2315 – 2322. *(p. 14, 38)*

Weber, R., J. Dugue, A. Sayre, and B. Visser (1992). Quarl zone flow field and chemistry of swirling pulverized coal flames: Measurements and computation. *Symposium (International) on Combustion 24*(1), 1373 – 1380. *(p. 12, 14)*

Wendt, J., B. Kram, M. Masteller, and B. McCaslin (1988). Coal pyrolysis in flat, laminar, opposed jet combustion configurations. *Symposium (International) on Combustion 21*(1), 419 – 426. *(p. 38)*

World Coal Association (2005). The coal resource. https://www.worldcoal.org/coal-resource. Accessed: 2017-06-26. *(p. 9)*

World Coal Association (2017). WCA basic coal facts. www.worldcoal.org/

basic-coal-facts. Accessed: 2017-06-26. *(p. xiii, 1, 2)*

Xia, M., D. Zabrodiec, P. Scouflaire, B. Fiorina, and N. Darabiha (2017). Experimental and numerical studies of pulverized coal devolatilization and oxidation in strained methane/air flames. *Proceedings of the Combustion Institute 36*(2), 2123 – 2130. *(p. 25, 28, 29, 40, 41, 59)*

Xu, W.-C. and A. Tomita (1987a). Effect of coal type on the flash pyrolysis of various coals. *Fuel 66*(5), 627 – 631. *(p. 75, 96)*

Xu, W.-C. and A. Tomita (1987b). Effect of temperature on the flash pyrolysis of various coals. *Fuel 66*(5), 632 – 636. *(p. 75)*

Yamamoto, K., T. Murota, T. Okazaki, and M. Taniguchi (2011). Large eddy simulation of a pulverized coal jet flame ignited by a preheated gas flow. *Proceedings of the Combustion Institute 33*(2), 1771 – 1778. *(p. 13)*

Yan, W., Y. Ya, F. Du, H. Shao, and P. Zhao (2017). Spectrometer-based line-of-sight temperature measurements during alkali-pulverized coal combustion in a power station boiler. *Energies 10*(9), 1375. *(p. 26)*

Zabrodiec, D., J. Hees, A. Massmeyer, F. vom Lehn, M. Habermehl, O. Hatzfeld, and R. Kneer (2017). Experimental investigation of pulverized coal flames in co2/o2- and n2/o2-atmospheres: Comparison of solid particle radiative characteristics. *Fuel 201*, 136 – 147. 1st International Workshop on Oxy-Fuel Combustion. *(p. 12, 26)*

Zhang, D. (2013). *Ultra-supercritical coal power plants : materials, technologies and optimisation*. Woodhead Pub. *(p. 7)*

Zhang, L., E. Binner, Y. Qiao, and C.-Z. Li (2010). In situ diagnostics of victorian brown coal combustion in o2/n2 and o2/co2 mixtures in drop-tube furnace. *Fuel 89*(10), 2703 – 2712. *(p. 32)*

Zhao, X.-Y. and D. C. Haworth (2014). Transported PDF modeling of pulverized coal jet flames. *Combustion and Flame 161*(7), 1866 – 1882. *(p. 12, 70)*

Zhou, Z., L. Chen, L. Guo, B. Qian, Z. Wang, and K. Cen (2017). Computational modeling of oxy-coal combustion with intrinsic heterogeneous char reaction models. *Fuel Processing Technology 161*, 169 – 181. *(p. 76)*

Zolin, A., A. Jensen, L. S. Pedersen, K. Dam-Johansen, and P. TÃ¸rslev (1998). A comparison of coal char reactivity determined from thermogravimetric and laminar flow reactor experiments. *Energy & Fuels 12*(2), 268–276. *(p. 31)*

université PARIS-SACLAY | ÉCOLE DOCTORALE Sciences mécaniques et énergétiques, matériaux et géosciences (SMEMAG)

Titre: Etudes expérimentales et numériques de la pyrolyse et l'oxydation du charbon pulvérisé dans les flammes étirées de méthane/oxygène/azote

Mots-clés: PCC, matières volatiles, flamme laminaire étirée, OEC, FES

Résumé: Dans ce travail, une configuration laminaire stratifiée est utilisée afin d'étudier les caractéristiques de la pyrolyse et de l'oxydation du charbon pulvérisé dans un mélange de flux réactif à la fois dans les conditions atmosphériques conventionnelles et dans des conditions de combustion enrichie en oxygène. Deux diagnostics optiques, la spectroscopie d'émission de flamme et la mesure de l'émission spontanée sont utilisés pour caractériser la structure de la flamme. Les profiles de concentration de trois radicaux excités, OH^*, CH^* and C_2^* sont mesurés et analysés. Des simulations 1-D utilisant la cinétique détaillée y compris des sous-mécanismes de OH^*, CH^* and C_2^* et de combustion de charbon sont effectuées et comparées avec des données expérimentales. La comparaison qualitative a montré que la configuration numérique actuelle était appropriée pour la prédiction des émissions de OH^*, CH^* and C_2^*. Les résultats prédits par l'approche numérique diffèrent avec les modifications apportées aux sous-modèles de charbon et aux paramètres cinétiques. Le modèle de pyrolyse et les matières volatiles semblent jouer des rôles plus importants.

Title: Experimental and numerical studies of pulverized coal devolatilization and oxidation in strained methane/oxygen/nitrogen flames

Keywords: PCC, volatile matter, laminar strained flame, OEC, FES

Abstract: In the present work, a laboratory-scale laminar strained configuration is used to investigate the characteristics of pulverized coal devolatilization and oxidation in a mixture of $CH_4/O_2/N_2$ reactive flow both in conventional air conditions and in oxygen-enriched combustion conditions. Two optical diagnostics, Flame Emission Spectroscopy and measurement of spontaneous emission, are employed for the characterization of flame structure. The spatial concentration evolution of three excited radicals, OH^*, CH^* and C_2^*, are measured and analyzed. 1-D simulations using detailed gas-phase kinetics including OH^*, CH^*, and C_2^* sub-mechanisms and coal combustion submodels are performed and compared with experimental data. Qualitative comparison with experiments showed that the current numerical configuration was suitable for the prediction of OH^*, CH^* and C_2^* emission. The predicted results differed with changes to the coal sub-models and kinetic parameters. The devolatilization model and volatile matters seem to play more important roles.
